

NASA CR-2752

NASA CONTRACTOR
REPORT



NASA-GR-2

1241900

TECH LIBRARY KAFB, NM

LOAN COPY: RETURN TO
AFWL TECHNICAL LIBRARY
KIRTLAND AFB, N. M.



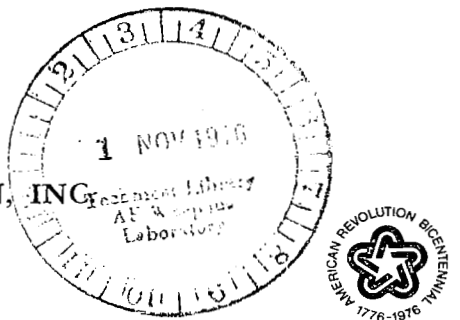
WIND SHEAR AND TURBULENCE AROUND AIRPORTS

W. S. Lewellen and Guy G. Williamson

Prepared by

AERONAUTICAL RESEARCH ASSOCIATES OF PRINCETON, INC.
Princeton, N.J. 08540

for George C. Marshall Space Flight Center



NATIONAL AERONAUTICS AND SPACE ADMINISTRATION • WASHINGTON, D. C. • OCTOBER 1976



0061421

1. REPORT NO. NASA CR-2752	2. GOVERNMENT ACCESSION NO.	3. RECIPIENT'S CATALOG NO.	
4. TITLE AND SUBTITLE Wind Shear and Turbulence Around Airports		5. REPORT DATE October 1976	
7. AUTHOR(S) W. S. Lewellen and Guy G. Williamson		6. PERFORMING ORGANIZATION CODE	
9. PERFORMING ORGANIZATION NAME AND ADDRESS Aeronautical Research Associates of Princeton, Inc. Princeton, New Jersey 08540		8. PERFORMING ORGANIZATION REPORT # M-185	
12. SPONSORING AGENCY NAME AND ADDRESS National Aeronautics and Space Administration Washington, D. C. 20546		10. WORK UNIT NO.	
		11. CONTRACT OR GRANT NO. NAS8-31380	
		13. TYPE OF REPORT & PERIOD COVERED Contractor Report	
15. SUPPLEMENTARY NOTES This report was prepared under the technical monitorship of the Aerospace Environment Division, Space Sciences Laboratory, NASA Marshall Space Flight Center.			
16. ABSTRACT A two-part study was conducted in the research program to determine the feasibility of predicting the conditions under which wind/turbulence environments hazardous to aviation operations exist. The first part of the study describes the Aeronautical Research Associates of Princeton computer model used to solve the velocity, temperature, and turbulence distributions in the atmospheric boundary layer, and gives the results of a parametric analysis to determine the expected range of wind shear and turbulence to be encountered in the vicinity of airports. The second part describes the delineation of an ensemble of aircraft accidents in which low-level wind shear and/or turbulence appeared to have been causative factors. This set of accidents, encompassing a wide range of meteorological conditions, should prove useful in developing techniques for reconstructing hazardous wind environments for aircraft safety investigation purposes.			
17. KEY WORDS Wind Shear Turbulence Atmospheric boundary layer Wind profile	18. DISTRIBUTION STATEMENT 02		
19. SECURITY CLASSIF. (of this report) Unclassified	20. SECURITY CLASSIF. (of this page) Unclassified	21. NO. OF PAGES 82	22. PRICE \$4.75

FOREWORD

The research in this document was intended to contribute to determining the feasibility of predicting the conditions under which wind/turbulence environments hazardous to aviation operations exist. Aeronautical Research Associates of Princeton has developed a computer model for solving for the velocity, temperature, and turbulence distributions in the atmospheric boundary layer. The model is based on using invariant modeling for closure of the dynamic equations of the ensemble-averaged, single-point, second-order correlations of the fluctuating velocities and temperature. The model equations are reviewed, and the dimensionless parameters investigated include surface roughness, geostrophic wind, latitude, surface heating, baroclinicity, radiation flux divergence, and geostrophic accelerations. Results of some variations in each of these variables and of some indication of probable maximum wind shear conditions at airports are presented. From the National Transportation Safety Board aircraft accident data bank, a set of accidents for which wind shear and/or turbulence appeared to be a contributing factor was investigated to select cases which can be used to evaluate the feasibility of predicting when conditions will be hazardous to aircraft operations. It is believed that results from this two-part study can have significant implications relative to the aeronautical safety aspects during landing and takeoff.

This research was conducted by the Aeronautical Research Associates of Princeton for the National Aeronautics and Space Administration, George C. Marshall Space Flight Center, Huntsville, Alabama, under the technical direction of Mr. Dennis W. Camp and Mrs. Margaret B. Alexander of the Space Sciences Laboratory. The support for this research was provided by Mr. John Enders of the Aeronautical Operating Division, Office of Advanced Research and Technology, NASA Headquarters.

TABLE OF CONTENTS

	Page
PART	
I	PARAMETERIC ANALYSIS OF TYPICAL PROFILES IN THE PLANETARY BOUNDARY LAYER..... 1
SECTION	
1	INTRODUCTION..... 1
2	NOMENCLATURE..... 3
3	REVIEW OF MODEL..... 5
4	GOVERNING DIMENSIONLESS PARAMETERS..... 9
5	RESULTS OF PARAMETER VARIATION..... 13
	Rossby Number Variation..... 13
	Geostrophic Acceleration..... 13
	Stability Variations..... 24
	Influence of Baroclinicity..... 42
	Radiation Flux Divergence..... 55
6	SUMMARY AND CONCLUSIONS..... 61
PART	
II	SELECTION OF AN ENSEMBLE OF AIRCRAFT ACCIDENTS FOR WHICH WIND SHEAR OR TURBULENCE APPEARED TO BE A CONTRIBUTING FACTOR..... 69
SECTION	
1	INTRODUCTION..... 69
2	SELECTING ACCIDENT CASES..... 71
3	REFERENCES..... 77

LIST OF TABLES

		Page
TABLE		
1	RANGE OF EXPECTED VALUES OF PLANETARY BOUNDARY LAYER PARAMETERS.....	11
2	NOTATION FOR ISOLINE PLOTS.....	67
3	KEY FOR SUMMARY PLOTS (FIGURES 34 AND 35).....	68
4	CAUSE/FACTORS, TYPE OF ACCIDENT, AND OPERATIONAL PHASES WHERE WIND SHEAR AND/OR TURBULENCE COULD HAVE CONTRIBUTED TO THE AIRCRAFT ACCIDENT.....	72
5	ACCIDENTS FOR FURTHER INVESTIGATION.....	74

LIST OF ILLUSTRATIONS

	Page
Figure	
1 Influence of Rossby Number on the Mean Wind Component in the Direction of the Geostrophic Wind (Normalized Altitude Converts to z in km for $f = 10^{-4} \text{ sec}^{-1}$ and $U_g = 10 \text{ m/sec}$) ($Ri = M = G_A = \mu_r = 0$).....	14
2 Influence of Rossby Number on the Mean Wind Component in the Direction Normal to the Geostrophic Wind for the Conditions of Figure 1.....	15
3 Influence of Rossby Number on the Variance of the Vertical Velocity for the Conditions of Figure 1.....	16
4 Influence of Rossby Number on the Variance of the Velocity in the Direction of the Geostrophic Wind for the Conditions of Figure 1.....	17
5 Influence of Rossby Number on the Variance of the Velocity in the Direction Normal to the Geostrophic Wind for the Conditions of Figure 1.....	18
6 Influence of Rossby Number on the Turbulent Macroscale (Solid Curve as Predicted by Eq. (14); Dashed Curve Simplified Approximation) for the Conditions of Figure 1...	19
7 Total Velocity Fluctuation as a Function of Rossby Number for Steady-State Flow and for a Periodically Varying Geostrophic Wind [$U_g = 10 \text{ m/sec} \cos(\pi t \text{ (hrs)}/12)$] ($-6.4 > G_A < 6.4$, $Ri = \mu_r = M = 0$).....	21
8 Isolines of the Component of the Mean Wind in the Direction of the Geostrophic Wind for a Full Period Variation of U_g on an Altitude vs Time Plot [$U_g = 10 \text{ m/sec} \cos(\pi t \text{ (hrs)}/12)$] ($-6.4 > G_A < 6.4$, $Ri = \mu_r = M = 0$).....	22
9 Isolines of the Component of the Mean Wind in the Direction Normal to the Geostrophic Wind for the Conditions of Figure 8.....	23
10 Influence of Richardson Number on the Quasi-Steady Distributions of Mean Wind Component in the Direction of the Geostrophic Wind ($Ro = 10^6$, $G_A = M = \mu_r = 0$).....	25

Figure

11	Influence of Richardson Number on the Quasi-Steady Distributions of Mean Wind Component in the Direction Normal to the Geostrophic Wind for the Conditions of Figure 10.....	26
12	Vertical Velocity Variance for Unstable Conditions Compared with the Limiting Profile for Free Convection ($G_A = M = \mu_r = 0$).....	27
13a	Isolines of the Component of the Mean Wind in the Direction of the Geostrophic Wind for a Standard Summer Day in Midwestern United States ($Ro = 10^7$, $M = G_A = 0$)....	29
13b	Vertical Distributions of u Taken at Select Times from Figure 13a.....	30
14a	Isolines of the Component of the Mean Wind in the Direction Normal to the Geostrophic Wind for the Conditions of Figure 13.....	31
14b	The Vertical Distributions of v Taken at Select Times From Figure 14a.....	32
15	Isolines of Turbulence Intensity q^2 for the Conditions of Figure 13.....	33
16	Isolines of Turbulence Macroscale Λ for the Conditions of Figure 13.....	34
17a	Isolines of u for a Reduced Symmetrical, Periodic, Heat Flux and An Increased Upper-Level Temperature Gradient ($Ro = 10^6$, $M = G_A = 0$).....	36
17b	Vertical Distributions of u taken at select times from Figure 17a.....	37
18a	Isolines of v for the Conditions of Figure 17.....	38
18b	Vertical Distributions of v Taken at Select Times from Figure 18a.....	39

Figure

19	Isolines of Turbulence Intensity q^2 for the Conditions of Figure 17.....	40
20	Isolines of Turbulence Macroscale Λ for the conditions of Figure 17.....	41
21	Isolines of u for a Thermal Wind Varying Periodically in Direction ($Ro = 10^6$, $\partial\theta/\partial Z _\infty = 3^\circ\text{C}/\text{km}$, $M = 1.25$, $\mu_r = 0$, $Ri(10) = 0$).....	43
22	Isolines of v for the Conditions of Figure 21.....	44
23	Isolines of Turbulence Intensity q^2 for the Conditions of Figure 21.....	45
24	Isolines of Turbulence Macroscale Λ for the Conditions of Figure 21.....	46
25	Isolines of u for the Same Thermal Wind Variation as in Figure 21 but with $\partial\theta/\partial Z _\infty = 9.87^\circ\text{C}/\text{km}$ ($Ro = 10^6$, $M = 12.5$, $\mu_r = 0$, $Ri(10) = 0$).....	48
26	Isolines of v for the Conditions of Figure 25.....	49
27	Isolines of Turbulence Intensity q^2 for the Conditions of Figure 25.....	50
28	Isolines of Turbulence Macroscale Λ for the conditions of Figure 25.....	51
29a	Influence of Temperature Advection on the Profiles of Figures 25 and 26 at a Set Time, 24 Hours, After Initialization of the run (Run 16 without Advection and Run 17 with Advection); (a) Mean Wind Components..	53
29b	Influence of Temperature Advection on the Profiles of Figures 25 and 26 at a Set Time, 24 Hours, After Initialization of the Run (Run 16 Without Advection and Run 17 with Advection); (b) Potential Temperature Distribution.....	54

	Page
Figure	
30 Isolines of u for a Simulated Day with the Radiation Flux Divergence of Eq. (23) over a Constant Temperature Surface ($Ro = 10^6$, $\partial\theta/\partial Z = 3^\circ\text{C}/\text{km}$, $M = 0$).....	56
31 Isolines of v for the Conditions of Figure 30.....	57
32 Isolines of Turbulence Intensity q^2 for the Conditions of Figure 30.....	58
33 Isolines of Turbulence Macroscale Λ for the Conditions of Figure 30.....	59
34 Summary Plot of Normalized Total Velocity Fluctuation as a Function of the Bulk Richardson Number Between the Surface and 1 km Altitude.....	62
35 Summary Plot of Maximum Wind Shear at or Above 10 m Altitude as a Function of the Bulk Richardson Number Between the Surface and 1 km Altitude.....	63
36 Summary Plot of Wind Shear as a Function of Altitude Showing the Influence of the Expected Range of Variations in Ro , Ri and M	65

WIND SHEAR AND TURBULENCE AROUND AIRPORTS

W. S. Lewellen and Guy G. Williamson

SUMMARY

In June of 1975, we initiated a research program with the ultimate goal of determining the feasibility of predicting the conditions under which wind/turbulence environments hazardous to aviation operations exist. This report on the first six months of this effort is divided into two parts. The first part describes the computer model used for solving for the velocity, temperature, and turbulence distributions in the atmospheric boundary layer and gives the results of a parametric analysis to determine the expected range of wind shear and turbulence to be encountered in the vicinity of airports. The second part describes the delineation of an ensemble of aircraft accidents in which low-level wind shear and/or turbulence appeared to have been causative factors. This set of accidents, encompassing a wide range of meteorological conditions, should prove useful in developing techniques for reconstructing hazardous wind environments for aircraft safety investigation purposes.

Also during this six months, an investigation of the wind shear and turbulence conditions existing at Kennedy International Airport on the afternoon of 24 June 1975 was made. Results of this study are detailed in a separate report. It showed that a wind shear of the order of 15 m/sec over a 100 m altitude change was quite consistent with the meteorological conditions at the time of the Eastern Airlines Flight 66 crash.

PART 1. PARAMETRIC ANALYSIS OF TYPICAL PROFILES IN THE PLANETARY BOUNDARY LAYER

INTRODUCTION

Over the last few years, Aeronautical Research Associates of Princeton, Inc. (A.R.A.P.) has developed a computer model for solving for the velocity, temperature, and turbulence distributions in the atmospheric boundary layer (refs. 1 - 5). The model is based on using invariant modeling for closure of the dynamic equations of the ensemble-averaged, single point, second-order correlations of the fluctuating velocities and temperature.

Details of our atmospheric boundary layer model, as developed under EPA sponsorship for the purpose of predicting the dispersal of atmospheric pollutants, are given in reference 5. The basic assumption is that the dependence of the third-order correlations of the velocity fluctuations on the second-order correlations, the mean flow properties, and their derivatives is invariant with respect to changes in flow geometry. This permits data from relatively simple flow experiments to be used in evaluating the necessary coefficients in the modeled terms.

Verification comparisons between model predictions and a variety of experimental observations are presented in references 5 - 8. The prediction of wind shear and vertical velocity fluctuations has been tested against observations in the surface layer, and agreement is very good (ref. 7). Also, predictions of the vertical velocity fluctuations in the afternoon unstable mixed layer agree very well (ref. 8) with laboratory simulations of this layer. These verifications have convinced us that the model is fundamentally correct. However, specific verification of wind shear and turbulence prediction capabilities in the vicinity of airports should be tested by comparison with experimental observations at a number of airports in order to permit us to set more precise confidence levels. This process might lead to some adjustments in the model, but we believe the present estimates represent the best currently available.

Herein we will first review the model equations and then formulate the governing dimensionless parameters to be studied. The dimensional variables to be investigated are surface roughness, geostrophic wind, latitude, surface heating, baroclinicity, radiation flux divergence, and geostrophic accelerations. Results of some variation in each of these variables will be presented. Although in the confines of this brief study it has not been possible to look at all possible combinations of these variables, it is possible to give some indication of probable maximum wind shear conditions at airports.

As a part of this parameter study, we have investigated conditions approximating those existing at Kennedy International Airport on the afternoon of 24 June 1975 when Eastern Airlines Flight 66 crashed. The results of that investigation have been detailed in a separate report (ref. 9).

NOMENCLATURE

f	Coriolis parameter = $2\Omega \sin \phi$
G_A	parameter measuring geostrophic acceleration, eq. (19)
g	gravitational acceleration
k	von Kármán's constant = $-u_*/(z \partial u/\partial z)_0$ in the neutral surface layer
L	Monin-Obukhov length = $-\theta_0 u_*^3 / kg(\bar{w}\theta)_0$
M	parameter measuring the magnitude of baroclinicity, eq. (18)
P	mean pressure
q	square root of twice the turbulent kinetic energy
\dot{Q}	temperature source strength denoting radiation flux divergence or temperature advection
Ri	Richardson number
$Ri()$	bulk Richardson number based on the temperature and velocity difference between the altitude indicated in () and the surface
Ro	Rossby number based on geostrophic wind conditions = U_g/fz_0
t	time
U	mean velocity in the direction of the geostrophic wind at the top of the boundary layer
U_g	U component of the geostrophic wind velocity
u	fluctuating velocity in the direction of the geostrophic wind at the top of the boundary layer
u_*	surface shear stress velocity
V	mean velocity perpendicular to the geostrophic wind direction at the top of the boundary layer
V_g	V component of the geostrophic wind
v	fluctuating velocity perpendicular to the geostrophic wind direction at the top of the boundary layer
W	mean vertical velocity
w	fluctuating vertical velocity
w_*	free convective velocity scale = $[gz_i(\bar{w}\theta)_0/\theta_0]^{1/3}$
z	vertical coordinate
z_i	temperature inversion height above an unstable layer
z_0	surface roughness height

β_0	parameter defining the direction of the geostrophic wind shear, eq. (18)
ϵ	dissipation function
θ	mean potential temperature perturbation
θ	fluctuating potential temperature
θ_0	absolute temperature about which the perturbation is taken
Λ	model macroscale length
μ, μ_0, μ_r	stability parameters defined in eqs. (16) and (17)
ϕ	latitude
Ω_i	angular velocity of the coordinate system

Superscript:

— denotes ensemble average

REVIEW OF MODEL

For homogeneous boundary conditions at the surface and at the top of the boundary layer, the equations of motion for the mean horizontal velocity and perturbation potential temperature within the boundary layer may be written for high Reynolds number as

$$\frac{\partial U}{\partial t} = f(V - V_g) - \frac{\partial}{\partial z} \bar{uw} \quad (1)$$

$$\frac{\partial V}{\partial t} = -f(U - U_g) - \frac{\partial}{\partial z} \bar{vw} \quad (2)$$

$$\frac{\partial \theta}{\partial t} = - \frac{\partial}{\partial z} \bar{w\theta} + \dot{Q} \quad (3)$$

Even with the energy source term \dot{Q} prescribed, the solution to this set of equations is not determined until some functional dependences of turbulent transport terms \bar{uw} , \bar{vw} , and $\bar{w\theta}$ are determined. Classical methods of modeling the planetary boundary layer (ref. 10) involve the assumption of some type of eddy viscosity to determine turbulent transport. Our approach is to use the Reynolds stress equations to directly compute the ensemble-averaged turbulent transport terms with invariant modeling techniques applied to close the system of equations. These equations with their modeled terms may be written as follows (ref. 5):

the six equations for the independent Reynolds stresses

$$\begin{aligned} \frac{\partial \bar{uu}}{\partial t} = & 4\Omega(\bar{uv} \sin \phi - \bar{uw} \cos \phi) - 2\bar{uw} \frac{\partial U}{\partial z} + 0.3 \frac{\partial}{\partial z} \left[\Lambda q \frac{\partial \bar{uu}}{\partial z} \right] \\ & - \frac{q}{\Lambda} \left(\bar{uu} - \frac{q^2}{3} \right) - \frac{q^3}{12\Lambda} \end{aligned} \quad (4)$$

$$\begin{aligned} \frac{\partial \bar{vv}}{\partial t} = & -4\Omega\bar{uv} \sin \phi - 2\bar{vw} \frac{\partial V}{\partial z} + 0.3 \frac{\partial}{\partial z} \left[\Lambda q \frac{\partial \bar{vv}}{\partial z} \right] \\ & - \frac{q}{\Lambda} \left(\bar{vv} - \frac{q^2}{3} \right) - \frac{q^3}{12\Lambda} \end{aligned} \quad (5)$$

$$\frac{\partial \overline{w w}}{\partial t} = 4\Omega \overline{u w} \cos \phi + \frac{2g}{\theta_o} \overline{w \theta} + 0.3 \frac{\partial}{\partial z} \left[\Lambda q \frac{\partial \overline{w w}}{\partial z} \right] - \frac{q}{\Lambda} \left(\overline{w w} - \frac{q^2}{3} \right) - \frac{q^3}{12\Lambda} \quad (6)$$

$$\frac{\partial \overline{u v}}{\partial t} = 2\Omega(\overline{v v} \sin \phi - \overline{v w} \cos \phi - \overline{u u} \sin \phi) - \overline{u w} \frac{\partial V}{\partial z} - \overline{v w} \frac{\partial U}{\partial z} + 0.3 \frac{\partial}{\partial z} \left[\Lambda q \frac{\partial \overline{u v}}{\partial z} \right] - \frac{q}{\Lambda} \overline{u v} \quad (7)$$

$$\frac{\partial \overline{u w}}{\partial t} = 2\Omega(\overline{v w} \sin \phi - \overline{w w} \cos \phi + \overline{u u} \cos \phi) - \overline{w w} \frac{\partial U}{\partial z} + \frac{g}{\theta_o} \overline{u \theta} + 0.3 \frac{\partial}{\partial z} \left[\Lambda q \frac{\partial \overline{u w}}{\partial z} \right] - \frac{q}{\Lambda} \overline{u w} \quad (8)$$

$$\frac{\partial \overline{v w}}{\partial t} = 2\Omega(-\overline{u w} \sin \phi + \overline{u v} \cos \phi) - \overline{w w} \frac{\partial V}{\partial z} + \frac{g}{\theta_o} \overline{v \theta} + 0.3 \frac{\partial}{\partial z} \left[\Lambda q \frac{\partial \overline{v w}}{\partial z} \right] - \frac{q}{\Lambda} \overline{v w} \quad (9)$$

the three equations for the components of the heat flux vector

$$\frac{\partial \overline{u \theta}}{\partial t} = 2\Omega(\overline{v \theta} \sin \phi - \overline{w \theta} \cos \phi) - \overline{u w} \frac{\partial \theta}{\partial z} - \overline{w \theta} \frac{\partial U}{\partial z} + 0.3 \frac{\partial}{\partial z} \left[\Lambda q \frac{\partial \overline{u \theta}}{\partial z} \right] - \frac{0.75q}{\Lambda} \overline{u \theta} \quad (10)$$

$$\frac{\partial \bar{v}\theta}{\partial t} = -2\bar{u}\bar{\theta} \sin \phi - \bar{vw} \frac{\partial \theta}{\partial z} - \bar{w\theta} \frac{\partial v}{\partial z} + 0.3 \frac{\partial}{\partial z} \left[\Lambda q \frac{\partial \bar{v}\theta}{\partial z} \right] - \frac{0.75q}{\Lambda} \bar{v}\theta \quad (11)$$

$$\frac{\partial \bar{w}\theta}{\partial t} = 2\bar{u}\bar{\theta} \cos \phi - \bar{ww} \frac{\partial \theta}{\partial z} + \frac{g}{\theta_0} \bar{\theta}^2 + 0.3 \frac{\partial}{\partial z} \left[\Lambda q \frac{\partial \bar{w}\theta}{\partial z} \right] - \frac{0.75q}{\Lambda} \bar{w}\theta \quad (12)$$

the equation for the temperature variance

$$\frac{\partial \bar{\theta}^2}{\partial t} = -2\bar{w}\bar{\theta} \frac{\partial \theta}{\partial z} + 0.3 \frac{\partial}{\partial z} \left[\Lambda q \frac{\partial \bar{\theta}^2}{\partial z_j} \right] - \frac{0.45q}{\Lambda} \bar{\theta}^2 \quad (13)$$

and the equation for the turbulent macroscale

$$\frac{\partial \Lambda}{\partial t} = 0.35 \frac{\Lambda}{q^2} \left(\bar{uw} \frac{\partial U}{\partial z} + \bar{vw} \frac{\partial V}{\partial z} \right) + 0.075q + 0.3 \frac{\partial}{\partial z} \left(q\Lambda \frac{\partial \Lambda}{\partial z} \right) - \frac{0.375}{q} \left(\frac{\partial q\Lambda}{\partial z} \right)^2 + \frac{0.8\Lambda}{q^2} \frac{g\bar{w}\theta}{\theta_0} \quad (14)$$

These fourteen equations are solved simultaneously for the turbulence field. The detailed accounting of the modeled terms and the choice for the coefficients are given in references 3 and 5. Similar modeled equations are being used by Wyngaard et al. (refs. 11-13) and Mellor and Yamada (refs. 14-15) to compute atmospheric boundary layer flow. The primary differences in these models are that the model given in eqs. (4) through (14) has been developed from comparison with laboratory data to predict a wider class of flows, rather than being specialized to apply only to the atmospheric boundary layer flow. There are two reasons for this.

First, laboratory flows can, in general, be more carefully specified and measured. Second, the wider the class of flows for which the model is tested, the more likely the model is to be valid for an untested flow situation.

The general boundary conditions applied to these equations at the top of the boundary layer are that as $z \rightarrow \infty$

$$\left. \begin{array}{l} U = U_g \\ V = 0 \end{array} \right\} \quad \text{geostrophic wind}$$

$$\frac{\partial \theta}{\partial z} = \text{constant} \quad (\text{difference between the adiabatic lapse rate and the ambient lapse rate})$$

$$\overline{u_i u_j} = \overline{u_i \theta} = \overline{\theta \theta} = \Lambda = 0$$

Rather than compute all the way to the surface with these equations, which would, in general, require computing the flow around various roughness elements, the surface boundary conditions are applied at z_0 , the effective aerodynamic roughness height. At $z = z_0$,

$$U = V = 0$$

$$\theta = \theta_{\text{surface}} \quad (\text{or } \overline{w\theta} = \overline{w\theta}_{\text{surface}})$$

and the surface layer, Monin-Obukhov functions hold for the turbulent correlations.

Within the confines of this report, the model will be restricted to a one-dimensional, unsteady model with the above boundary conditions a function only of time. This sets the major limitation on the application of the model. As long as the surface conditions are reasonably homogeneous, the model may be applied to any location just by changing the boundary conditions. However, strong spatial inhomogeneities in surface roughness or heat flux will invalidate this one-dimensional model. An extended two-dimensional version of this model is now being used to make calculations along a shoreline for the Navy.

GOVERNING DIMENSIONLESS PARAMETERS

The flow is now completely specified when initial conditions on all the variables are specified. The dimensionless parameters governing the flow may be obtained by normalizing the equations and boundary conditions. For a characteristic velocity, let us choose U_g . Then, if we normalize all lengths by z_o and time by f^{-1} , eqs. (1) and (2) introduce one parameter, a Rossby number, $Ro = U_g/z_o f$. When the flow is neutral (i.e., $\theta = \text{constant}$ everywhere), then the only other parameter introduced by the remaining equations, eqs. (4) - (9) and (14), is $\cot \phi$. We will explore the variation resulting from changes in the Rossby number but will not explore the variation caused by changing $\cot \phi$ alone. Shir (ref. 16) has reported that varying $\cot \phi$ has a weak influence on the correlation distributions. We believe this to be the case but have not made a specific study of the sensitivity to this parameter.

When the potential temperature is allowed to vary but Q_r remains zero, one or more stability parameters must be introduced. If the temperature is normalized by $\Delta\theta$, not yet specified, then the equations introduce only one more parameter, a bulk Richardson number,

$$Ri_b = g\Delta\theta z_b / \theta_o U_o^2 g \quad (15)$$

For stable conditions, $\Delta\theta$ may be taken as the temperature difference across the boundary layer, while for unstable conditions, it would appear reasonable to take it as the height of the inversion layer times $(\partial\theta/\partial z)_\infty$. We will choose a bulk Richardson number based on the temperature and velocity differences between the surface and 10 meters. This appears adequate to characterize a quasi-steady turbulence field under stable conditions. However, unstable conditions appear to require two stability parameters even under quasi-steady conditions. To the bulk Richardson number, we add the ratio of the inversion height, z_i , to U_g/f . For this purpose, z_i is defined as the altitude near the top of the boundary layer where the temperature variance reaches a local maximum.

This combination of stability parameters is not unique. Zilitinkevich (ref. 17) uses two parameters

$$\mu_o = -\frac{g(\overline{w\theta})_o k^2}{u_*^2 f \theta_o} \quad (16a)$$

and

$$\mu = - \frac{z_i g(\bar{w}\theta)_o k}{u_*^3 \theta_o} \quad (16b)$$

Further, he argues that in relatively strongly **unstable** boundary layers, the flow becomes a function of μ only. Some of our results will be presented in terms of these variables.

When \dot{Q} is permitted to represent some radiation flux divergence \dot{Q}_r , then another governing parameter exists. One possible grouping for this parameter is to replace $\bar{w}\theta$ in μ_o with $\dot{Q}_r z_i$ to give

$$\mu_r = - \frac{g \dot{Q}_r z_i k^2}{u_*^2 f \theta_o} \quad (17)$$

This should be a rough measure of the stability influences on the turbulence resulting from radiation flux divergence.

The remaining parameters involve changes in the boundary conditions. To investigate geostrophic wind shear, otherwise known as thermal wind, or baroclinicity, a variation in U_g and V_g as a function of z is imposed as a boundary condition on the flow. This requires two parameters to specify the magnitude and direction of the geostrophic wind shear. Following Arya and Wyngaard (ref. 18), these will be taken as

$$M = \left[\left(\frac{\partial U_g}{\partial z} \right)^2 + \left(\frac{\partial V_g}{\partial z} \right)^2 \right]^{1/2} \frac{z_i}{(U_g)_{@z=z_i}} \quad (18)$$

$$\beta_0 = \tan^{-1} \frac{\partial V_g / \partial z}{\partial U_g / \partial z}$$

However, we have replaced u_* by U_g in forming M .

The one remaining parameter to be investigated in this report is acceleration in the geostrophic wind. The most natural parameter with which to compare is the Coriolis frequency f , i.e.,

$$G_A = \dot{U}_g / |U_{max}| f \quad (19)$$

The approximate range of values for the 8 parameters which may be expected in the vicinity of airports is given in Table I. Sample results of the model predictions for variations in these parameters are given in the next section.

Table I.

Range of Expected Values of Planetary Boundary Layer Parameters

Ro	10^4	-	10^8
$\text{Ri}_{(10)}$	-0.1	-	+0.1
μ_o	-500	-	+100
μ	-500	-	+100
μ_r	-100	-	+100
M	0	-	10
β	0	-	2π
G_A	- 10	-	+ 10

RESULTS OF PARAMETER VARIATION

Rossby Number Variation

Perhaps the simplest variation to unravel is that due to Rossby number under neutral, barotropic, steady-state conditions. The Rossby number variation may be due to changes in surface roughness, geostrophic wind, and/or latitude. Figures 1 and 2 show the mean wind profiles normalized by the geostrophic wind as a function zf/U_g for three different values of Ro . The wind component parallel to the geostrophic wind has a small overshoot which is slightly amplified as Ro increases. The dimensionless height at which it occurs is also reduced. The crosswind perpendicular to the geostrophic wind also increases and occurs at a lower altitude as Ro increases.

The vertical coordinate for these plots is normalized in such a way that for the typical values of $f = 10^{-4} \text{ sec}^{-1}$ and $U_g = 10 \text{ m/sec}$, z may be read directly in meters. For other values of U_g/f , the plot must be read as a dimensionless plot and the appropriate physical z determined. This shows that for equal Ro the neutral boundary layer would become thicker as the equator is approached and/or the geostrophic wind is increased.

The variances of the three velocity components are shown in figures 3, 4, and 5 for the same values of Ro . The amplitudes of these dimensionless variances decrease as Ro increases. However, if the Ro is increased by increasing U_g with z_0 and f held fixed, then the dimensional value of the variance will actually increase.

The macroscale Λ is shown in figure 6. The solid curves give Λ as predicted by eq. (14), while the dashed curve gives the simplified approximation obtained by holding the slope $\partial\Lambda/\partial z$ fixed until a maximum value equal to 15% of the spread of the turbulence is reached. All of the dynamic runs in this report with boundary conditions or parameters varying with time have been made using eq. (14). However, the quasi-steady runs shown in figures 1 through 5 and eqs. (10) and (11) were made with the simpler approximation. We do not believe the differences materially affect the sensitivity to the parameters shown here. For the specific example of the typical diurnal variations, both formulations have been run. The results using eq. (14) are given here and those using the simple approximation given in ref. 6.

Geostrophic Acceleration

The next parameter to be investigated is G_A to get an idea of how important it is to follow the unsteady development of the boundary layer rather than confine attention to steady calculations.

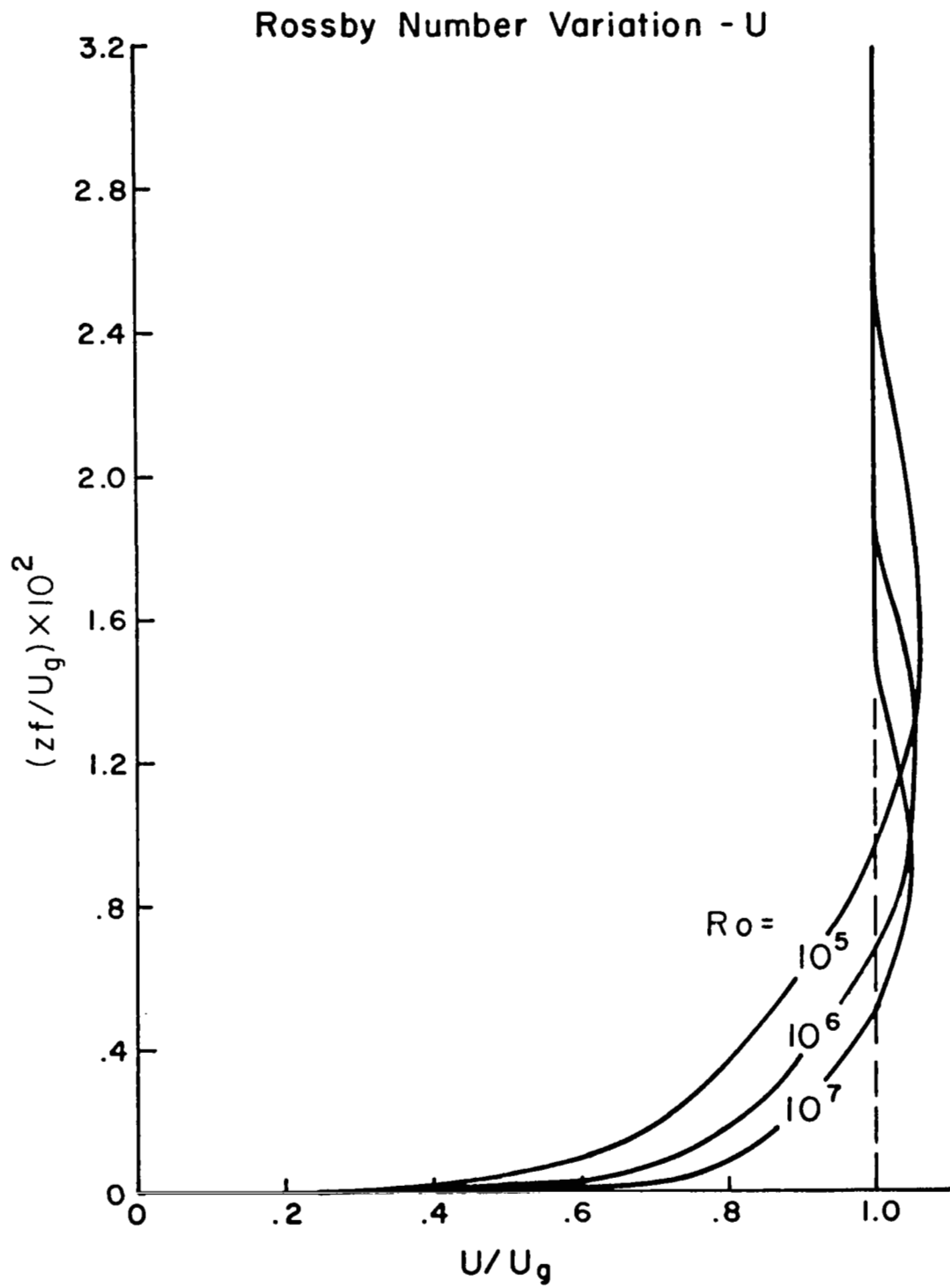


Figure 1. Influence of Rossby number on the mean wind component in the direction of the geostrophic wind (normalized altitude converts to z in km for $f = 10^{-4} \text{ sec}^{-1}$ and $U_g = 10 \text{ m/sec}$) ($Ri = M = G_A = \mu_r = 0$).

Rossby Number Variation - V

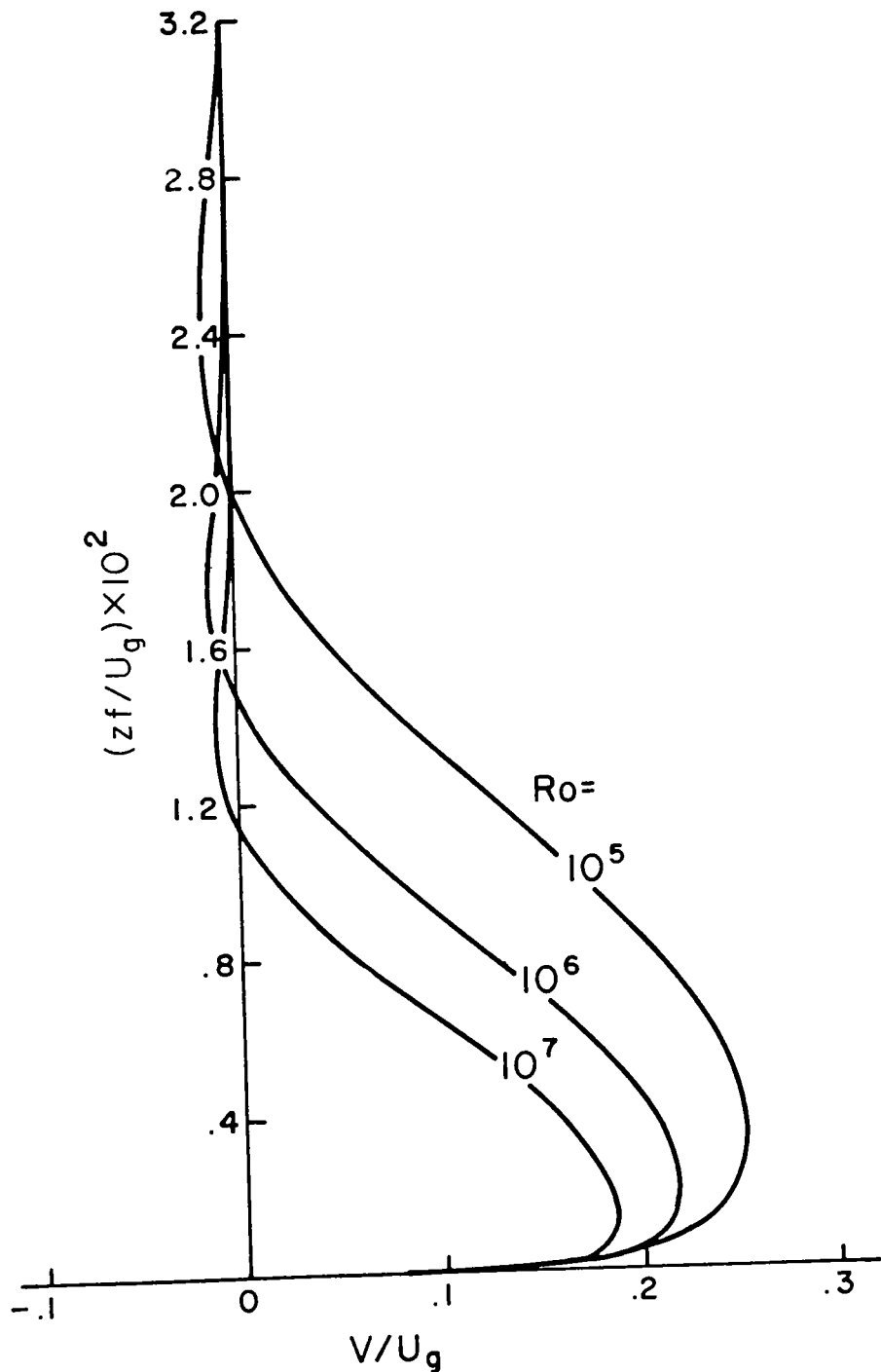


Figure 2. Influence of Rossby number on the mean wind component in the direction normal to the geostrophic wind for the conditions of figure 1.

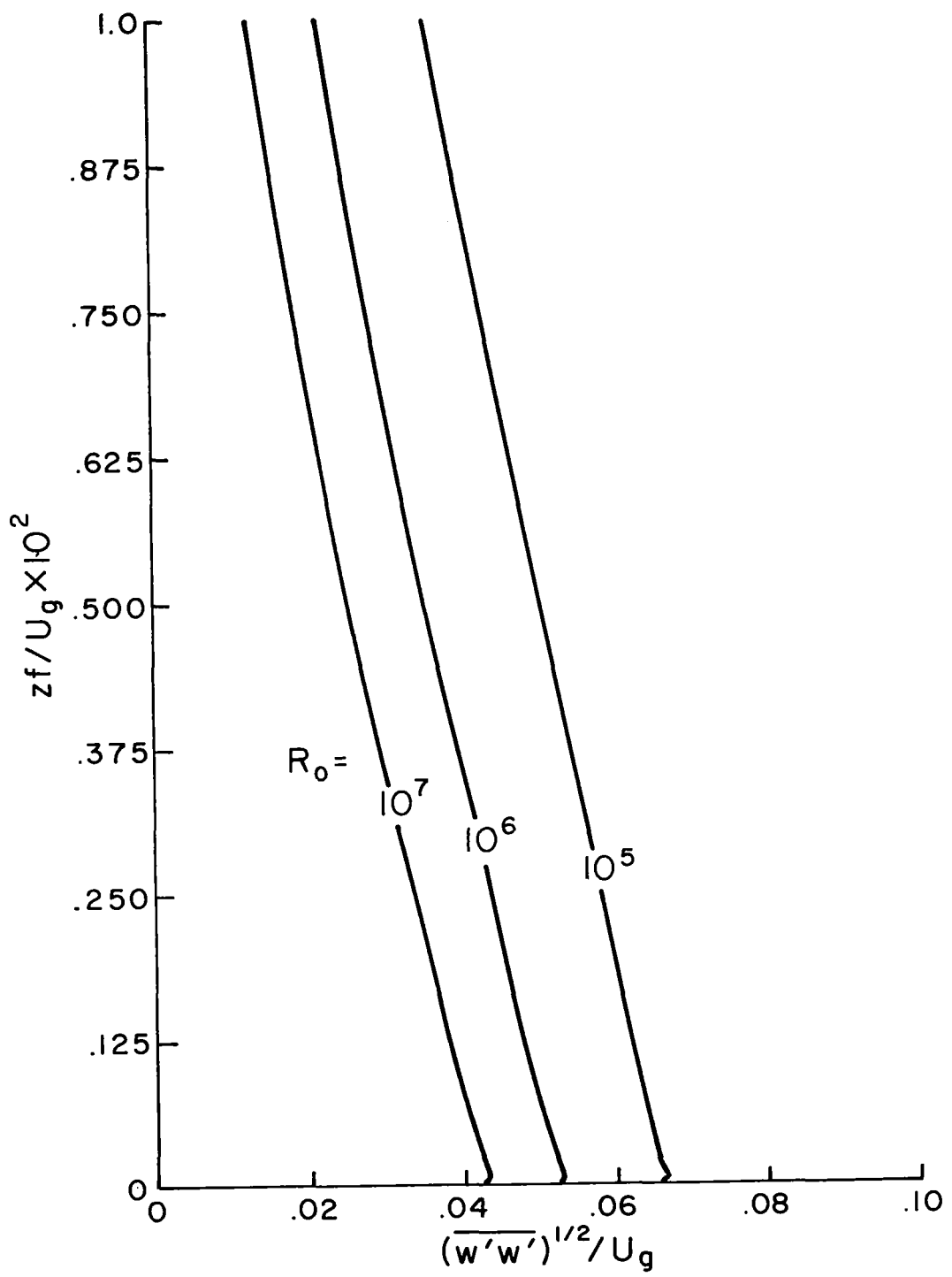


Figure 3. Influence of Rossby number on the variance of the vertical velocity for the conditions of figure 1.

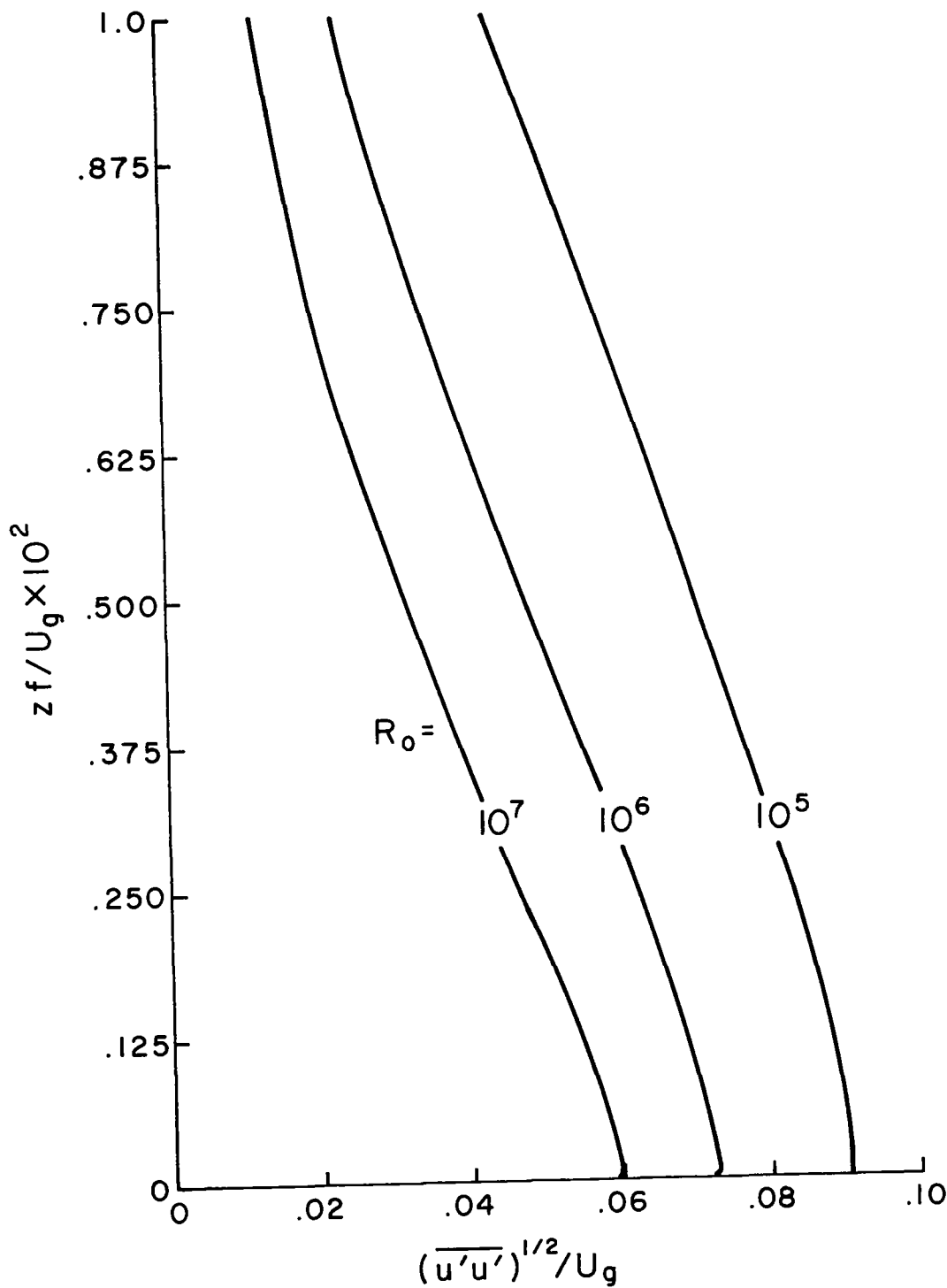


Figure 4. Influence of Rossby number on the variance of the velocity in the direction of the geostrophic wind for the conditions of figure 1.

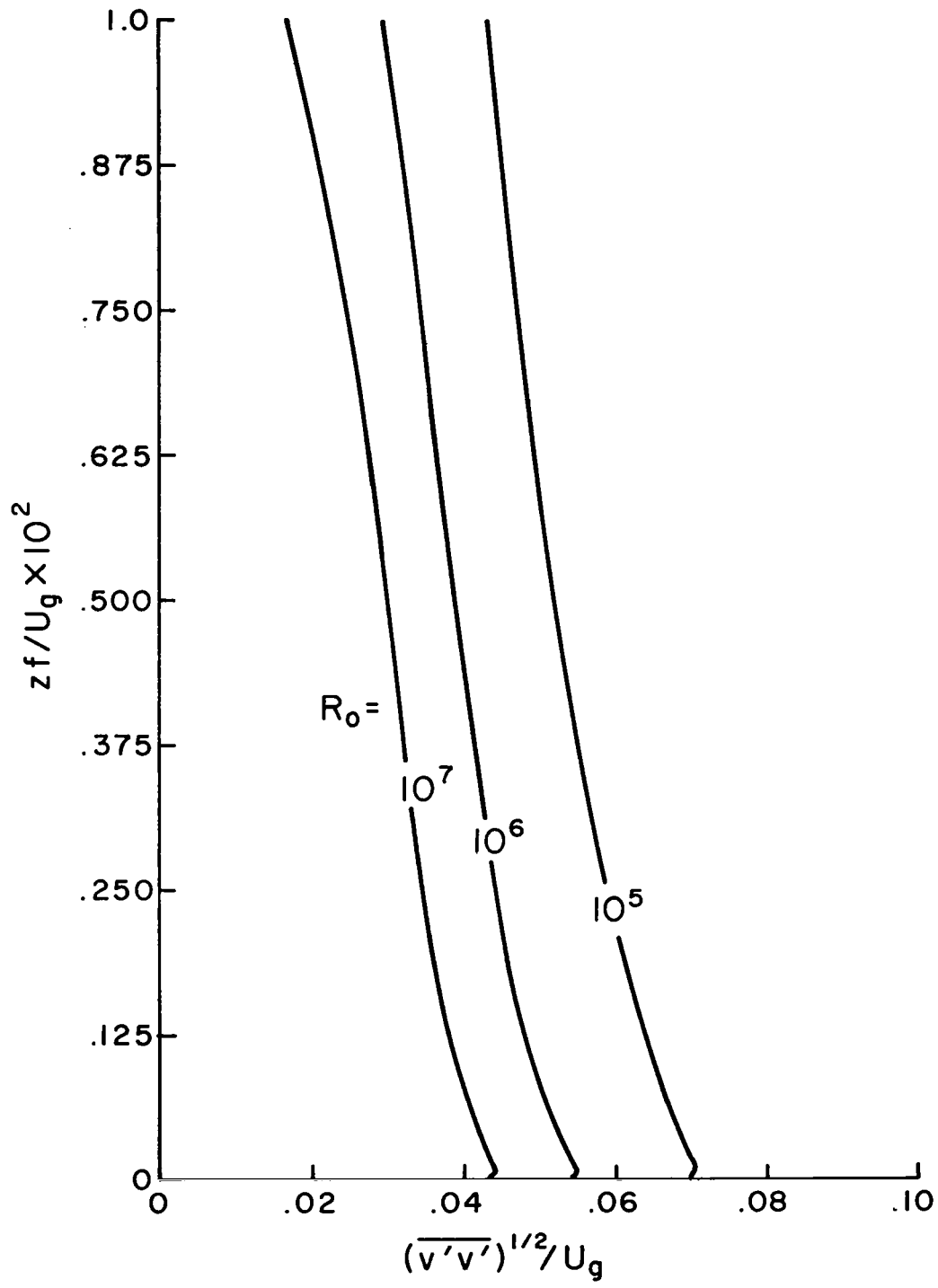


Figure 5. Influence of Rossby number on the variance of the velocity in the direction normal to the geostrophic wind for the conditions of figure 1.

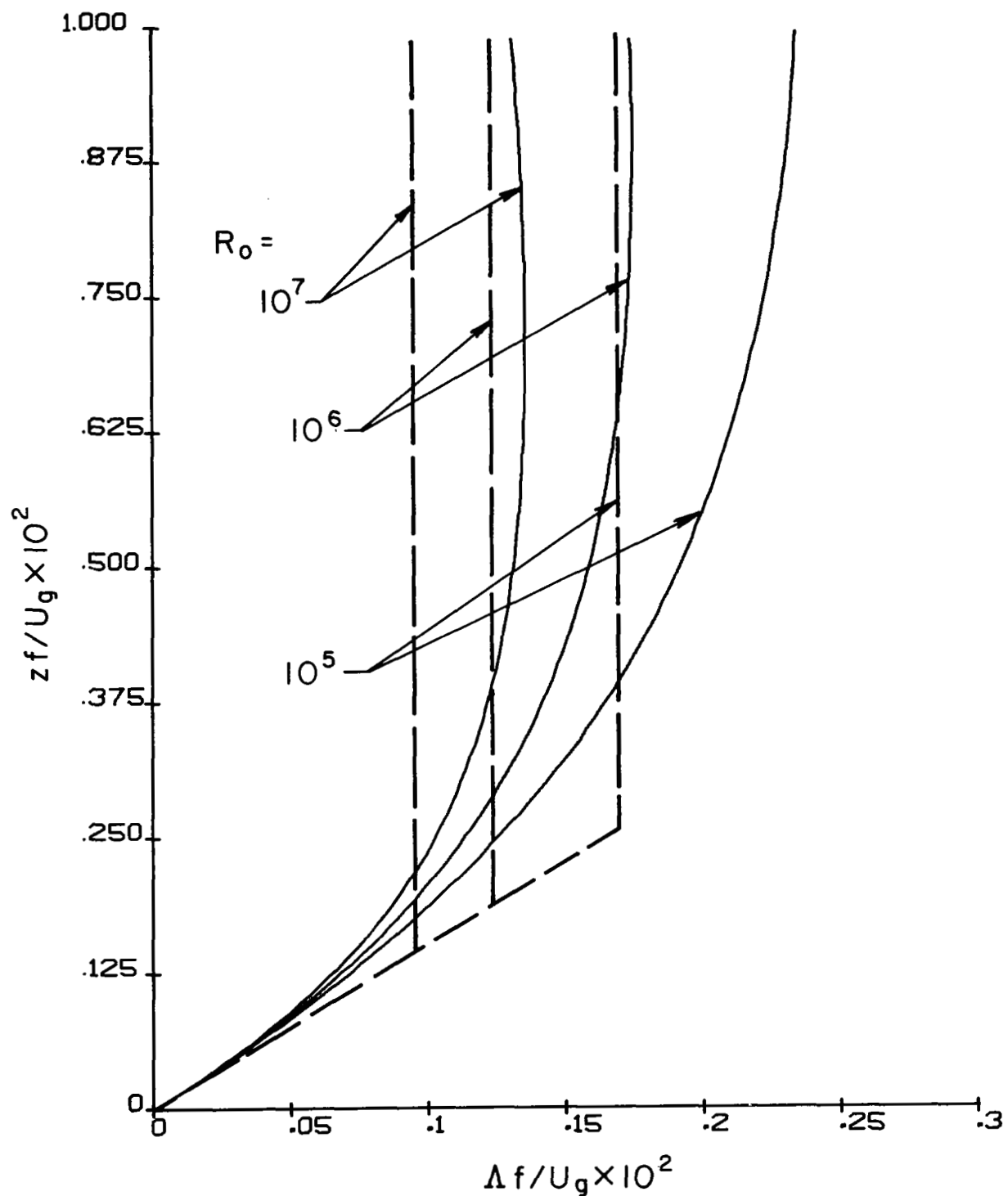


Figure 6. Influence of Rossby number on the turbulent macroscale (solid curve as predicted by Eq. (14); dashed curve simplified approximation) for the conditions of figure 1.

To do this, we have made a run where the geostrophic wind is allowed to vary sinusoidally from +10 m/sec to -10 m/sec over a period of 24 hours. This yields a maximum value of $G_A \approx 6.4$ and an average value of zero over the 24-hour period. As shown in figure 7, there is a significant difference between the steady-state values of turbulence intensity and those for the dynamic case.

The characteristic adjustment time in the turbulent correlation equations, eqs. (4) - (14), is proportional to Λ/q . Near the surface where Λ is proportional to z , this characteristic time is small - less than a minute for typical conditions at 10 m height. Therefore, in the surface layer, one can expect the turbulent correlations to be in equilibrium with the instantaneous values of the mean flow gradients. However, in eqs. (1) and (2), the characteristic time is f^{-1} which for 45° latitude is of the order of 3 hours. Therefore, variations in the geostrophic wind on a time scale of a few hours lead to unsteady effects in the velocity gradients through eqs. (1) and (2). This in turn leads to variations in the turbulent correlations, as demonstrated in figure 7.

Near the top of the boundary layer, Λ/q also approaches f^{-1} . Thus, although a local equilibrium approximation for the turbulence is quite appropriate near the surface, it is not appropriate in the upper levels of the boundary layer when the geostrophic wind is changing on a time scale of a few hours.

Isolines of constant wind speed in the direction of the geostrophic wind are shown in figure 8. The isolines are nearly symmetrical about the 12-hour point where $U_g = -10$ m/sec. At 10 m altitude, the component of wind shear in this direction is 0.10 sec^{-1} , very close to the steady-state value for the same boundary conditions. From figure 1 it may be seen that the wind shear may be properly normalized by dividing by f . The dimensional values quoted in this report are all given for $f = 10^{-4} \text{ sec}^{-1}$.

The transverse wind isolines are shown in figure 9. The maximum negative value is shifted to approximately 2 hours after the maximum negative value of the geostrophic wind. In spite of this, the plot tends to confirm the indication of figure 8 that the differences in the low-level wind shear between the dynamic and steady-state cases are not very significant. The maximum value of the vector velocity shear at 10 meters is 0.104 sec^{-1} for the dynamic case in comparison to 0.103 sec^{-1} for the steady-state case. Quite a reduction in the period of the geostrophic variation is required for this difference to be significant. For the rather extreme case of a 12-hour period for a complete cycle, the corresponding value of the maximum velocity shear remains remarkably close, although the height of the boundary layer as marked by the height where q^2 falls to 10% of its maximum value is reduced from

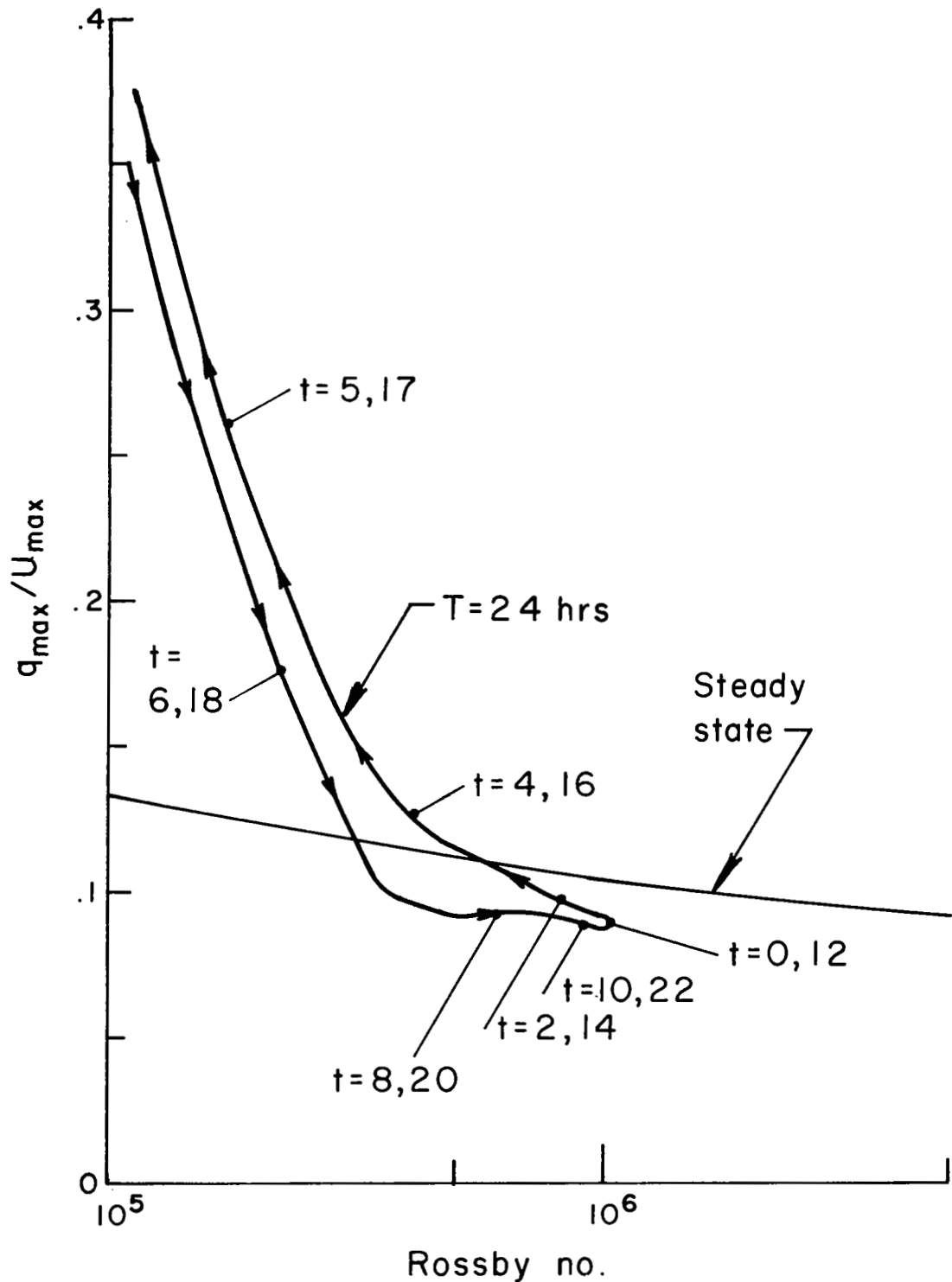


Figure 7. Total velocity fluctuation as a function of Rossby number for steady-state flow and for a periodically varying geostrophic wind [$U_g = 10 \text{ m/sec} \cos(\pi t(\text{hrs})/12)$] ($-6.4 > G_A < 6.4$, $Ri = \mu_r = M = 0$).

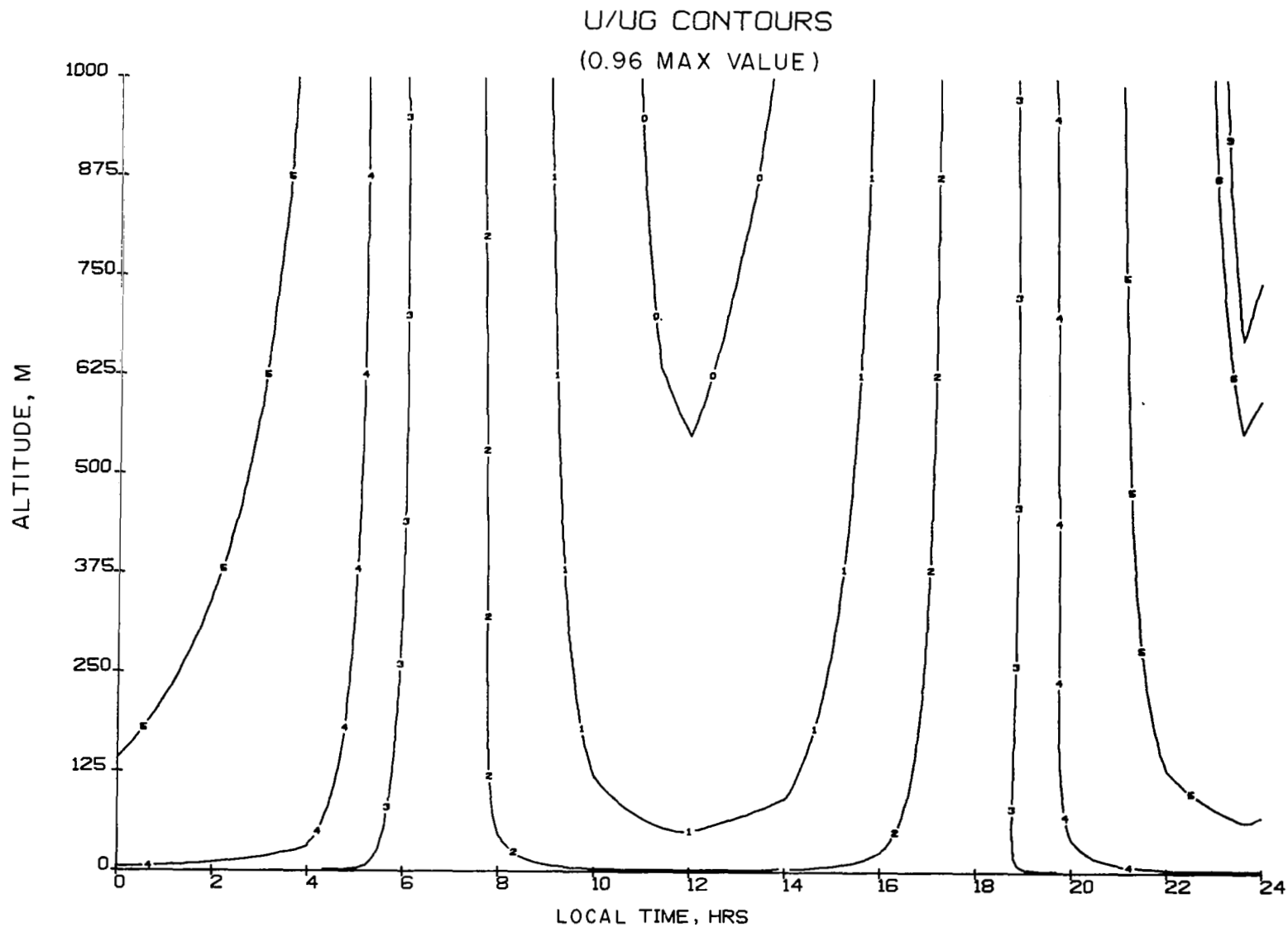


Figure 8. Isolines of the component of the mean wind in the direction of the geostrophic wind for a full period variation of U_g on an altitude vs. time plot [$U_g = 10 \text{ m/sec} \cos(\pi t(\text{hrs})/12)$] ($-6.4 > G_A < 6.4$, $Ri = \mu_r = M = 0$).

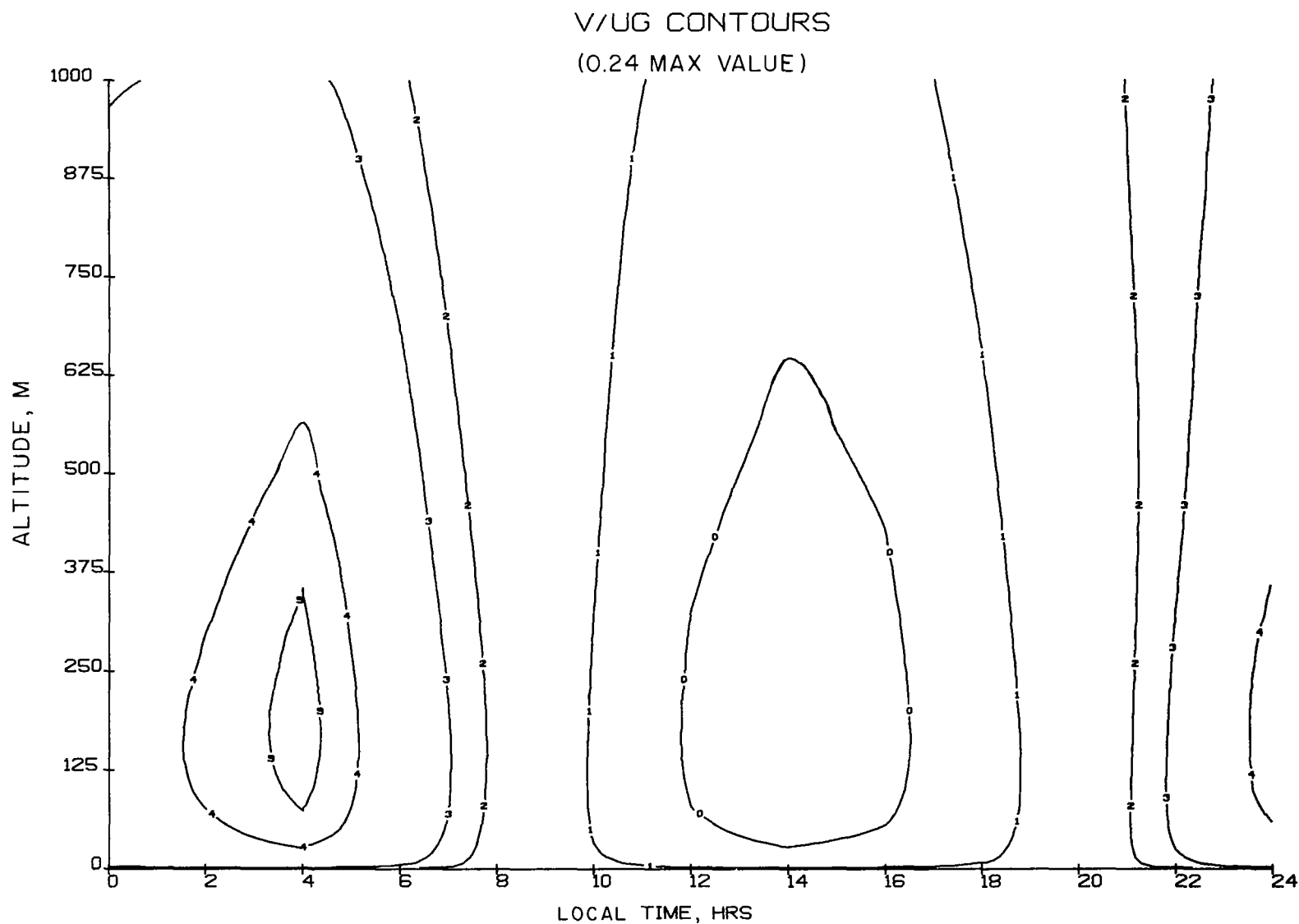


Figure 9. Isolines of the component of the mean wind in the direction normal to the geostrophic wind for the conditions of figure 8.

a value of 2.0 km for the 24-hour period to 1.2 km for the 12-hour period case.

Stability Variations

Although we expect the dynamics of the changing boundary conditions to be important for most real stability variations in the atmosphere, we will first consider the quasi-steady case where the surface heat flux is held constant. Figures 10 and 11 show the wind profiles for 4 different stability conditions with Ro held constant at 10^6 . When the bulk Richardson number defined by eq. (15) is positive, the flow is stable and the turbulence damped. As shown in figures 10 and 11, $\text{Ri}_{(10)} = 0.0135$ produces a boundary layer which is significantly smaller than the neutral case of $\text{Ri}_{(10)} = 0$, as should be expected for damped turbulence. This also produces a stronger transverse wind component, as seen in figure 11. Although the wind shear at the surface is reduced by the increase in stability, the wind shear a short distance above the surface is significantly increased. Thus, from the point of view of the wind shear which an aircraft may encounter, an increase in $\text{Ri}_{(10)}$ is quite likely to be associated with increased wind shear.

As outlined in the previous section, the specification of $\text{Ri}_{(10)}$ alone is not sufficient to determine the unstable profile ($\text{Ri}_{(10)} < 0$) even in the quasi-steady case. Figures 10 and 11 show two wind profiles for nearly the same negative value of $\text{Ri}_{(10)}$ and two quite different values of the inversion height. The unstable layer, driven by a positive surface heat flux, must be capped by a stable, temperature inversion layer if the boundary layer is to reach a quasi-steady state. The figures show that in addition to the shear layer at the surface, a shear layer is also developed in the vicinity of the temperature inversion. As may be noted in the discussion of the boundary conditions in a prior section, z_i is not a rigid lid but is defined as the altitude at which the maximum values of $\overline{\theta^2}$ occur as the temperature inversion is asymptotically approached. In between the surface shear layer and the inversion layer, the layer is relatively uniformly mixed.

The vertical velocity variance is shown in figure 12 for the unstable cases but with the normalization which is appropriate for free convection when there is no mean wind shear. The limiting profile for $\text{Ri}_{(10)} \rightarrow -\infty$, as predicted by our model, was shown in reference 8 to agree very well with laboratory simulations of this limit. Figure 12 shows that it does not require a very negative $\text{Ri}_{(10)}$ to approach this limiting distribution. The corresponding values of the Zilitinkevich parameter μ are also given.

Next we consider the diurnal variations which may be expected to occur on a typical summer day in the midwestern United States.

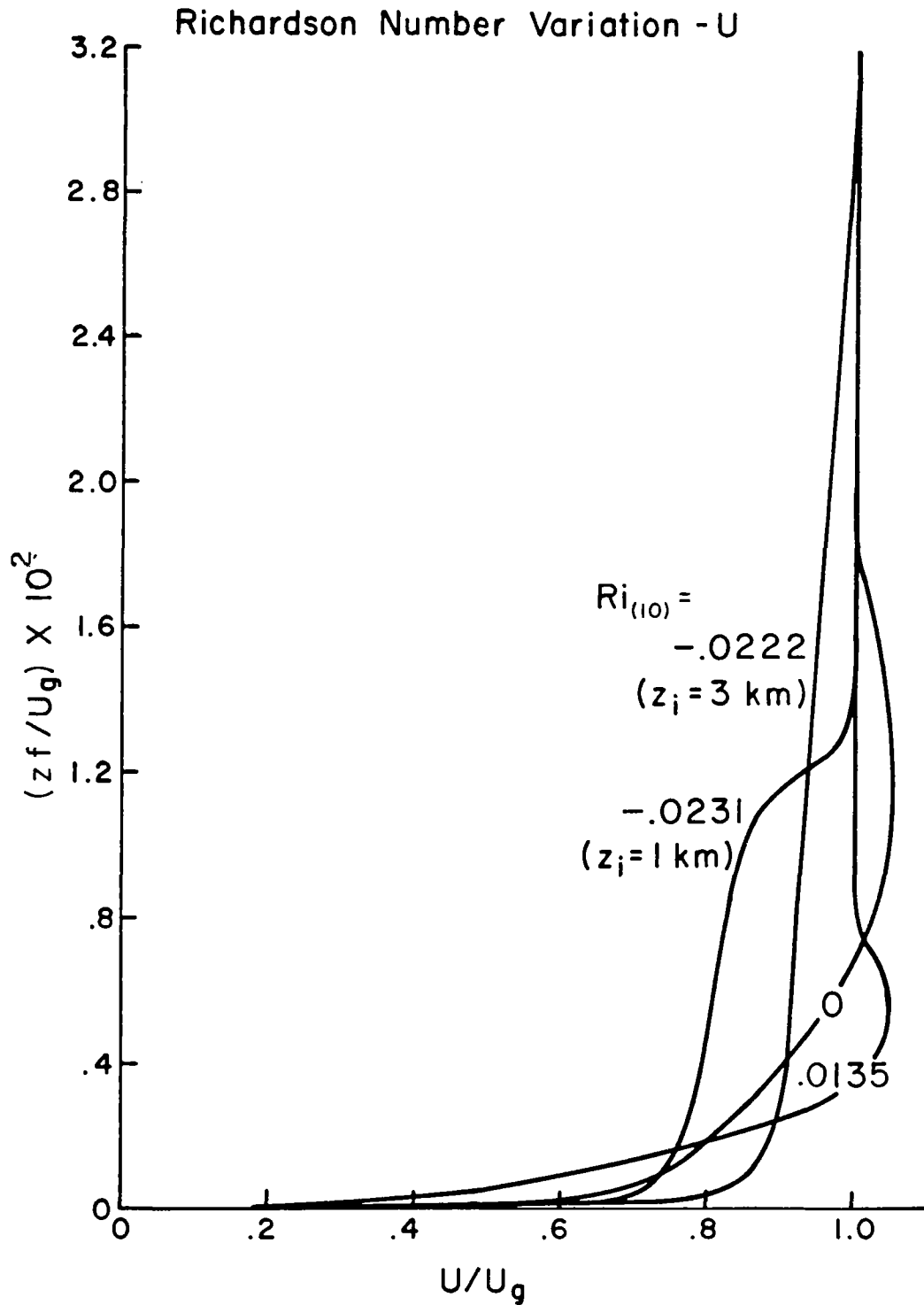


Figure 10. Influence of Richardson number on the quasi-steady distributions of mean wind component in the direction of the geostrophic wind ($Ro = 10^6$, $G_A = M = \mu_r = 0$).

Richardson Number Variation - V

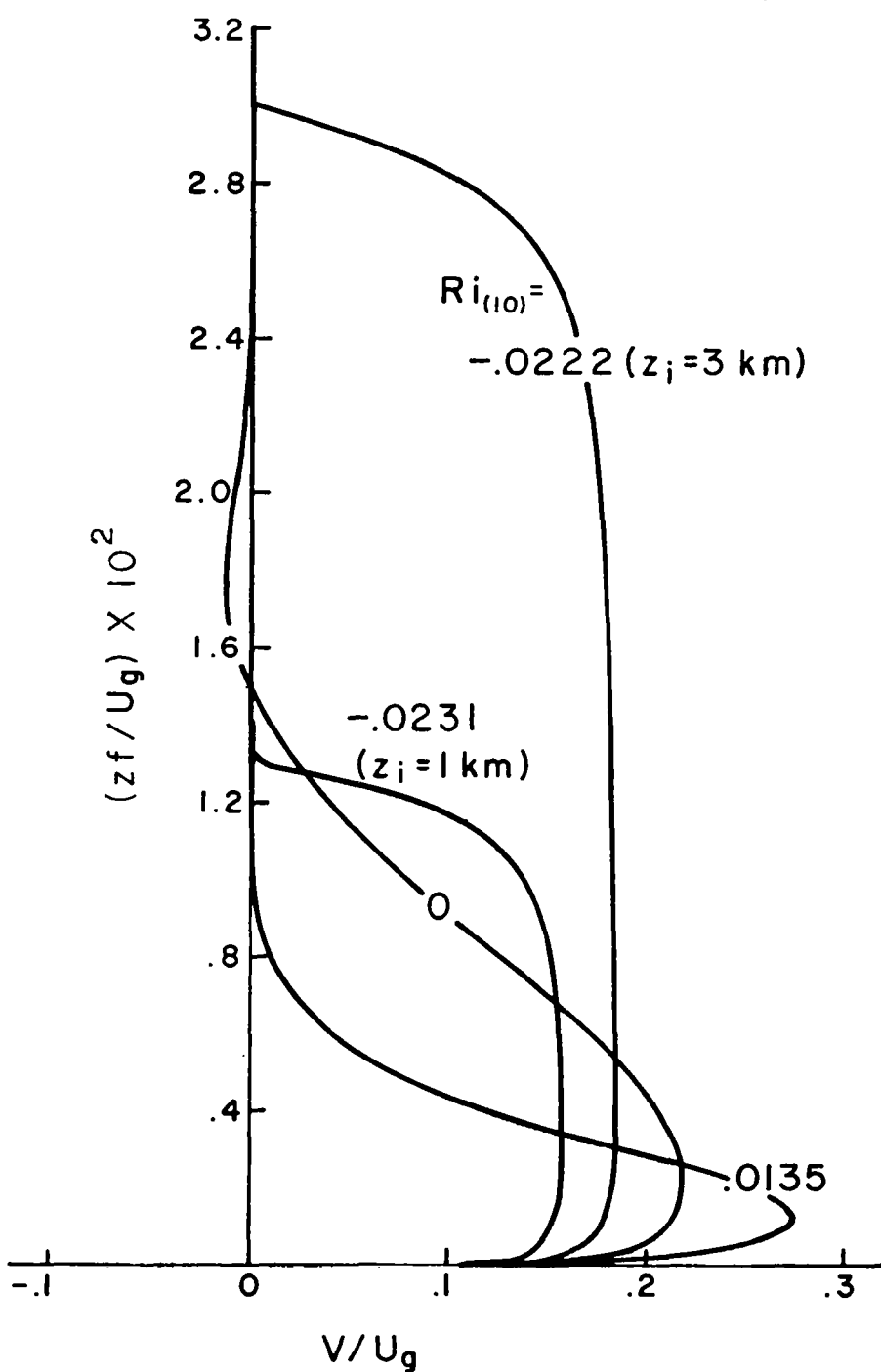


Figure 11. Influence of Richardson number on the quasi-steady distributions of mean wind component in the direction normal to the geostrophic wind for the conditions of figure 10.

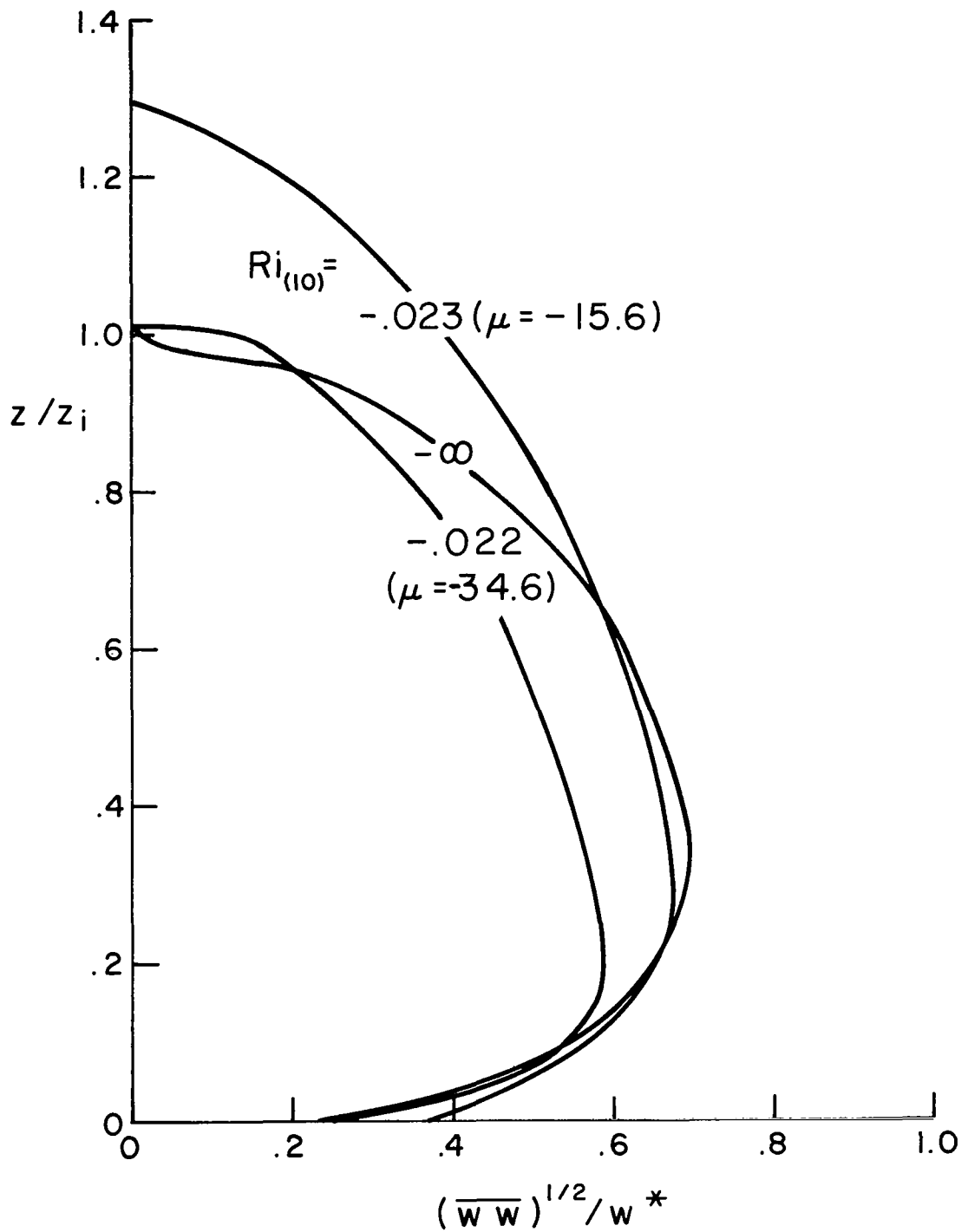


Figure 12. Vertical velocity variance for unstable conditions compared with the limiting profile for free convection ($G_A = M = \mu_r = 0$).

We have published results for this case (see refs. 5 and 6). In figures 13 through 16, the isolines of U , V , q^2 , and Λ are shown for a day's cycle for the lowest 1 km altitude. The notation for the isolines is given in Table II. In figures 13b and 14b, we also show the vertical profile of the wind components at selected times to aid in visualizing the changes. In the plots given previously for quasi-steady conditions, it was possible to present results in terms of a dimensionless height, zf/U_g . However, in the present case, since the dynamics of the diurnal variation is important in determining the height of the layer at any given time, this nondimensionalization is no longer valid. The results of all runs involving true time variations in hours will be given in terms of altitude in meters. For this run, the geostrophic wind was held constant at $U_g = 10$ m/sec, the upper level temperature gradient was held constant at $(\partial\theta/\partial z)|_\infty = 3^\circ\text{C}/\text{km}$, the surface roughness constant at $z_0 = .01$ m, and the surface heat flux was allowed to follow an experimentally observed distribution (ref. 19). Between sunset and sunrise, the heat flux is a negative constant ($-0.025^\circ\text{C m/sec}$) and between approximately 8:00 A.M. and 8:00 P.M., the heat flux is positive and nearly follows a sine wave with a maximum of 0.25°C m/sec . Over the 24-hour cycle, there is a net positive heat flux to the atmosphere which must be removed (in simulation of long wave radiation) in order to achieve a periodic solution with no long-term heating of the boundary layer. In the present run, this was accomplished by assuming \dot{Q}_r distributed uniformly over the night hours with the following assumed vertical distribution:

$$\dot{Q}_r = -0.703 \times 10^{-4} \cos(\pi z/6000 \text{ m}) (\text{°C/sec}) \quad z \leq 3000 \text{ m}$$

$$\dot{Q}_r = 0 \quad z > 3000 \text{ m}$$

Figures 13 and 14 show the wind shear to be a maximum in the early morning hours when the turbulence, as shown in figure 15, is a minimum. There is a low-level nocturnal jet which exceeds the geostrophic wind by 14% at a little above 100 m altitude. The wind at this time drops from 11.4 m/sec to 3 m/sec at 10 m altitude at the same time the principal wind direction is shifting by 40 degrees.

A lower scale on the q^2 plot (fig. 15) indicates the value of the first Zilitinkevich parameter μ_o as a function of time. It is readily observed that the values of q^2 occurring when $\mu_o = 0$ in the morning are quite different from those occurring for $\mu_o = 0$ in the evening.

Figure 16 shows the isolines of the turbulent macroscale Λ . Near the ground, Λ increases nearly proportionally to altitude, except in the nocturnal hours when the larger turbulent eddies are preferentially damped. This forces the turbulent scale to be less

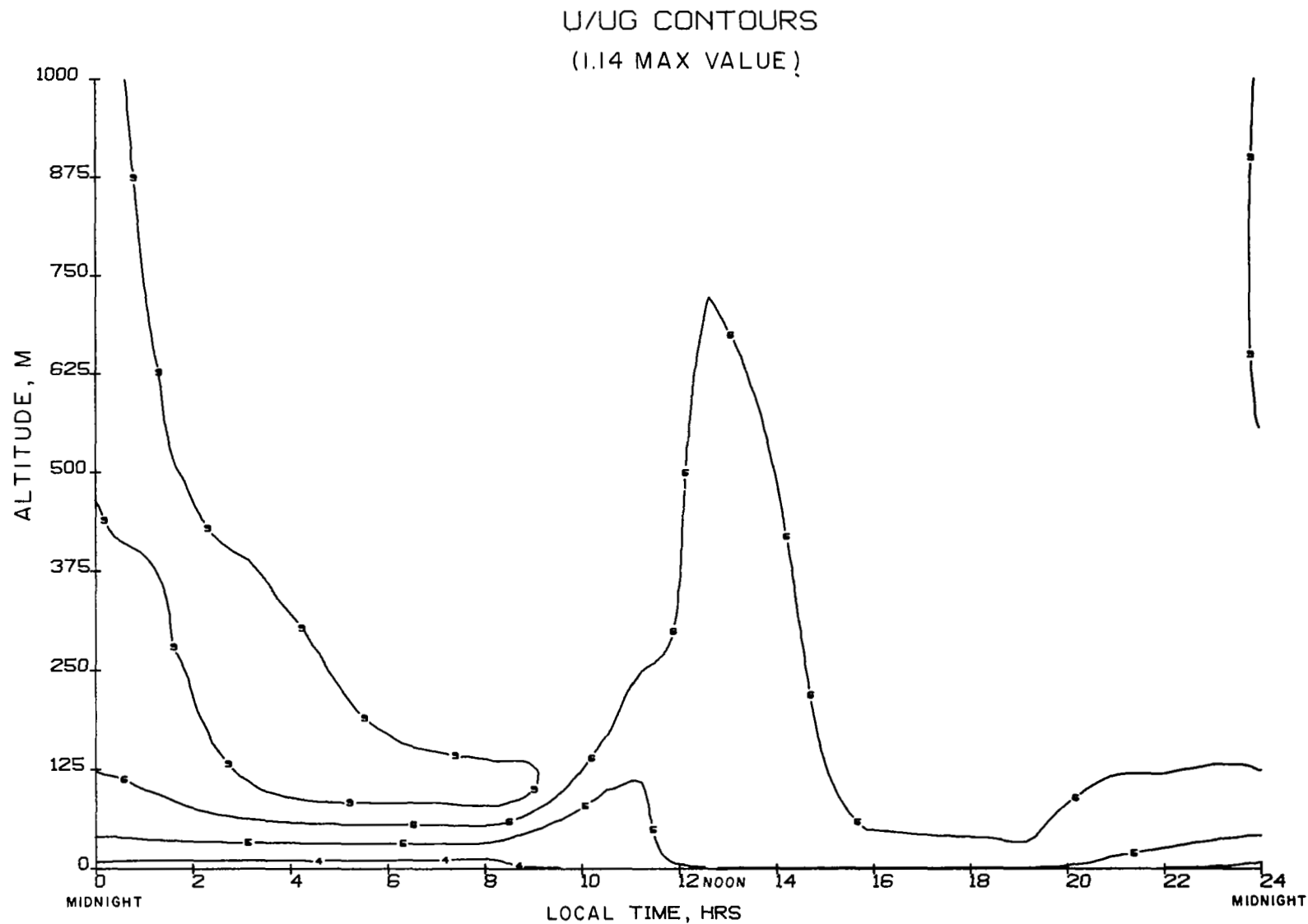


Figure 13a. Isolines of the component of the mean wind in the direction of the geostrophic wind for a standard summer day in midwestern United States ($\text{Ro} = 10^7$, $M = G_A = 0$).

U/UG PROFILE

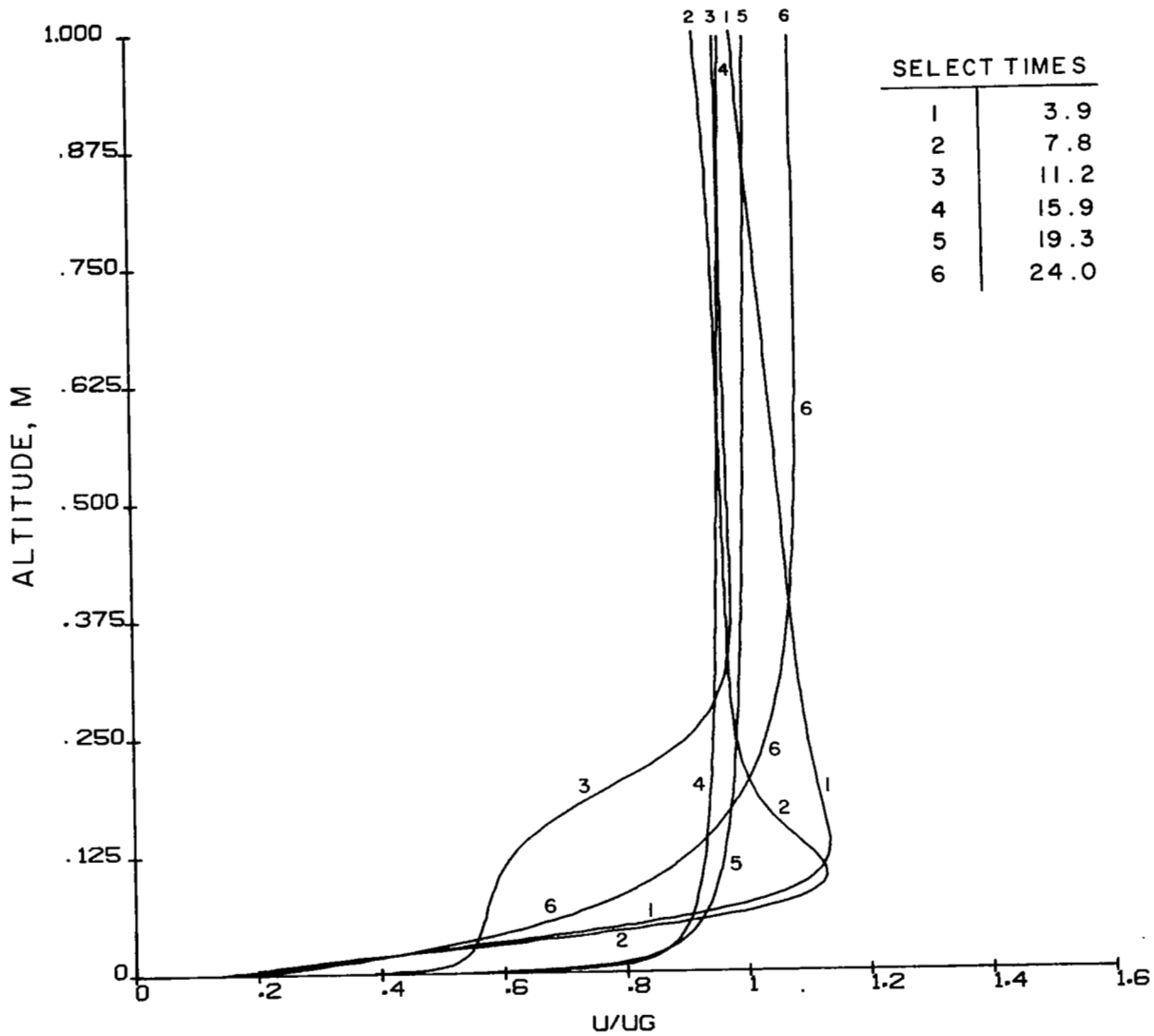


Figure 13b. Vertical distributions of u taken at select times from figure 13a.

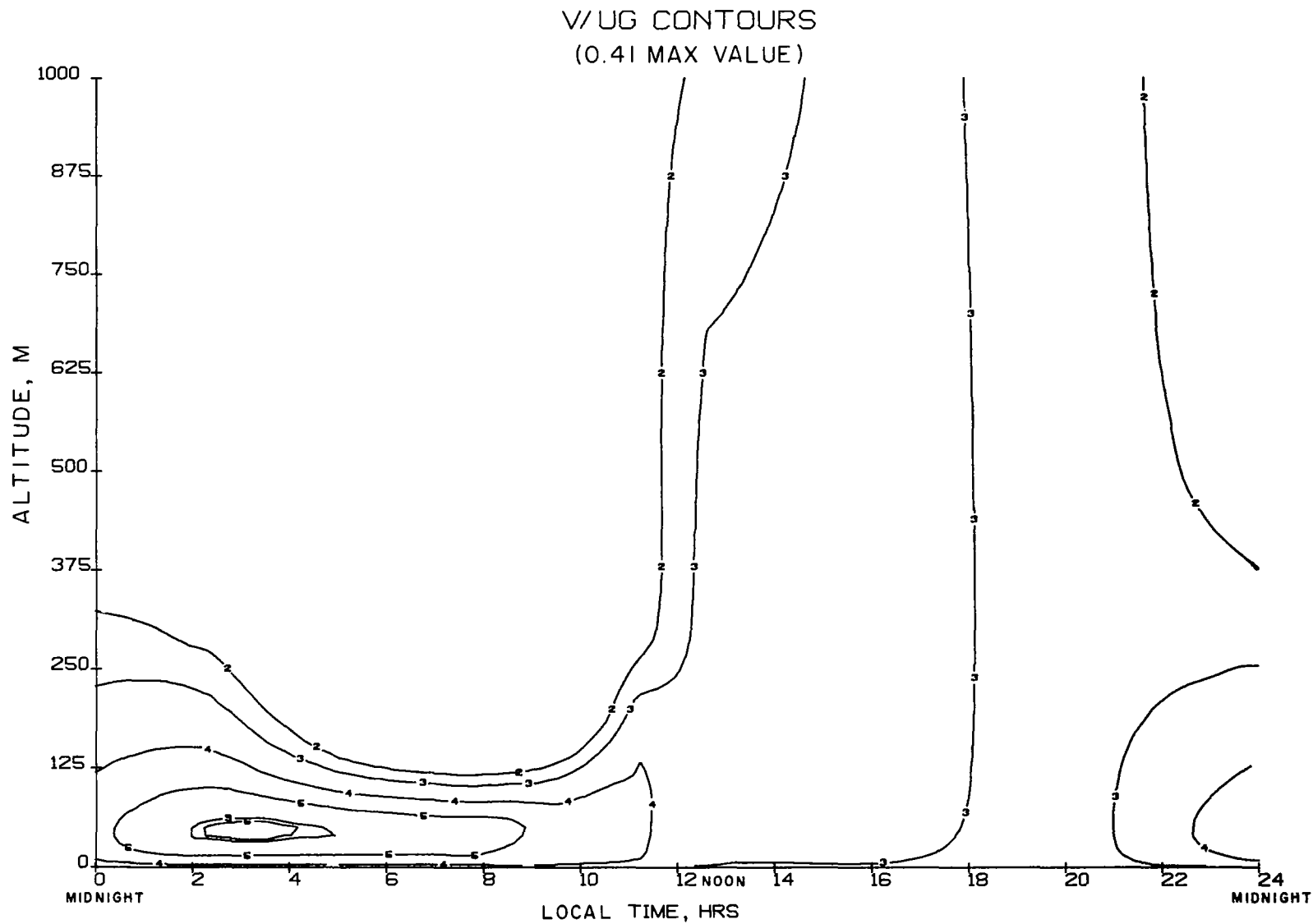


Figure 14a. Isolines of the component of the mean wind in the direction normal to the geostrophic wind for the conditions of figure 13.

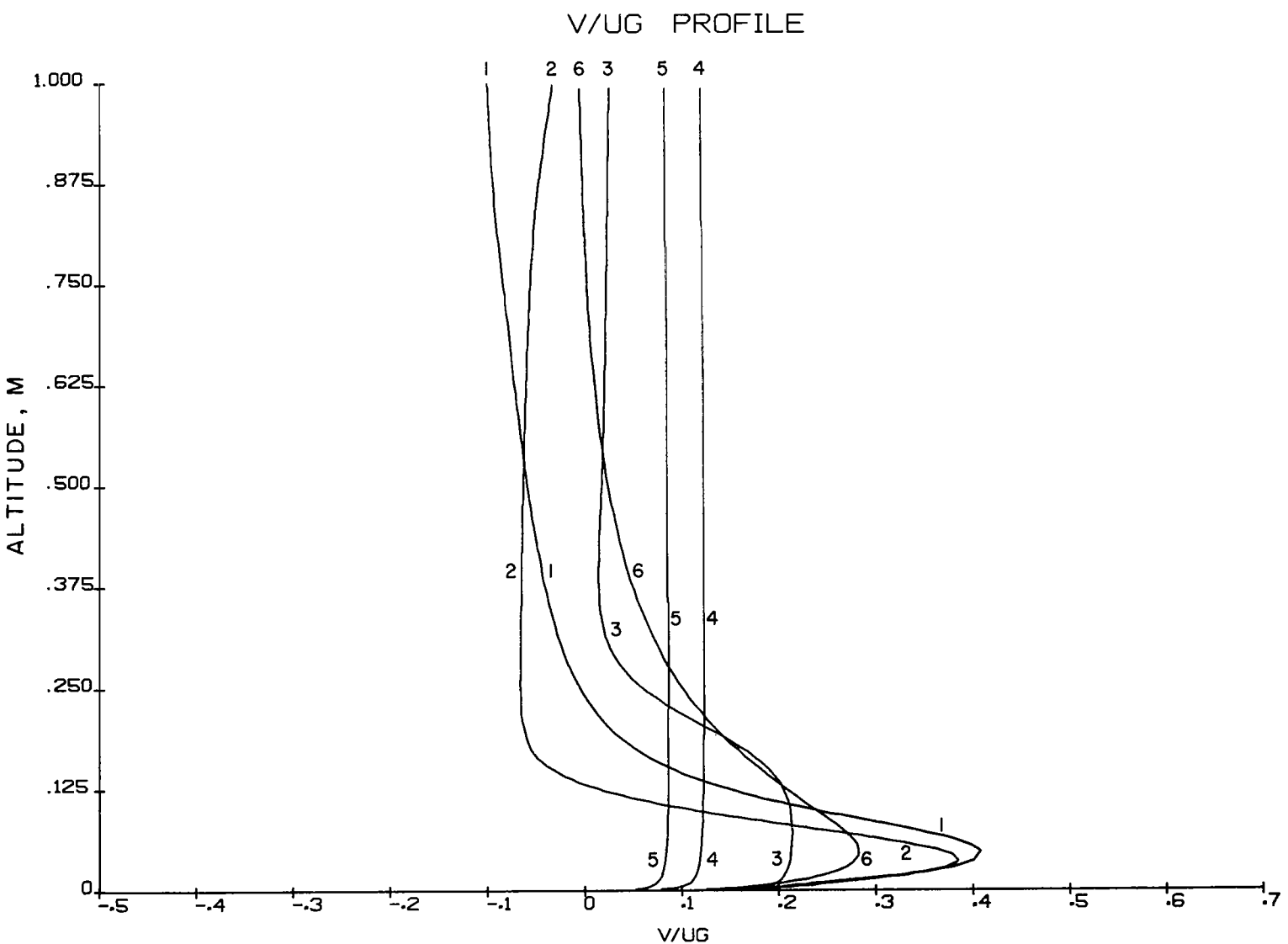


Figure 14b. The vertical distributions of v taken at select times from figure 14a.

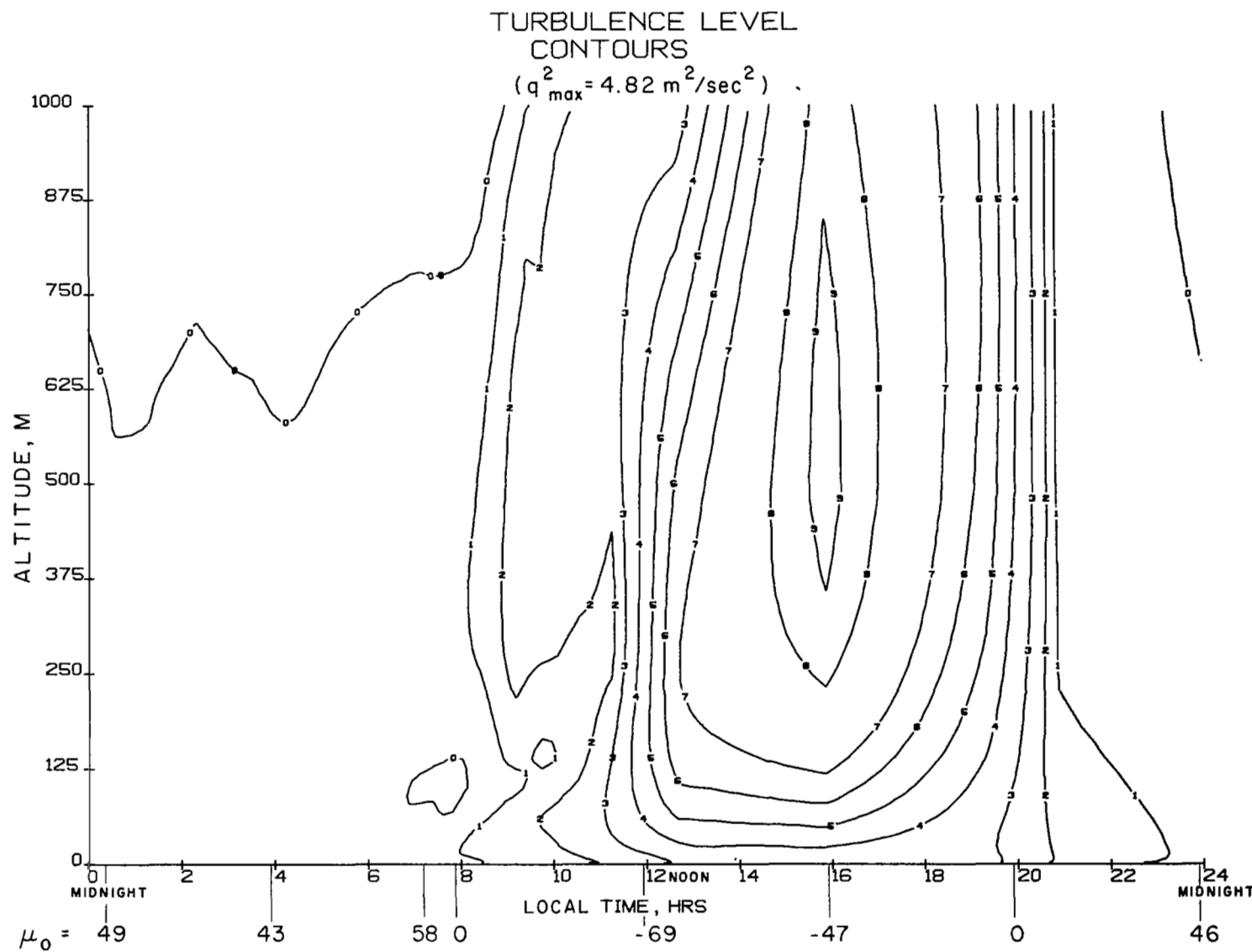


Figure 15. Isolines of turbulence intensity q^2 for the conditions of figure 13.

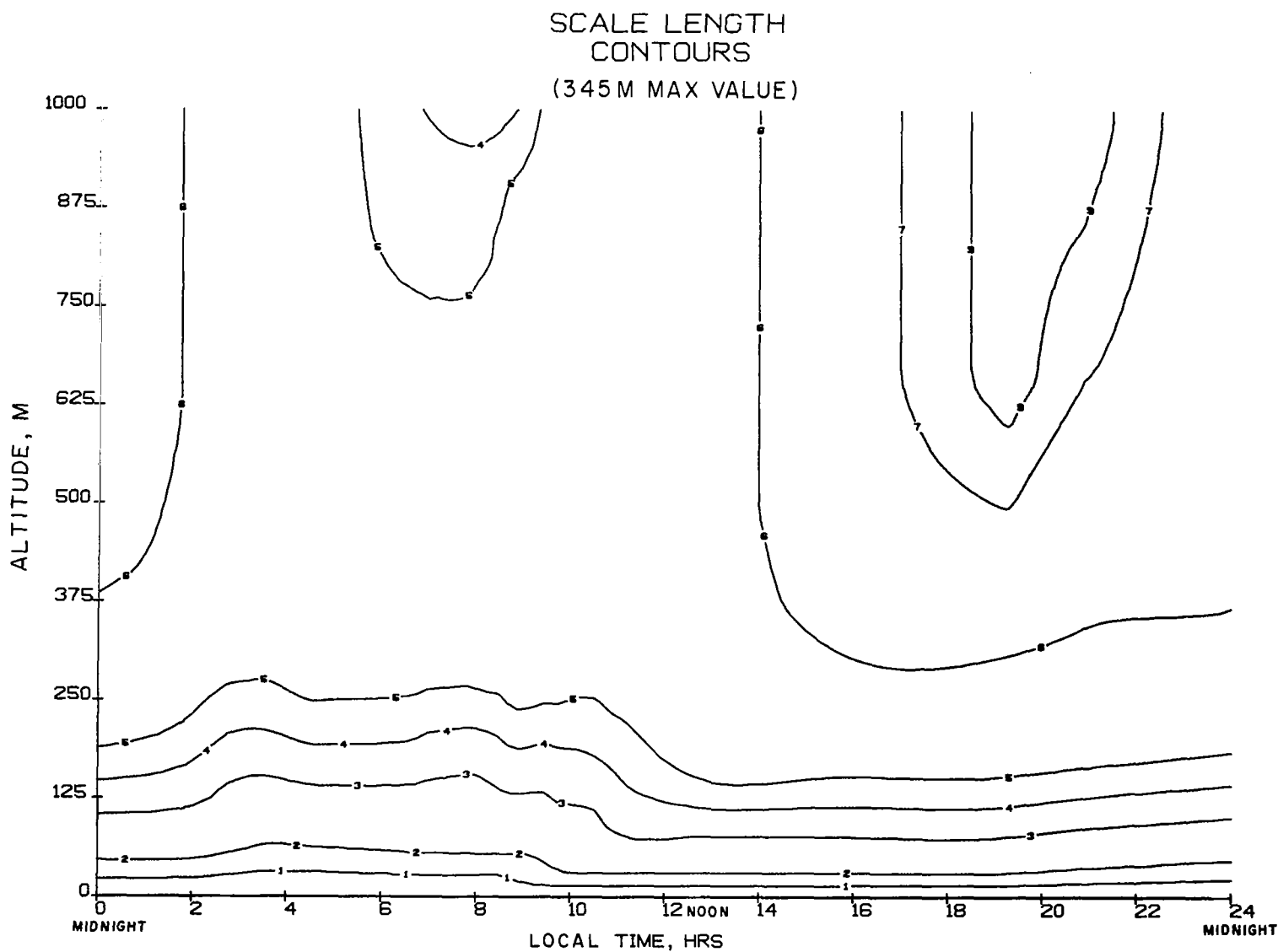


Figure 16. Isolines of turbulence macroscale Λ for the conditions of figure 13.

at the same altitude than it is during the daytime hours and is reflected in figure 16 as a rise in the isolines during the nocturnal hours. At moderate altitudes, the scale remains relatively large even during the early morning hours. However, as noted from figure 15, this is associated with very low intensity turbulence. So the flow is very nearly laminar even though the scale of what turbulence remains is large.

Very little difference is observed if only the upper-level temperature gradient is changed. A run was made with conditions identical to the preceding run with the exception of $(\partial\theta/\partial z)|_{\infty}$ changed from $3^{\circ}\text{C}/\text{km}$ to the isothermal value of $9.87^{\circ}\text{C}/\text{km}$. The resulting wind and turbulence distributions showed no significant differences from those given in figures 13 through 16. Even the value of the height of the upper-level inversion which was achieved when the flow became periodic was surprisingly close to that of the previous run.

Figures 17 through 20 show the variation caused in the diurnal fluctuations if the afternoon positive heat flux is reduced in addition to increasing the upper-level lapse rate. For this run, the surface heat flux was taken as exactly symmetrical in time so there is no need for a radiation flux divergence term to make the boundary layer periodic. We specified $w\theta|_0 = .025 \sin(\pi/12)(t-8 \text{ hrs})$ and $z_0 = 0.1 \text{ m}$. Also the upper-level potential temperature gradient is increased from $3^{\circ}\text{C}/\text{km}$ to the isothermal value of $9.87^{\circ}\text{C}/\text{km}$. Other conditions are the same as for figures 13 through 16. In both cases, the flow is permitted to run through three complete cycles to eliminate any influence of the initial conditions. The third cycle appears quite close to periodic and is the result shown.

There is considerably less time variation in the turbulence level shown in figure 19. There is neither sufficient heating in the afternoon to force the large ballooning of the turbulence intensity to higher levels seen in figure 15 nor sufficient cooling at night to strongly damp the turbulence. However, as seen in figures 17 and 18, the wind distribution is markedly different from either the standard day variation of figures 13 and 14 or the neutral, steady-state profiles of figures 1 and 2. The low-level nocturnal jet is actually increased to 13.1 m/sec and occurs at a somewhat higher altitude, as seen by comparing figures 13 and 17. This is an example of how difficult it is to track through all the nonlinearities in the equations and anticipate the results of some particular change.

The macroscale in figure 20 is reduced throughout the day to a value which is even less than that for a steady-state, neutral boundary layer. This may be a result of the imposed temperature inversion which was initially started at 100 m altitude. In the standard day run (figs. 13-16), the temperature inversion was

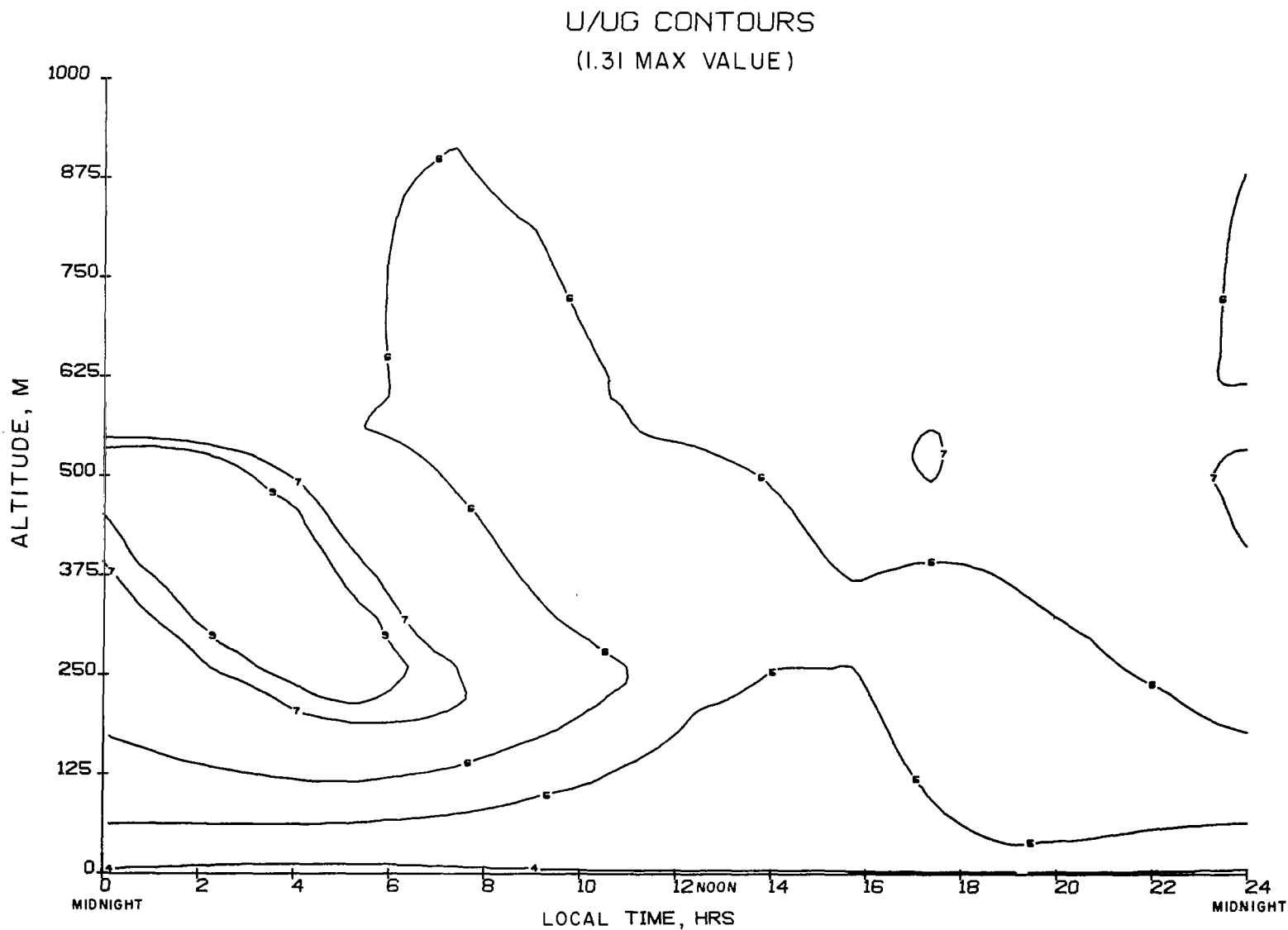


Figure 17a. Isolines of u for a reduced symmetrical, periodic, heat flux and an increased upper-level temperature gradient ($\text{Ro} = 10^6$, $M = G_A = 0$).

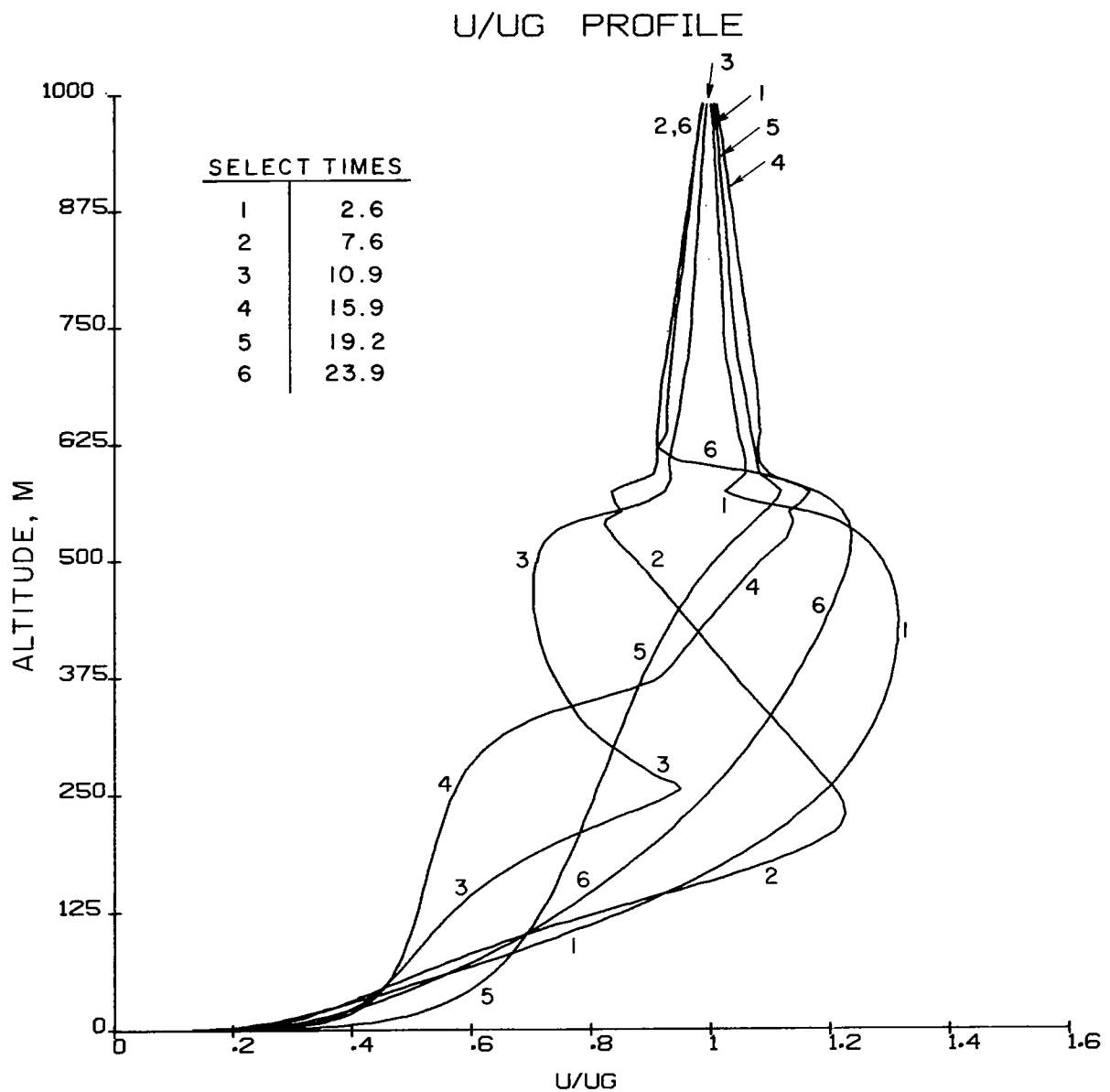


Figure 17b. Vertical distributions of u taken at select times from figure 17a.

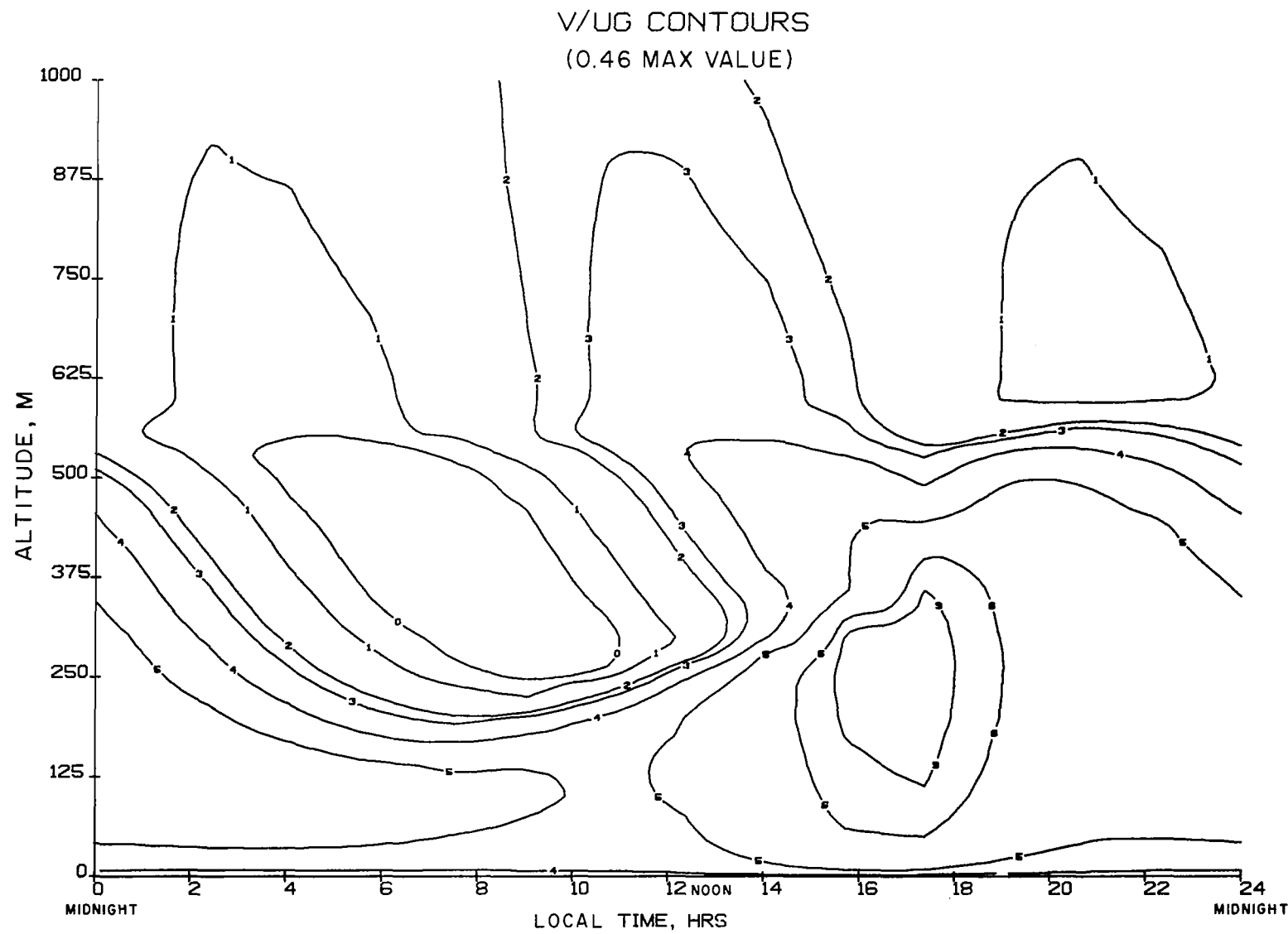


Figure 18a. Isolines of v for the conditions of figure 17.

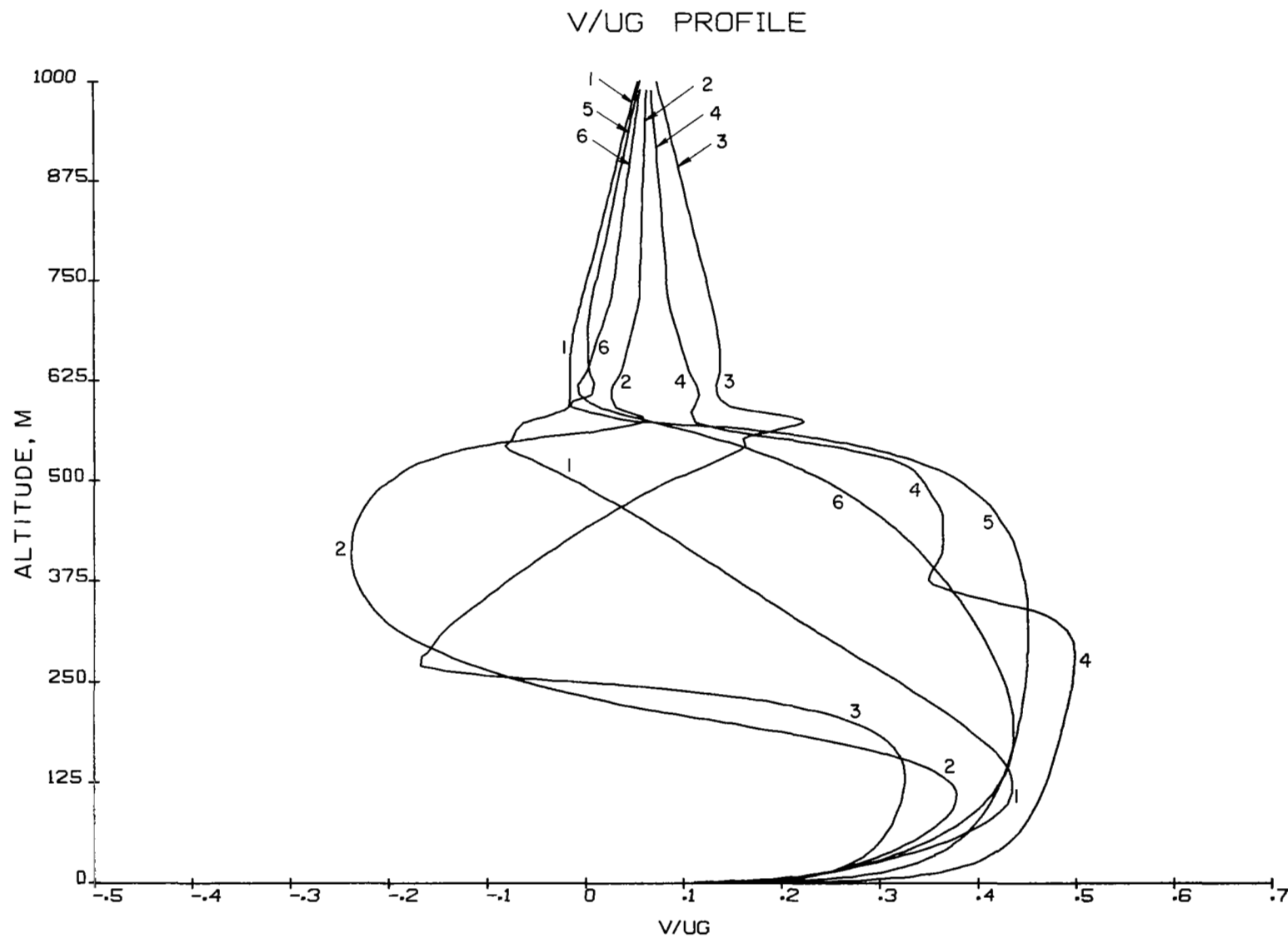


Figure 18b. Vertical distributions of v taken at select times from figure 18a.

TURBULENCE LEVEL
CONTOURS

($q^2_{\max} = 1.18 \text{ m}^2/\text{sec}^2$)

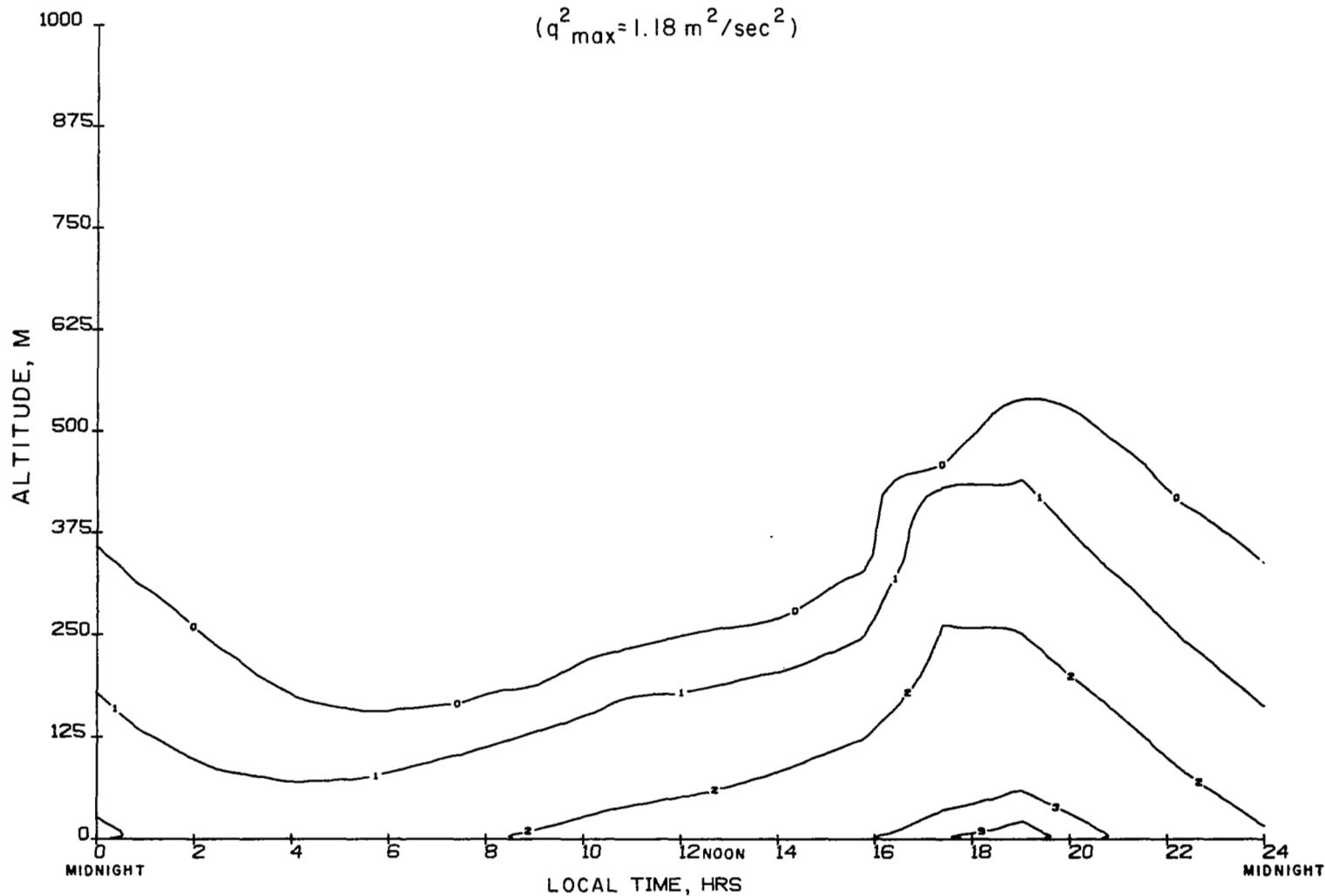


Figure 19. Isolines of turbulence intensity q^2 for the conditions of figure 17.

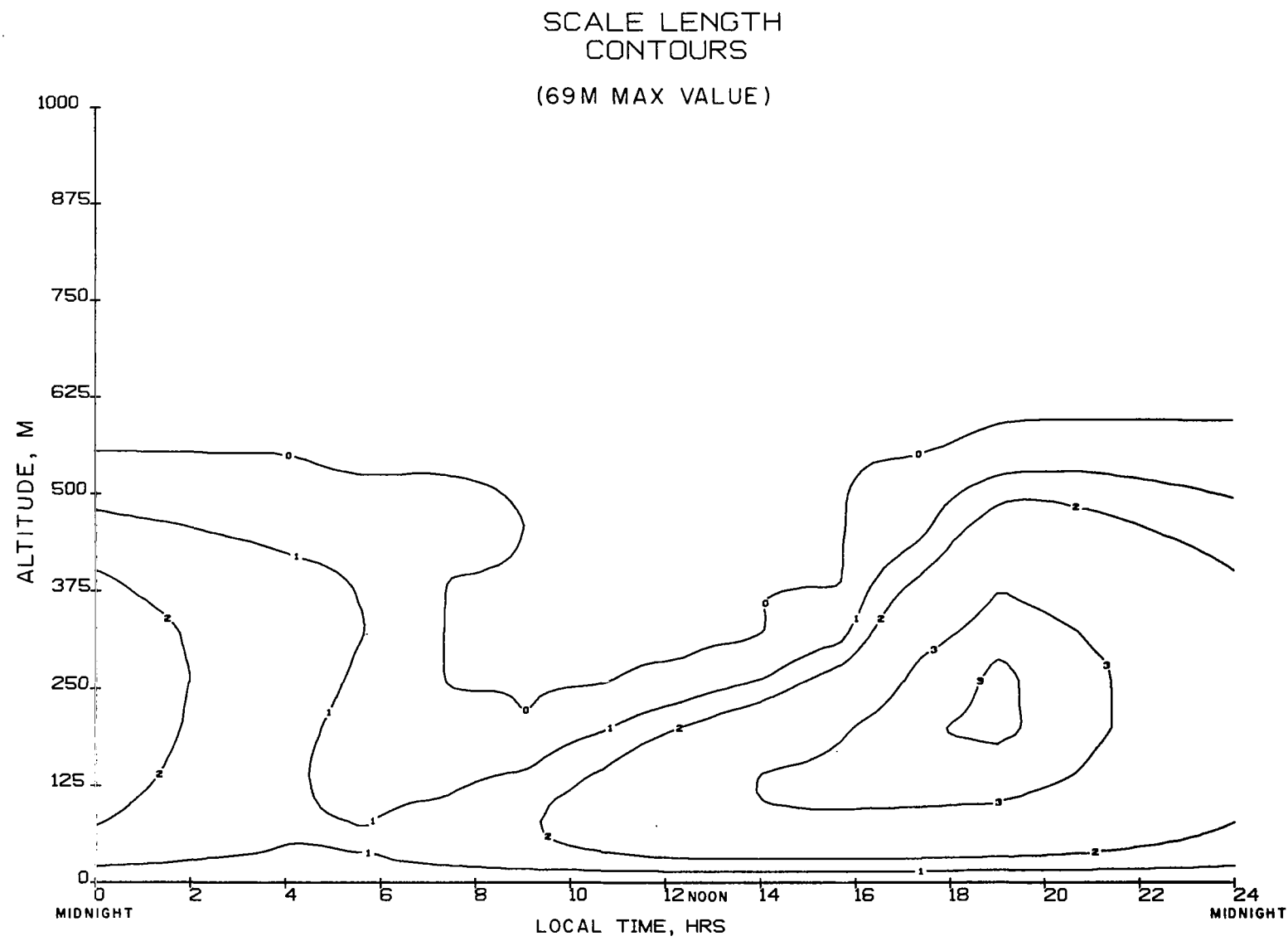


Figure 20. Isolines of turbulence macroscale Λ for the conditions of figure 17.

raised by the turbulence to approximately 3 km. The reduced surface heat flux of the present case only pushes the inversion to approximately 500 m altitude. This is much less than the height of the neutral, steady-state boundary layers shown in figures 11 through 16. It appears to permit the natural inertial oscillations to play a more important role, particularly in the transverse wind component V .

Influence of Baroclinicity

The approximation of horizontal, spatial inhomogeneity is seldom completely realized in the atmosphere. One effect which perhaps is most often encountered is that of horizontal temperature gradients. Fortunately, this effect can be incorporated within the one-dimensional model by permitting the pressure gradient, represented in eqs. (1) and (2) in terms of geostrophic velocities, to vary with altitude. This "thermal wind" variation in the geostrophic wind can be obtained directly from the geostrophic balance by differentiating and using the equation of state

$$\frac{\partial U}{\partial z} \frac{g}{f\theta_0} = - \frac{g}{f\theta_0} \frac{\partial \theta}{\partial y} \quad (20)$$

$$\frac{\partial V}{\partial z} \frac{g}{f\theta_0} = \frac{g}{f\theta_0} \frac{\partial \theta}{\partial x} \quad (21)$$

with x in the direction of U_g at the top of the boundary layer. If temperature advection is to be included in the energy equation, then the source term in eq. (3) should include a term of the form

$$\dot{Q} = -u \frac{\partial \theta}{\partial x} - v \frac{\partial \theta}{\partial y} = - \frac{f\theta_0}{g} \left(U \frac{\partial V}{\partial z} \frac{g}{f\theta_0} + V \frac{\partial U}{\partial x} \frac{g}{f\theta_0} \right) \quad (22)$$

We will consider the direct effect of the geostrophic wind shear in the momentum equation separately from the effect of temperature advection. Figures 21 through 24 show the results for $M = 1.25$. To include both the dynamics and the influence of different values of β_0 , we have allowed β_0 to vary from 0 to 2π and back to 0 in a period of 12 hours. The magnitude corresponds to a horizontal temperature change of 3°C in 100 km which appears as a not uncommon value in nature. The time variation corresponds to a relatively fast moving temperature anomaly, such as a thunderstorm at a distance. Again, the flow was permitted to become relatively periodic by allowing 3 full periods of variation before the results shown in the figures were recorded. For this first set of figures, the temperature is uniform between the surface and the inversion layer at approximately 1250 m altitude.

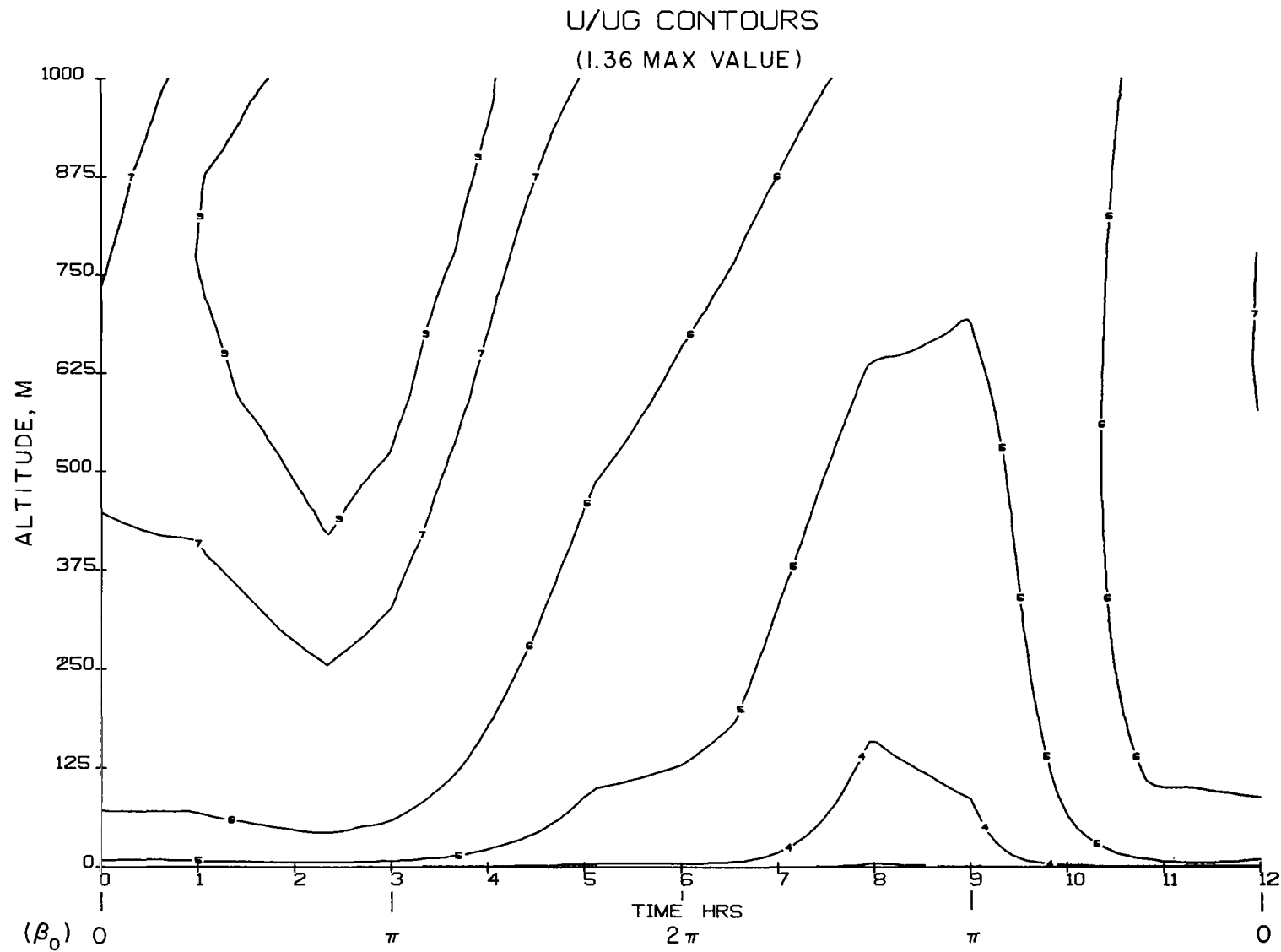


Figure 21. Isolines of u for a thermal wind varying periodically in direction ($Ro = 10^6$, $\partial\theta/\partial z|_\infty = 3^\circ\text{C}/\text{km}$, $M = 1.25$, $\mu_r = 0$, $Ri_{(10)} = 0$).

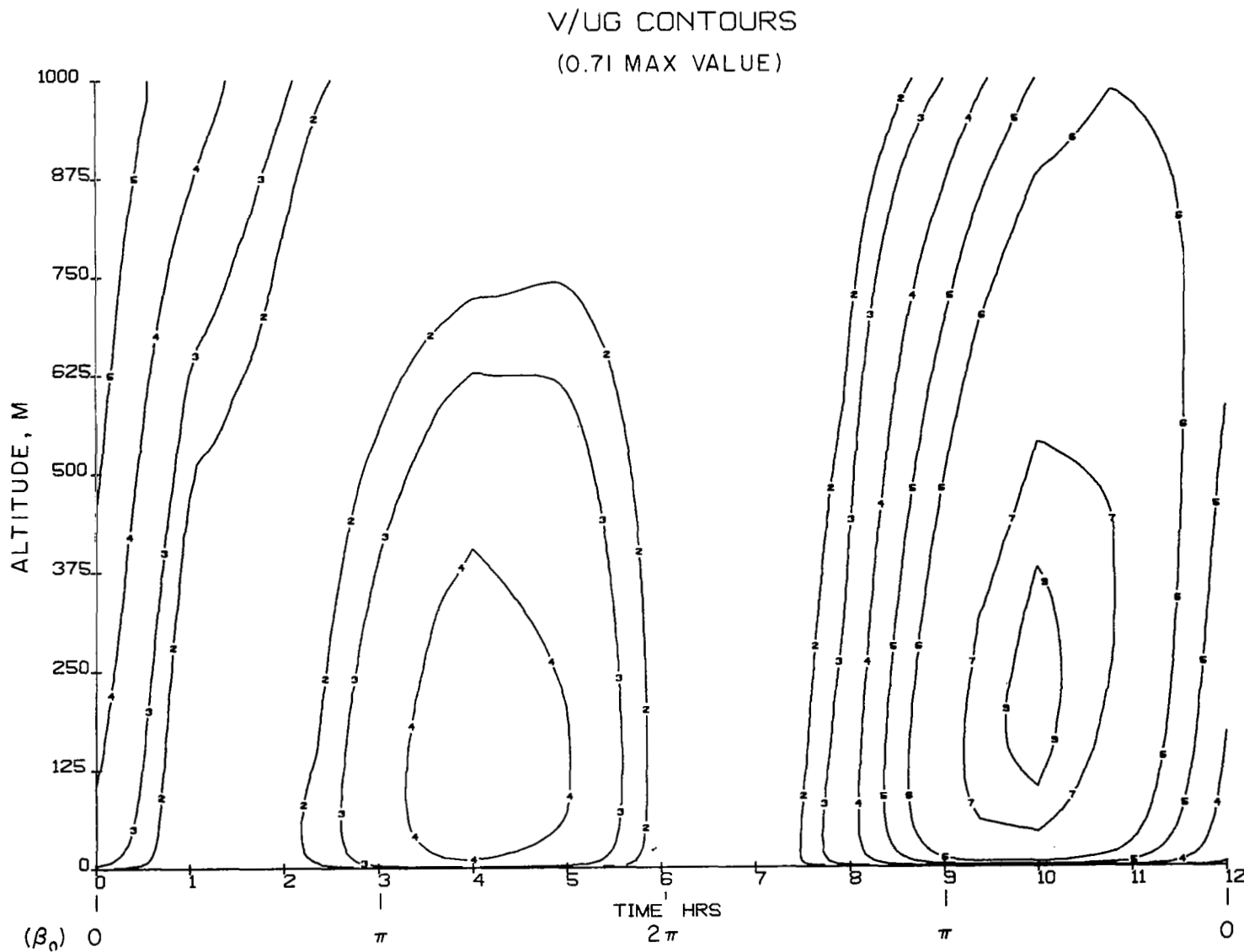


Figure 22. Isolines of v for the conditions of figure 21.

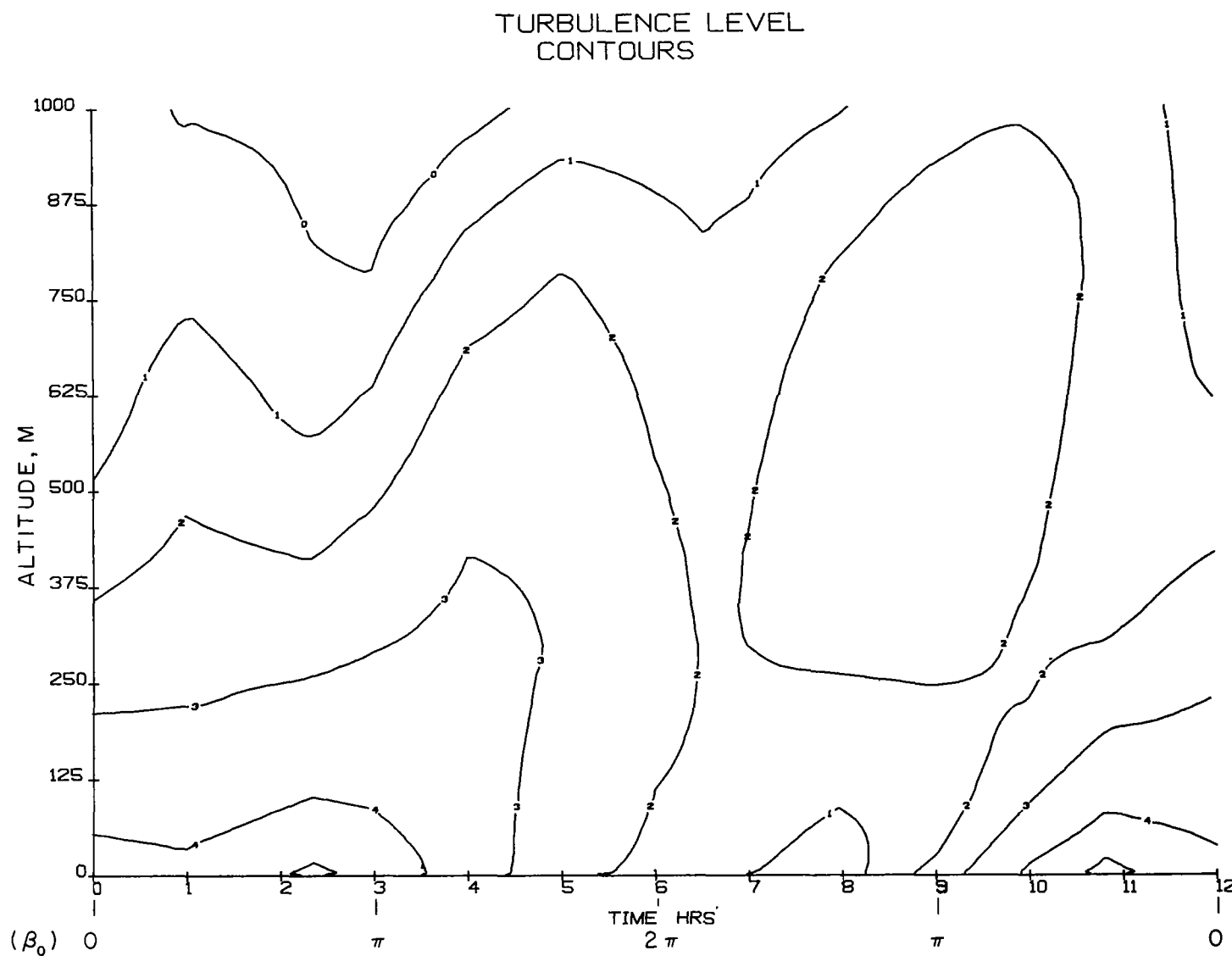


Figure 23. Isolines of turbulence intensity q^2 for the conditions of figure 21.

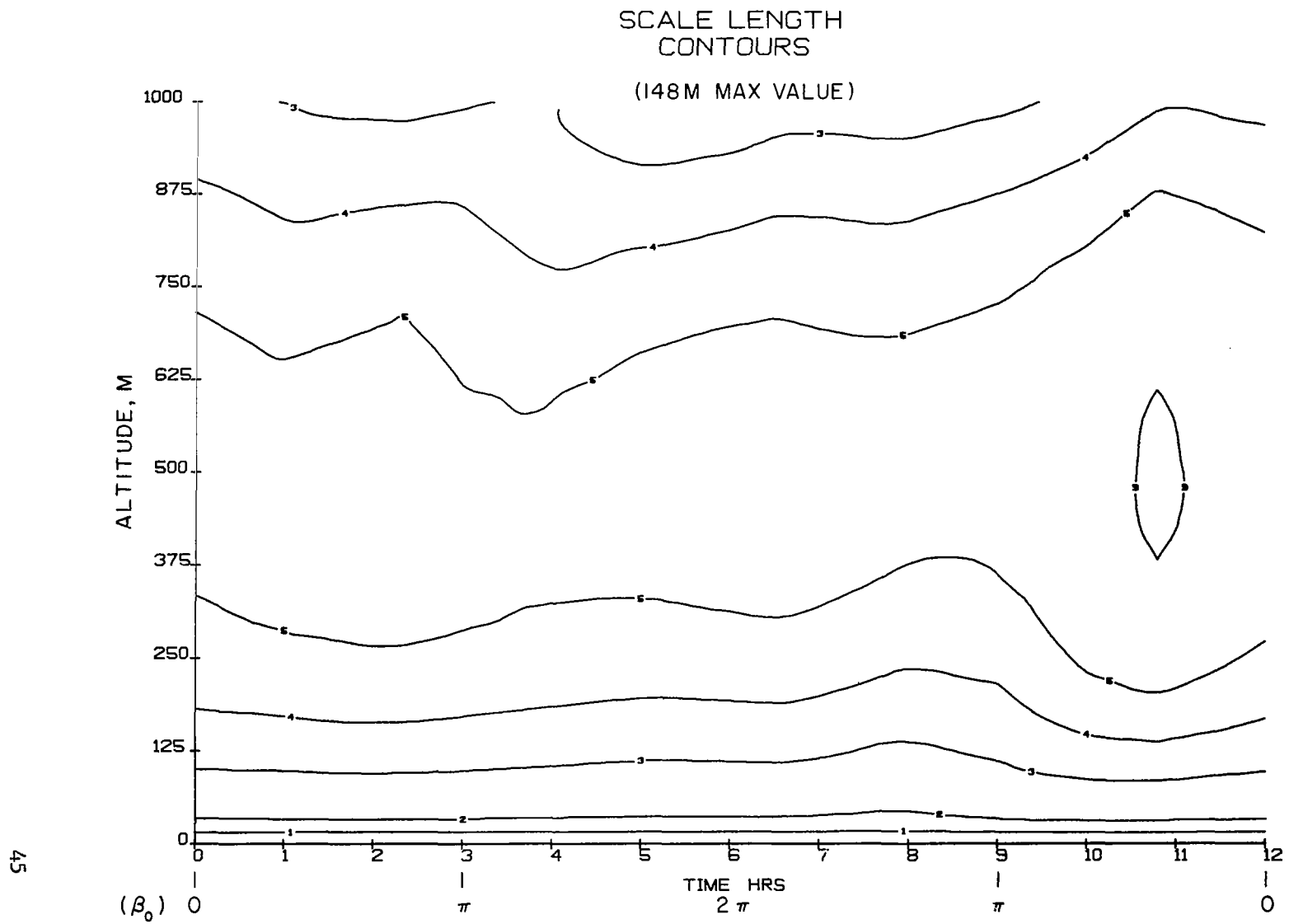


Figure 24. Isolines of turbulence macroscale Λ for the conditions of figure 21.

The maximum U velocity, 13.5 m/sec, occurs approximately 3 hours after the thermal wind is directed in the direction of the geostrophic wind ($\beta_0 = 0$). But 3 hours after the thermal wind is next directed in the same direction ($\beta_0 = 2\pi$), U is near a minimum. Actually, from eqs. (1) and (2) we see that the U velocity responds to variations in V_g and, since $\partial V_g / \partial z$ follows $\sin \beta t$, this contributes a positive pressure gradient in eq. (1) between $0 < \beta_0 < \pi$ and a negative pressure gradient between $\pi < \beta_0 < 2\pi$. Thus it is consistent for a maximum to occur in U when β_0 passes through π as it is increased and for a minimum to occur in U when β_0 passes through π as it is decreased. This particular time variation of driving conditions is not expected to occur long enough in nature to make the real flow periodic, but it does demonstrate how important the time history of the flow is in determining the response of the flow to instantaneous values of the driving conditions.

The maximum value of V , 7 m/sec, occurs near the 10-hour mark after the combination of a relative minimum in U and a maximum in U_g has produced a favorable pressure gradient (see eq. (2)) for a period of time. There is a region of slightly negative V (approx. -1 m/sec) between 1000 m and 1250 m altitude which does not show in figure 22. The turbulence isolines in figure 23 show no strong variation over the period. Neither do the isolines for Λ in figure 24, although there is a slight maximum occurring in Λ near the time that V has its local maximum.

The maximum wind shear at or above 10 m altitude computed by taking the square root of the sum of the squares of $\partial U / \partial z$ and $\partial V / \partial z$ gives a value of 0.14 sec^{-1} , somewhat less than the maximum value (0.18 sec^{-1}) that occurs in the typical day calculations of figures 13 and 14. However, in this case the shear occurs over a somewhat wider altitude range. Perhaps the more important difference is that in the earlier figures the strong local stability caused by surface cooling was the dominant mechanism while, in the present case, there is a neutral, vertical temperature variation in the region of maximum shear. This suggests two different ways in which the wind shear may be increased: either by increasing the horizontal wind gradients to increase the driving thermal winds or by applying a vertical temperature gradient which increases the stability of the flow under the same driving pressure gradients.

Figures 25 through 28 show the results of taking the same conditions as those for figures 21 through 24 and changing only the upper-level lapse rate from $3^\circ\text{C}/\text{km}$ to $6^\circ\text{C}/\text{km}$. As seen by comparing figures 21 and 25, the maximum U velocity is increased to 16.6 m/sec from 13.6 m/sec. Also from figures 22 and 26, the maximum V is increased from 7 to 10 m/sec. However, the resulting maximum shear still occurs near the surface with the value at 10 m altitude unchanged at 0.14 sec^{-1} .

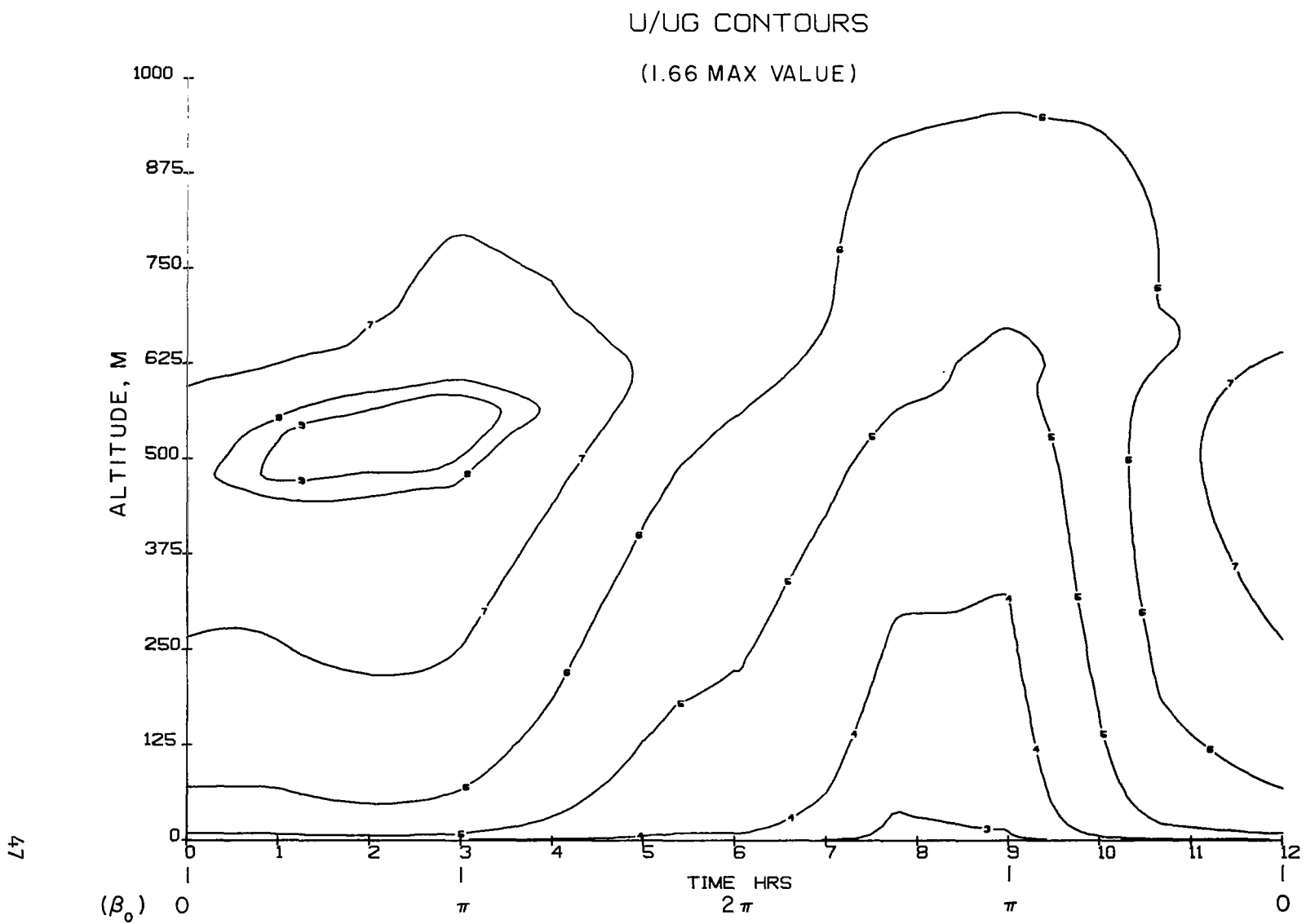


Figure 25. Isolines of u for the same thermal wind variation as in figure 21 but with $\partial\theta/\partial z|_\infty = 9.87^\circ\text{C}/\text{km}$ ($\text{Ro} = 10^6$, $M = 1.25$, $\mu_r = 0$, $Ri_{(10)} = 0$).

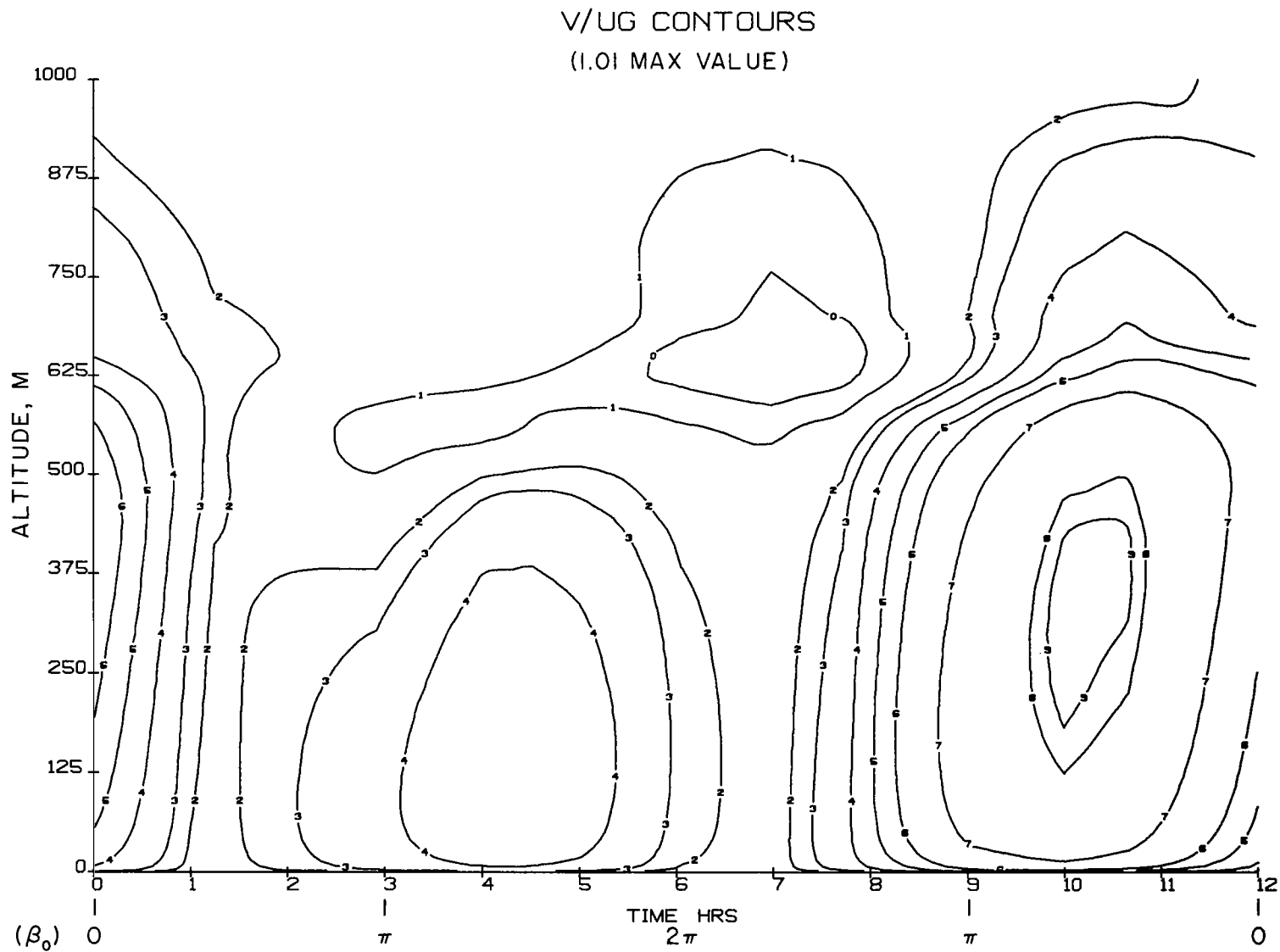


Figure 26. Isolines of v for the conditions of figure 25.

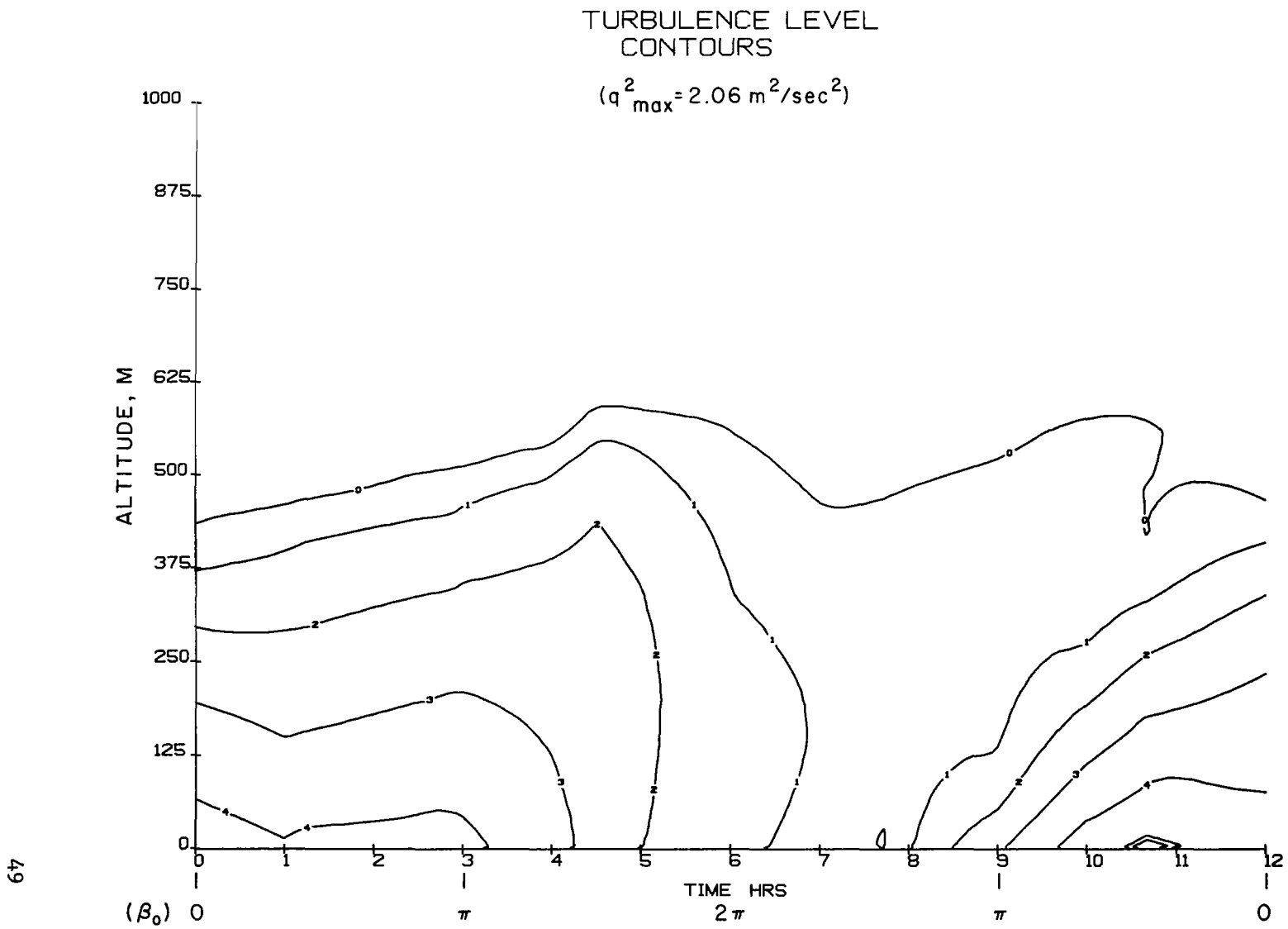


Figure 27. Isolines of turbulence intensity q^2 for the conditions of figure 25.

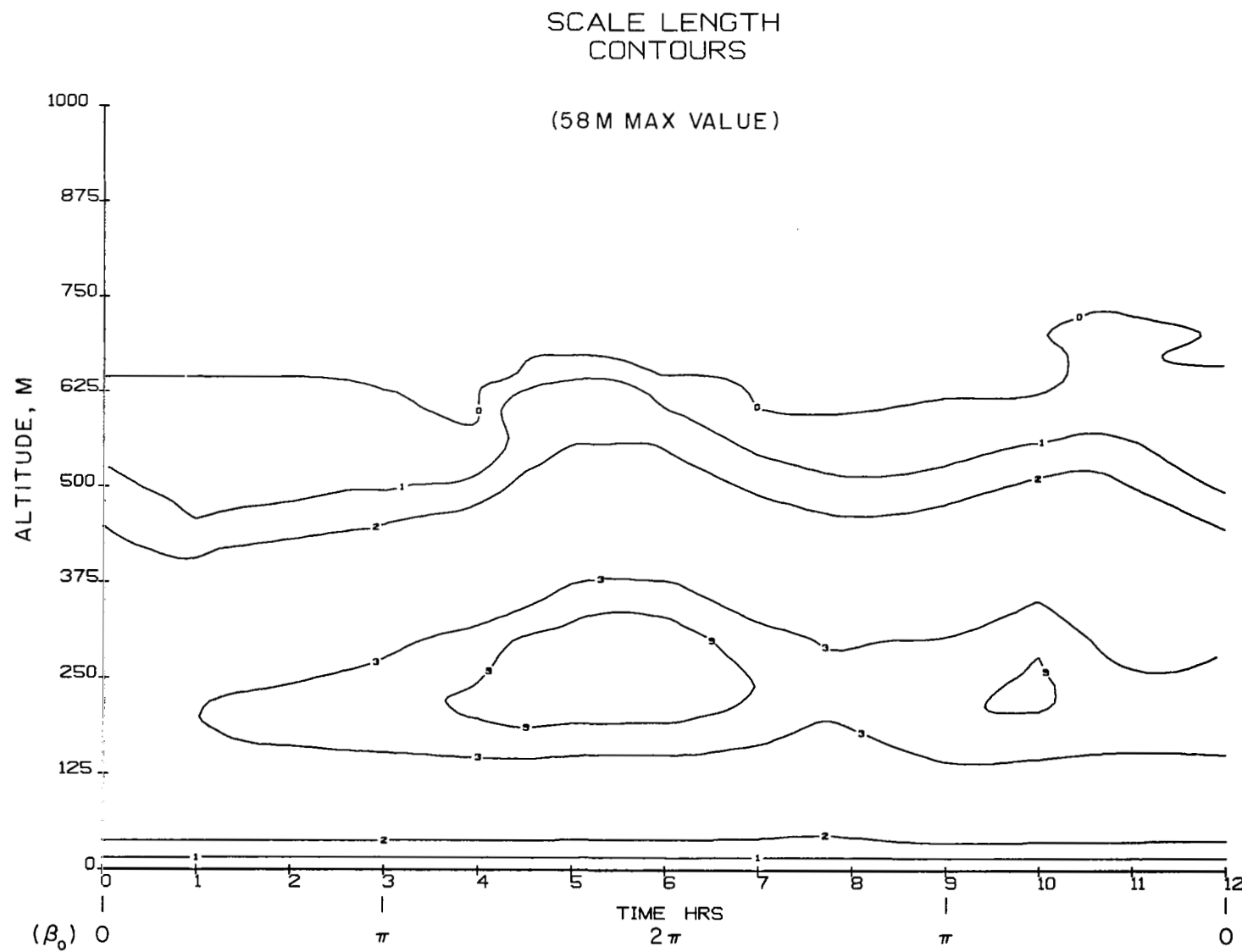


Figure 28. Isolines of turbulence macroscale Λ for the conditions of figure 25.

If, instead of increasing the stability, the magnitude of the driving thermal wind is increased an order of magnitude corresponding to 3°C in 10 km ($M = 10$) but other conditions remain the same as in figures 21 through 24, the maximum velocity in the U direction is increased to 25.4 m/sec and that in the transverse direction to 24.6 m/sec while the turbulence q^2 increases to 12.5 (m/sec) 2 . The maximum wind shear for this case is increased to 0.33 sec^{-1} . The maximum velocities associated with this case are close to the maximum gust velocities typically associated with the passage of thunderstorms. It might be anticipated that the maximum velocities and also the wind shear could be further increased by applying stable, vertical temperature gradients to this case. However, the large levels of turbulence associated with this case tend to rapidly mix any vertical temperature gradients before they significantly damp the turbulence. Thus, only quite modest further increases in maximum velocities and maximum wind shear are achieved by imposing any reasonable vertical thermal boundary conditions on this problem of very large M .

The influence of temperature advection is closely associated with the stabilizing effect of the vertical thermal boundary layer conditions. The computer run associated with figures 25 through 28 was rerun with temperature advection added. No other changes were made in the input conditions. The major difference in the computed results is that the advection destroys the periodicity of the output. Due to the nonlinearity in the source term, eq. (22), there is a net energy sink. So there is continued cooling in the mixed layer between the surface and the inversion layer. Figures 29a and 29b show the difference in the wind and temperature mean profiles two complete periods after the run is started with the same initial conditions. 12 hours later, run 16 would again predict the same profiles, but run 17 would have a further decreased mixed layer temperature and an even stronger shear layer in the neighborhood of 300 m altitude.

The results of our runs show that the influence of baroclinicity is strongly affected by the time history of its development on the time scale over which it is likely to occur in nature. Thus, in any attempt to simulate conditions in the baroclinic atmospheric boundary layer at a given time and place, it is necessary to trace the development of the boundary layer for some time preceding the desired time. In the case of our attempt (ref. 9) to simulate the conditions at JFK airport at the time of the Eastern Airlines crash in June 1975, we started the simulation 16 hours in advance of the desired time. The detailed distribution predicted and presented in reference 9 will not be repeated here. The general conclusion was that a wind shift of the order of 15 m/sec within a 100 m altitude change was consistent with the meteorological conditions leading up to and at the time of the crash. Shear of this same order of magnitude is given in several figures of this report, but the wind shift over any 100 m altitude change is less.

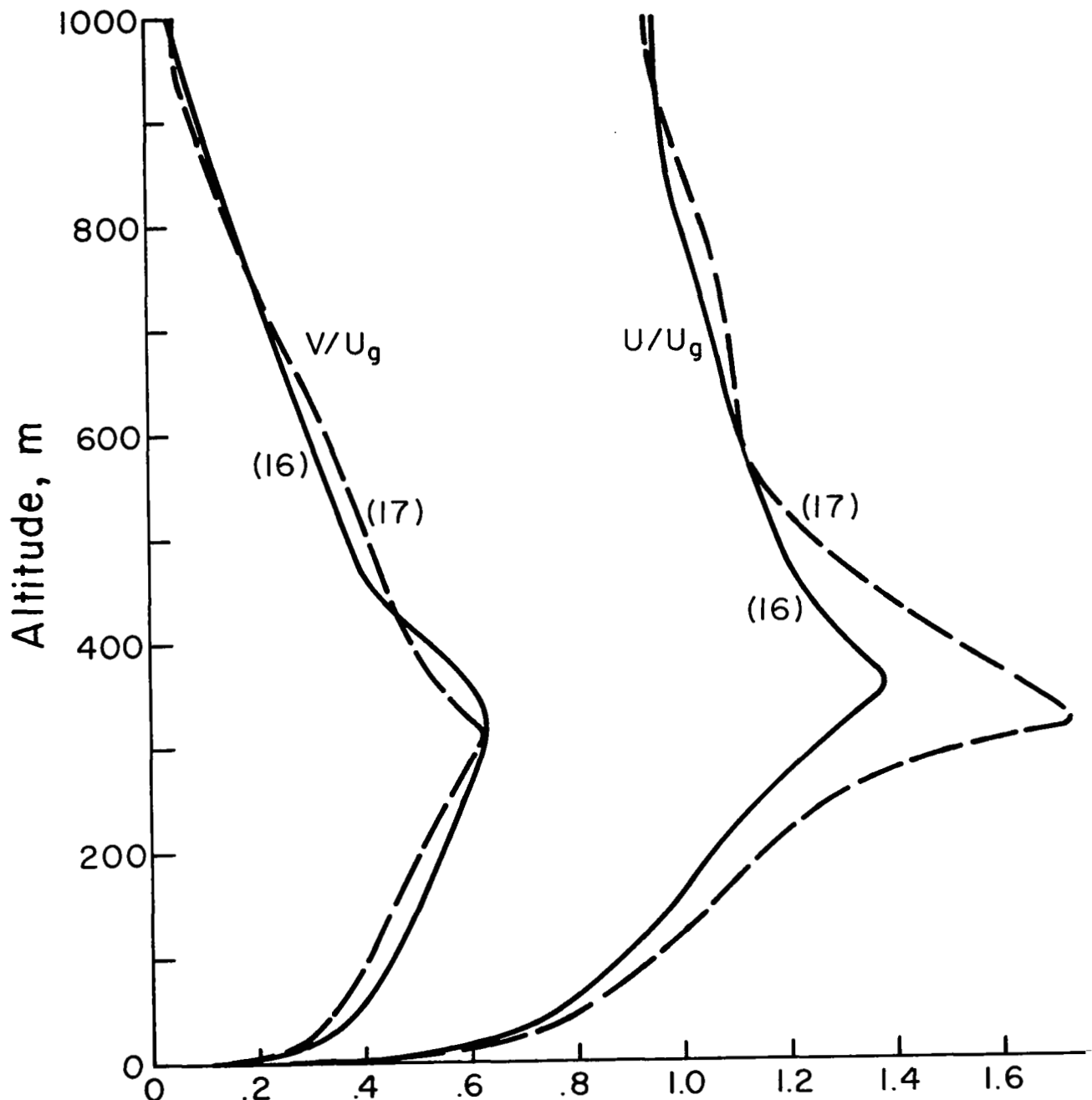


Figure 29a. Influence of temperature advection on the profiles of figures 25 and 26 at a set time, 24 hours, after initialization of the run (Run 16 without advection and Run 17 with advection):
(a) mean wind components.

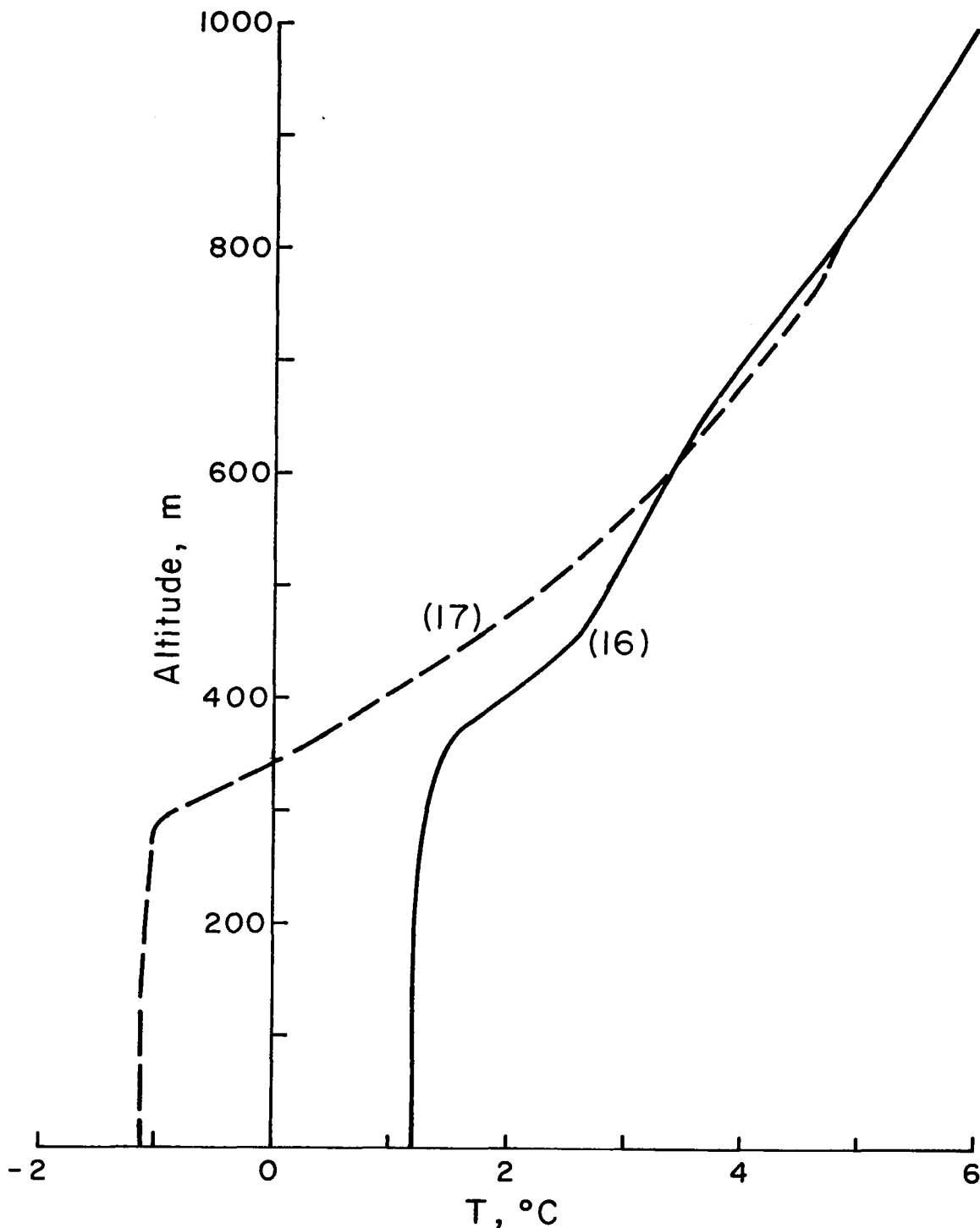


Figure 29b. Influence of temperature advection on the profiles of figures 25 and 26 at a set time, 24 hours, after initialization of the run (Run 16 without advection and Run 17 with advection); (b) potential temperature distribution.

Radiation Flux Divergence

The distributions of wind and turbulence may be strongly affected by the direct energy source or sink within the boundary layer by thermal radiation flux divergence. This has already been indirectly demonstrated by the influence of the upper-level temperature gradient on some of the previous solutions, since radiation is important in maintaining this stable upper-level temperature gradient. Here we would like to carry this a step further in demonstrating that under some conditions radiation flux divergence can govern the diurnal cycle.

In places where the earth's surface has a very high heat capacity, the surface temperature may be taken as essentially constant over time periods of the order of a day. This is the case for the ocean. Under the conditions of a constant surface temperature, any thermal diurnal variations will be driven by the direct energy absorption or emission from the gas in the boundary layer. Figures 30 through 33 simulate such a possible diurnal variation. For this case, the geostrophic wind was maintained constant at a typical value of 10 m/sec. The upper-level potential temperature gradient was maintained at $3^{\circ}\text{C}/\text{km}$, the aerodynamic surface roughness was set at 0.10 m, and the surface temperature held fixed. A radiation source term of the form

$$\dot{Q}_r = .000556 \sin\left(\frac{2\pi t}{24}\right) \cos\left(\frac{\pi z}{4000}\right) \left(e^{-z/500}\right)^2 (\text{°C/sec}) \quad (23)$$

was assumed. This is the type of radiation flux divergence which might be expected in a boundary layer with a relatively strong decrease in water vapor with altitude. The periodic variation with time was again chosen to eliminate initial condition dependency.

The resulting gravitational instability in the vicinity of the top of the heated layer forces this boundary layer to be relatively thick (approx. 1.8 km). We have only shown the lowest 1 km in figures 30 through 33. The turbulence intensity plot (fig. 32) is quite similar to that for the typical midwestern summer day (fig. 15). Although the stability in the surface layer is 12 hours out of phase with respect to the earlier run (i.e., the night time surface layer is unstable while the day time surface layer is stable), the maximum turbulence intensity is dominated more by the stability in the upper regions of the boundary layer which follows the same time dependence as that for figure 15. This upper region stability also dominates the turbulent scale variation in figure 33.

The maximum U wind component occurs in the afternoon, while the maximum V component occurs in the late morning. The maximum wind shear above 10 m altitude is 0.12 sec^{-1} , occurring at approximately 15 hours.

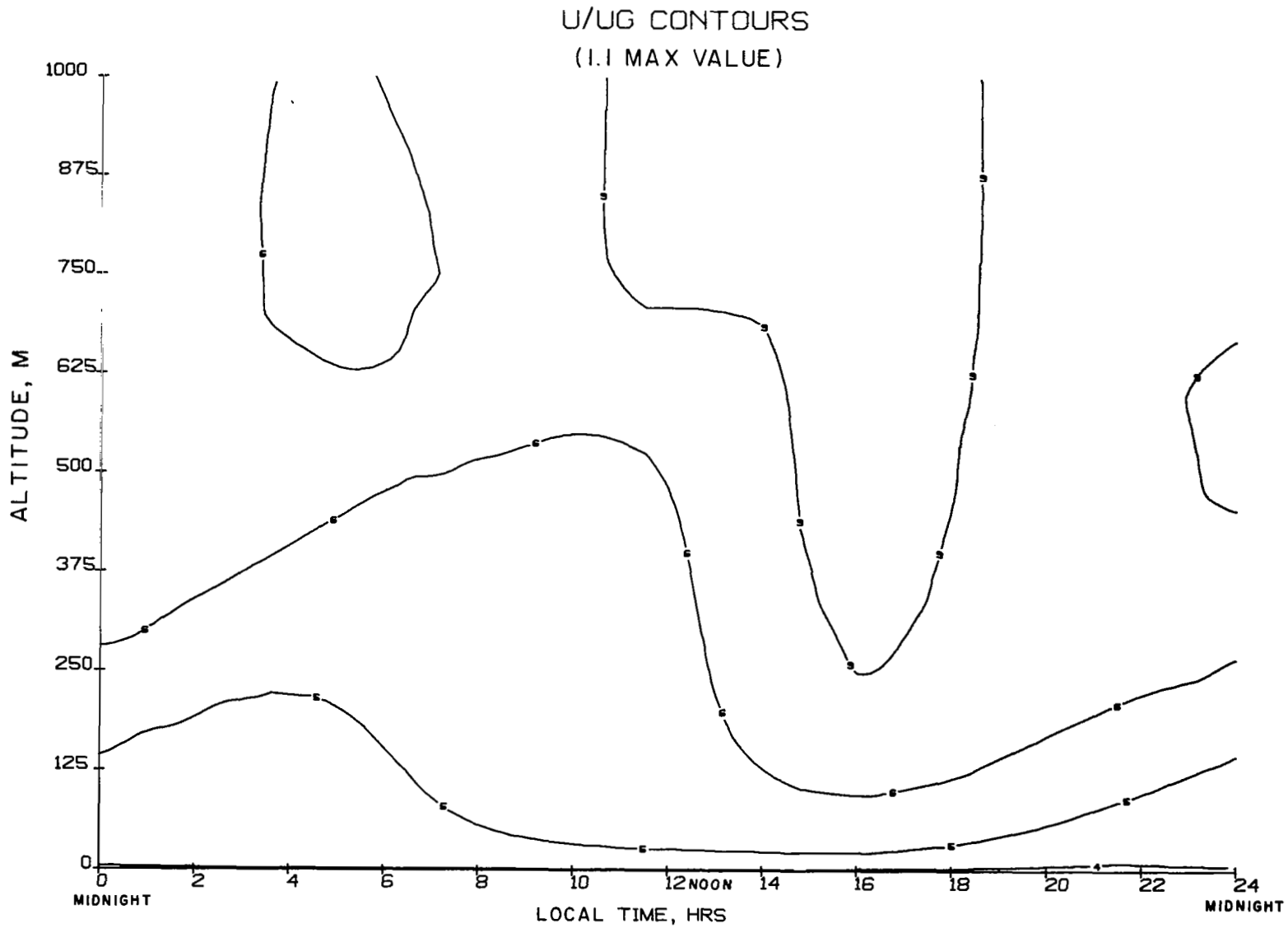


Figure 30. Isolines of u for a simulated day with the radiation flux divergence of Eq. (23) over a constant temperature surface ($R_0 = 10^6$, $\partial\theta/\partial z = 3^\circ\text{C}/\text{km}$, $M = 0$).

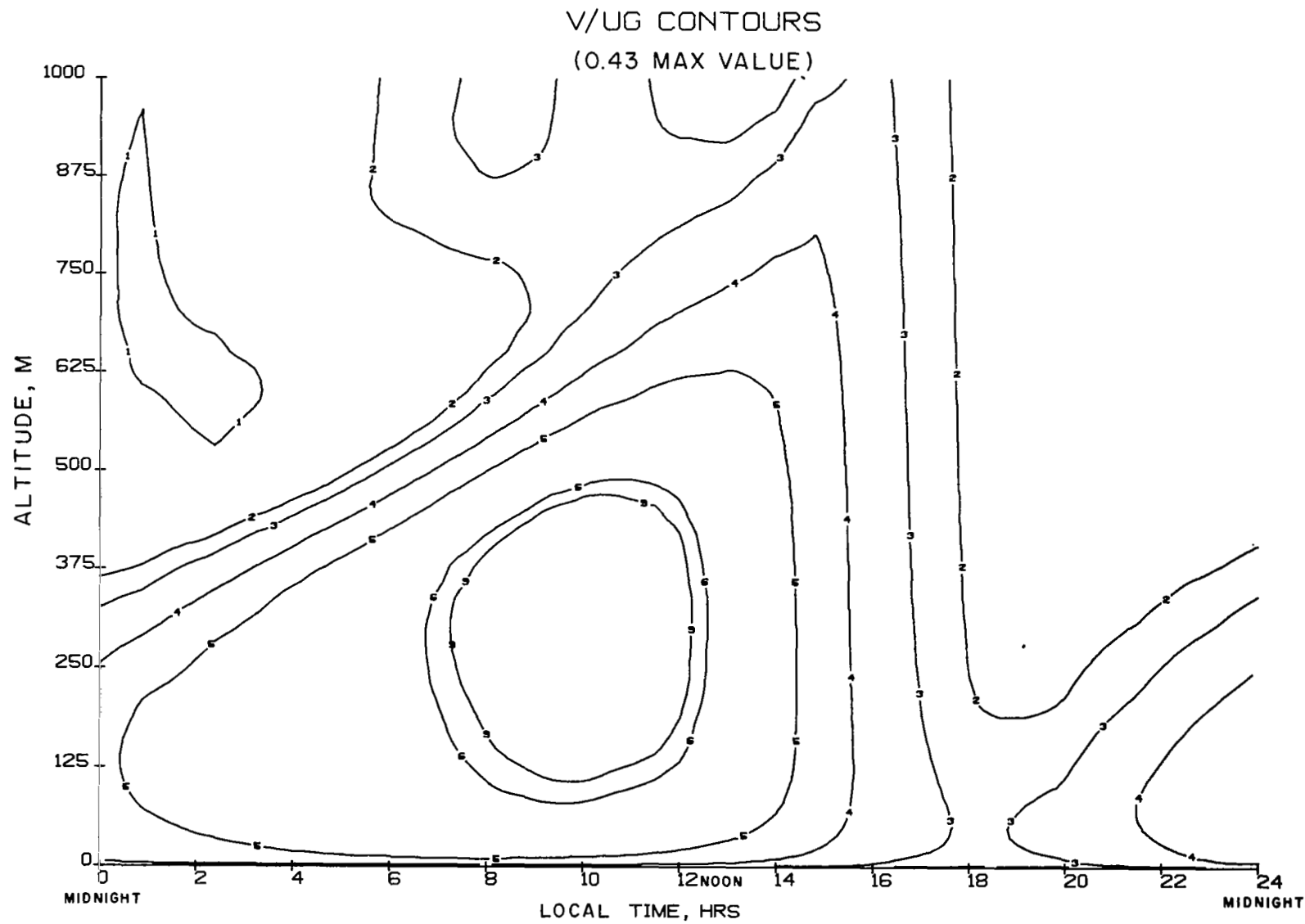


Figure 31. Isolines of v for the conditions of figure 30.

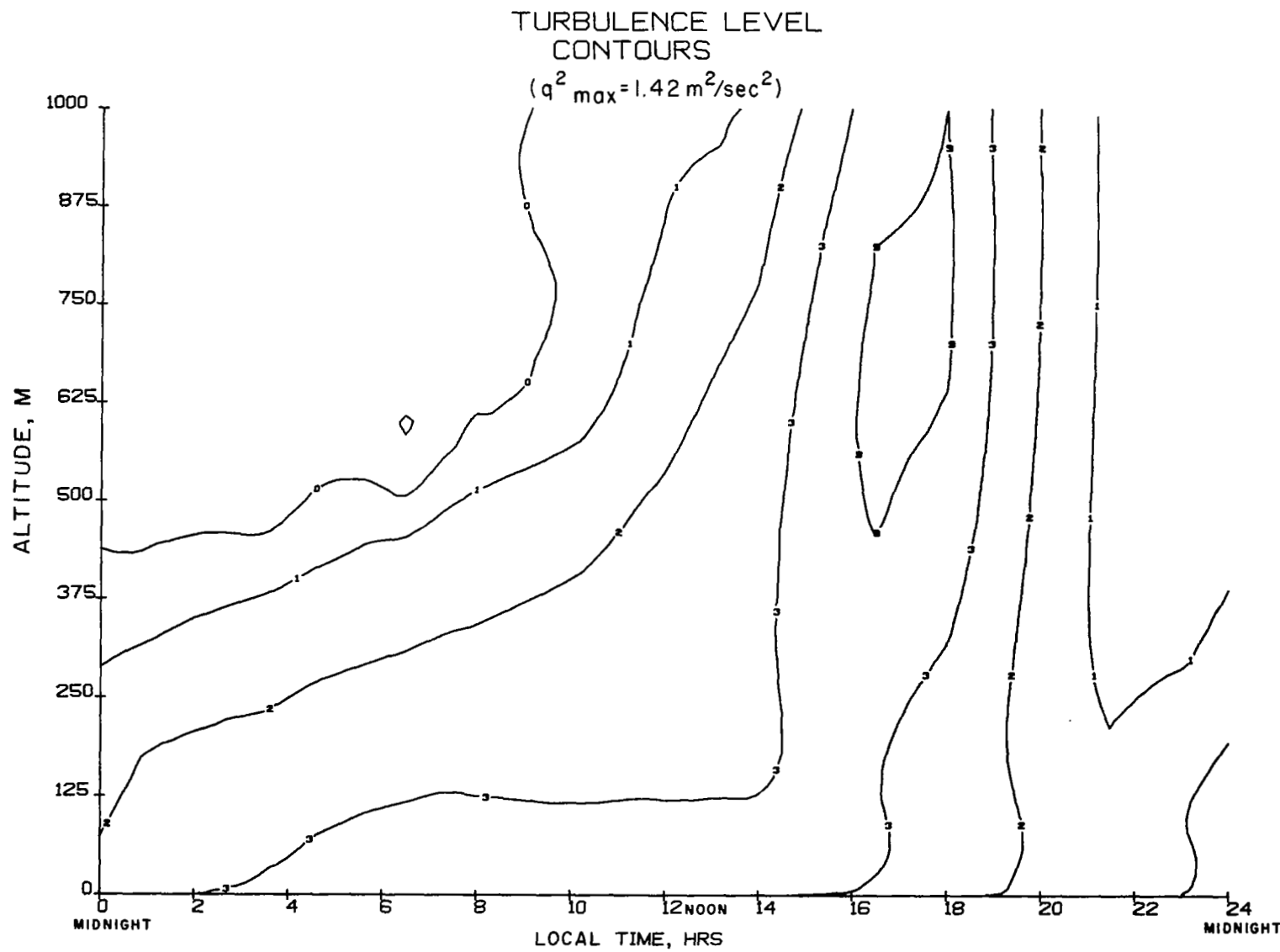


Figure 32. Isolines of turbulence intensity q^2 for the conditions of figure 30.

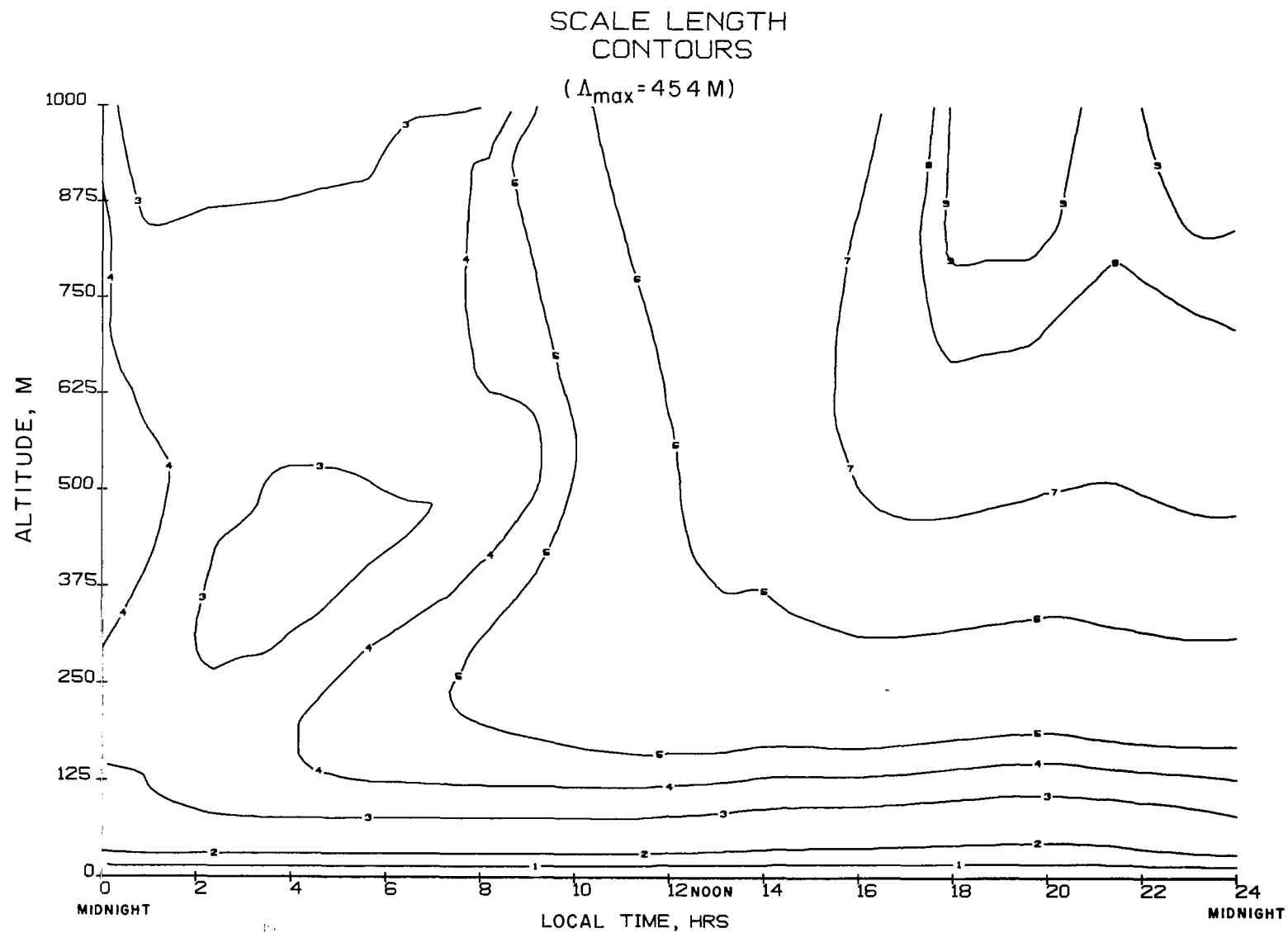


Figure 33. Isolines of turbulence macroscale Λ for the conditions of figure 30.

CONCLUDING REMARKS

We have not attempted to predict results for all possible combinations of the governing parameters. In fact, we have shown that even if this were done it would not exhaust the possibilities for wind and turbulence profiles which might exist, due to the importance of the time history of the governing parameters. Even within the limitations of our one-dimensional approximation, there is indeed a rich assortment of possible wind and turbulence profiles. What we have shown here is a sampling of the possibilities with some indication of the influence of the governing parameters.

A partial summary of the turbulence intensity for different conditions is shown in figure 34. Refer to Table III for the key to the different conditions. The turbulence is normalized by the maximum wind velocity between the ground and 1 km and plotted as a function of stability. As indicated in the previous section, it is not possible to reduce the detailed influences of stability to a single parameter. But for purposes of indicating only the rough dependence of stability, we have chosen a single parameter which does partially combine the influence of the surface heat flux which controls stability in the surface layer and the influence of the upper-level potential temperature gradient which influences the elevation of the inversion layer which caps the boundary layer. This parameter is a bulk Richardson number based on the velocity and potential temperature differences between the surface and 1 km. The hysteresis loops presented for the different periodic cycles considered indicate the type of scatter to be expected in attempting to predict the fluctuations in this manner. As the bulk Richardson number approaches $-\infty$, the conditions for free convection, the normalized q will approach ∞ . On the stable side, increasing $Ri(1000)$ tends to decrease the normalized q whether the increase in stability is caused by increased surface cooling or a decrease in the upper-level inversion height.

A similar rough summary of the maximum wind shear occurring at or above 10 m altitude in the boundary layer is given in figure 35. There is a fairly consistent trend of increasing shear with increasing stability, although there is a relatively strong influence of thermal wind which tends to mask this trend to some extent. The normalization of q by the maximum velocity within the layer tends to roughly compensate for the thermal wind influence in figure 34. Of course, the wind shear in a profile at a given time cannot be characterized by a single number. The actual changes in airspeed which an aircraft will encounter will also depend on the vertical depth over which this large shear exists. This must be determined by looking at the detailed profiles. Figure 35 does indicate the rough rule of thumb that as either horizontal temperature gradients increase or vertical stable temperature gradients increase, problems with wind shear may be expected to increase.

MAX TURB VS. RI

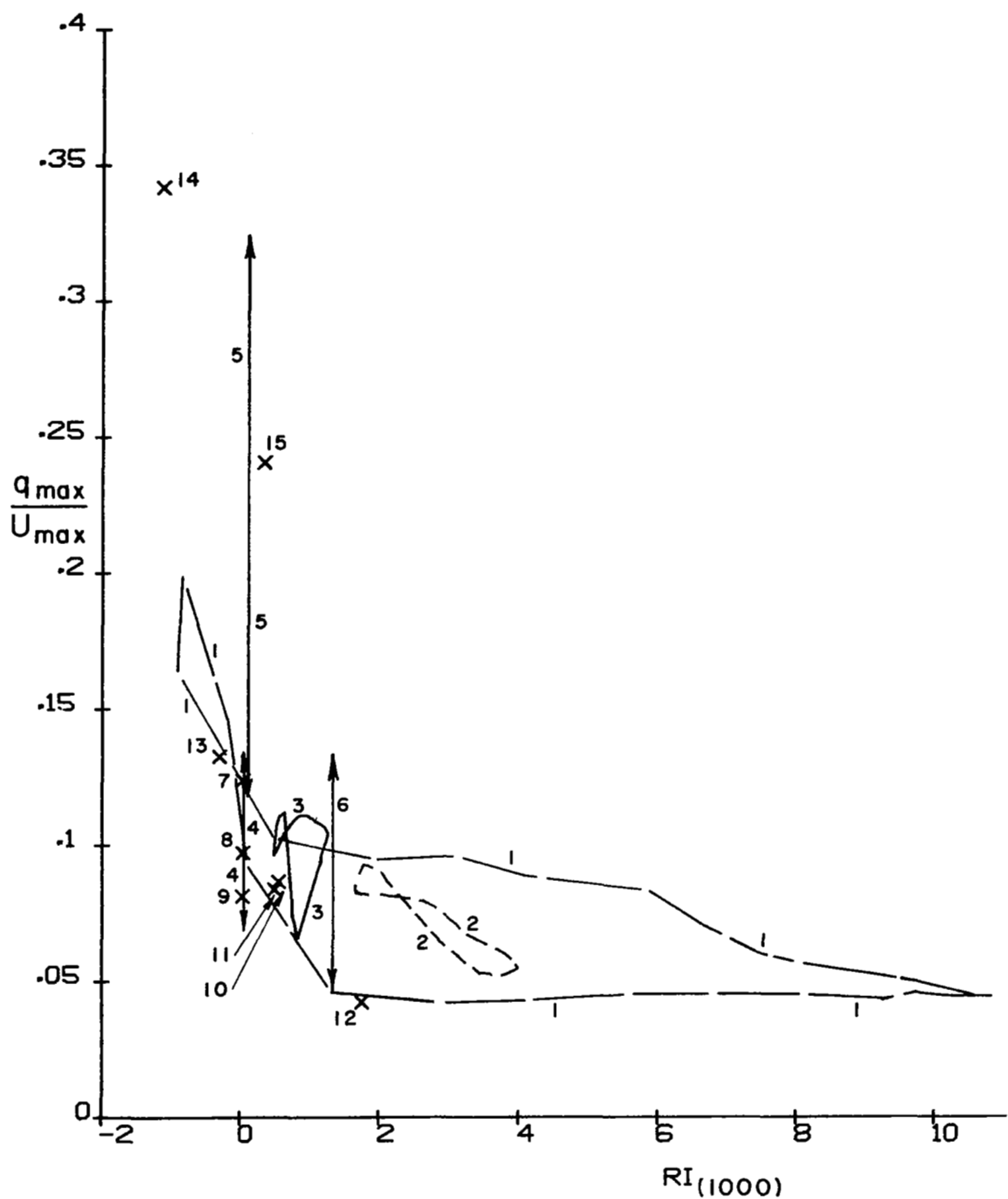


Figure 34. Summary plot of normalized total velocity fluctuation as a function of the bulk Richardson number between the surface and 1 km altitude.

MAX SHEAR VS. RI

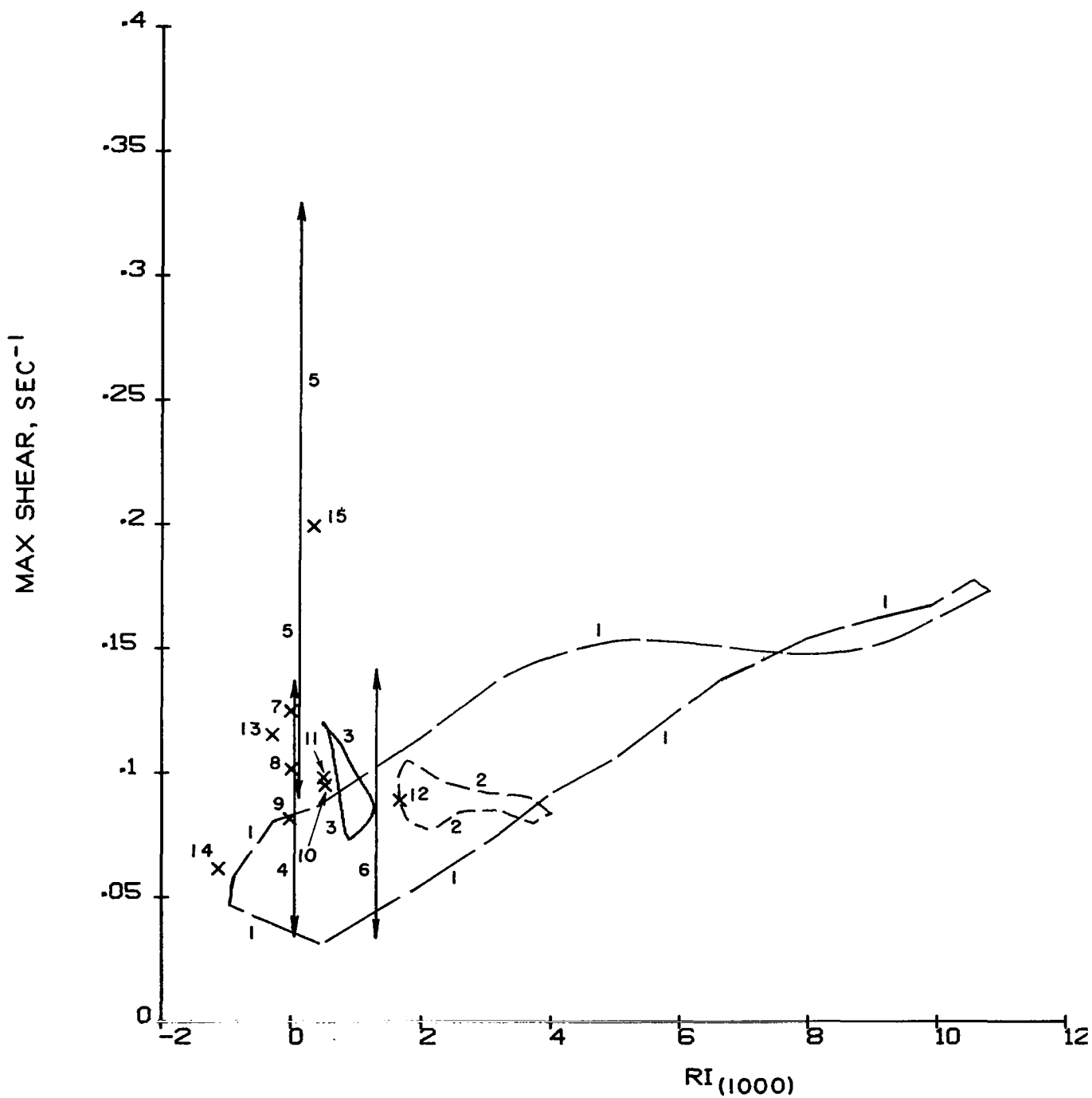


Figure 35. Summary plot of maximum wind shear at or above 10 m altitude as a function of the bulk Richardson number between the surface and 1 km altitude.

In general, the wind shear decreases with altitude in the lower portion of the boundary layer. This is shown in figure 36 to supplement the summary information in figure 35. The solid curve shows the distribution of wind shear with altitude for the neutral, barotropic distribution of figure 1. The bars represent the change in wind shear caused by two orders of magnitude change in Ro . The dashed curves represent the bounds in the variation of wind shear caused by expected values of Ri . In general, increasing Ri will tend to increase wind shear, as seen in the previous figure, but the minimum wind shear need not coincide with the minimum Ri due to hysteresis effects. Baroclinicity also will, in general, increase wind shear. It is not possible to correlate the variations indicated in figure 36 with time of day. Nocturnal hours do tend to be more stable ($Ri > 0$) and afternoon hours more unstable ($Ri < 0$), but the baroclinicity is associated with changing weather and does not correlate with time of day. A companion curve like figure 36 for the turbulence intensity as a function of altitude would be too misleading, since there is no consistent trend of turbulence intensity with altitude over parameter space. Under stable conditions, the turbulence will decrease, as seen in the early morning hours of figure 15, with altitude, but for unstable conditions at low levels, it will increase strongly with altitude, as seen in the afternoon hours of the same figure.

Many cases in nature where wind shear and turbulence are a problem to aviation are further complicated by the added dimensionality of the phenomena. For example, a strong downdraft may be associated with flow from a thunderstorm. To include the effect of such vertical velocities, it is necessary to at least extend our problem to a two-dimensional, unsteady program. This has been done during the time period of this contract under separate EPA and Navy contracts. This opens up the possibility of predicting the wind shear associated with strong local cold fronts, but this is beyond the scope of the present investigation.

We believe there are two tasks remaining to be accomplished in our effort to determine the feasibility of predicting the general meteorological conditions which lead to wind shear and turbulence conditions most hazardous for aircraft takeoffs and landings. One is a detailed investigation of the ensemble of aircraft accidents identified in Part 2 of this report and, second, a detailed program of comparison with turbulence and wind profiles recorded by airport instrumentation for the purpose of determining the accuracy of our model predictions. This combination of looking at cases which have proven to be a problem in the past, together with a careful delineation of the error involved in our predictions by additional comparisons with field observations, will allow us to determine the feasibility of predicting dangerous situations in advance. We believe that an interaction between our modeling efforts and the

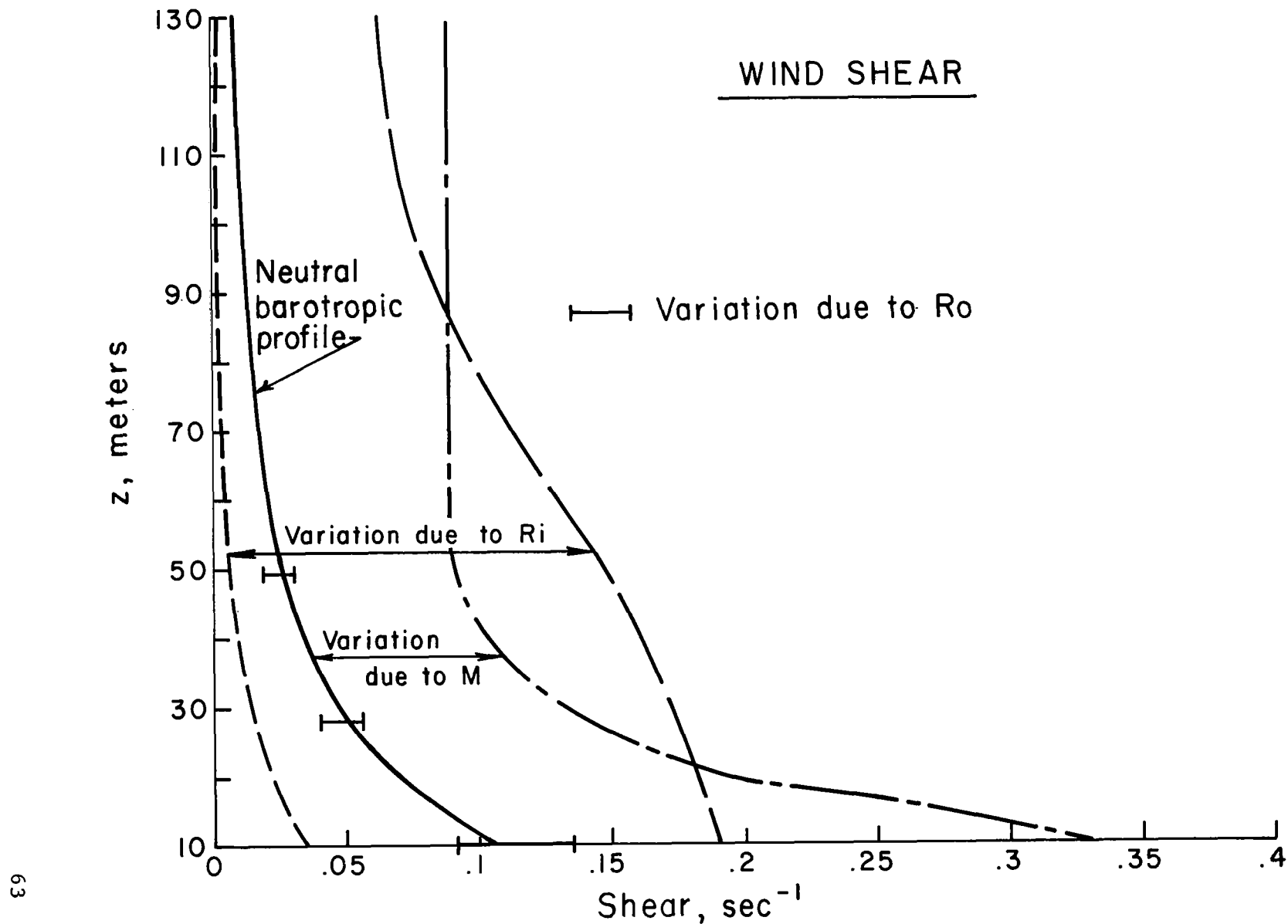


Figure 36. Summary plot of wind shear as a function of altitude showing the influence of the expected range of variations in R_o , R_i and M .

measurements program also would be of benefit to the measurements program by indicating possible modes for organizing the data.

TABLE II
 NOTATION FOR ISOLINE PLOTS
 (For Figs. 8-9, 13-28, and 30-33)

Contour #	represents	U/U_g	V/V_g	$q^2 (m^2/sec^2)$	$\Lambda(m)$
0		-0.9	-0.2	0	1.0
1		-0.6	-0.1	0.1	10.0
2		-0.3	0.05	1.0	20.0
3		+0.1	0.1	1.5	50.0
4		0.3	0.2	2.0	75.0
5		0.6	0.3	2.5	100.
6		0.9	0.4	3.0	200.
7		1.2	0.6	4.0	300.
8		1.5	0.9		400.
9		\leftarrow 95% of maximum value \rightarrow			

TABLE III
KEY FOR SUMMARY PLOTS (FIGS. 34 AND 35)

- 1 For the conditions corresponding to figures 13 - 16
- 2 For the conditions corresponding to figures 17 - 20
- 3 For the conditions corresponding to figures 30 - 33
- 4 For the conditions corresponding to figures 21 - 24
- 5 For the conditions corresponding to figures 21 - 24 but M_∞ increased from 1.25 to 10
- 6 For the conditions corresponding to figures 25 - 28
- 7 Neutral steady state ($Ro = 10^5$, $Ri = 0$)
- 8 Neutral steady state ($Ro = 10^6$, $Ri = 0$)
- 9 Neutral steady state ($Ro = 10^7$, $Ri = 0$)
- 10 Stable atmosphere ($Ro = 10^6$, $Ri_{(10)} = 0.014$)
- 11 Stable atmosphere ($Ro = 10^6$, $Ri_{(10)} = 0.0036$)
- 12 Stable atmosphere ($Ro = 10^7$, $Ri_{(10)} = 0.047$)
- 13 Unstable atmosphere ($Ro = 10^6$, $Ri_{(10)} = -0.0128$, $z_i f/\hat{u} = 0.21$)
- 14 Unstable atmosphere ($Ro = 10^7$, $Ri_{(10)} = -0.035$, $z_i f/\hat{u} = 0.16$)
- 15 For conditions simulating JFK weather at the time of EA Flight 66 crash (fig. 15, ref. 9)

WIND SHEAR AND TURBULENCE AROUND AIRPORTS

PART 2. SELECTION OF AN ENSEMBLE OF AIRCRAFT ACCIDENTS FOR WHICH WIND SHEAR OR TURBULENCE APPEARED TO BE A CONTRIBUTING FACTOR

W. S. Lewellen and Guy G. Williamson

INTRODUCTION

This part of the study is an investigation of a set of accidents where wind shear and/or turbulence were significant factors. The study was conducted in order to select cases which can be used to evaluate the feasibility of predicting when these weather conditions will be hazardous to aircraft operation.

It is well known that wind shear and gusts increase the difficulty of aircraft operation, particularly during landing and takeoff (ref. 20). Gusts or rapid changes in the wind vector as a function of time produce undesirable aircraft accelerations which must be compensated for by control inputs, thus increasing the pilot's workload. Wind shear or changes in the wind vector as a function of spatial location produce similar results. If the change in wind vector is small or occurs slowly, it does not significantly affect aircraft operation. However, rapid large changes can cause crashes, regardless of what the pilot and/or automatic controls do. It is therefore desirable to know

- a) what magnitude of wind shear and turbulence pose threats to aircraft safety, and
- b) when and where such threats exist.

Answers to the first part of the question have been based on past operating records and simulator studies. The solution to the second part requires direct measurement of these variables or reliable predictions of their likely existence.

Measurement of these variables throughout the landing and takeoff space requires elaborate, expensive equipment and it is not considered feasible for many airports at the present time. On the other hand, the reliability of predicting these conditions must still be shown.

One step in evaluating a predictive technique is to compare its results with known weather conditions which probably caused a real aircraft accident. If the technique can predict weather

conditions similar to those at the time of the accident, then it can conceivably be used to warn aircraft operations personnel of impending unsafe flight conditions. In order to perform this evaluation, it is necessary to select a number of real accident cases for use in the comparison.

Turbulence and/or wind shear are associated with several different weather conditions. An obvious hazardous weather condition is in the vicinity of thunderstorms. Here one expects strong turbulence, horizontal wind shear, and downdrafts. A not so obvious condition is when very stable temperature gradients prevail and high shears and low turbulence are possible. This type of condition can also have fog associated with it. The combination of low visibility due to fog and unexpected wind shear can give rise to aircraft accidents in which the wind shear factor goes unnoticed. These stable conditions can also occur during the passage of a cold front with the cold air slipping under the existing warm air mass. A third condition of interest occurs when a strong wind condition is combined with a sizable change in surface roughness. This combination, as exemplified by a sea breeze passing over a hilly island, can produce hazardous gusty conditions.

The selection of accidents for future study has been conducted with an eye towards obtaining cases representative of a number of different conditions. Such a study would permit a catalogue of hazardous weather conditions to be constructed with the complete model description of the detailed profiles of wind magnitude and direction and ensemble-averaged, turbulent fluctuations for each case. The selection process is further described and the resulting cases listed in the following section.

SELECTING ACCIDENT CASES

The starting point for the selection of accident cases was the National Transportation Safety Board (NTSB) aircraft accident data stored on magnetic tape. A description of each accident is generated and stored in coded form as specified in reference 21. The important characteristics of the accidents for this study are

1. Operational phase of flight
(landing, takeoff, climbout, etc.)
2. Type of accident
(stall, spin, hard landing, collision, etc.)
3. Probable causes of accident
(weather, pilot, terrain, etc.)

Since the study is concerned with low altitude wind shear and turbulence, the operational phases were limited to takeoff, landing, and missed approach. Similarly, the types of accidents which are likely to be caused by these weather conditions are hard landing, collision with ground obstacles, overshoot, undershoot, and stall. Finally, the probable causes or factors involved in the accidents are particular weather conditions and pilot error. Accidents due to certain pilot errors have been included because (a) pilot errors themselves could be induced by wind shear and turbulence, or (b) the effects of wind shear could be mistaken for pilot error. The above-mentioned accident characteristics are summarized in Table IV. Note that "wind shear" is not a codeable cause/factor, so other possibly related cause factors must be used.

The NTSB aircraft accident data bank was queried for the time period 1970-1974. The search was done in several parts with some accidents appearing in more than one part. Adjusting to approximately remove the redundancy from the accident count results in 1160 accidents in which wind shear or turbulence may be involved. Obviously, this large number of accidents should be further screened in order to obtain a more select set for further study. The next cut was based on the following observations:

1. The stronger the wind shear or turbulence, the greater the aircraft upset and, therefore, seriousness of the accident.
2. The accident data files for commercial accidents are more comprehensive than those for noncommercial ones.

Therefore, noncommercial accidents listed as less than serious were, with a few exceptions, deleted from the candidate list. The exceptions are cases where either the terrain or weather conditions made them particularly interesting. This left 47 takeoffs and 85 landings, a total of 132 candidate accidents.

TABLE IV.

Cause/Factors, Type of Accident, and Operational Phases
where Wind Shear and/or Turbulence Could Have Contributed
to the Aircraft Accident

Cause/Factors

Sudden wind shifts
Unfavorable wind conditions
Downdrafts, updrafts
Improper compensation for wind conditions
Fog
Thunderstorm activity
Clear air turbulence
Failed to maintain flying speed
Misjudged distance, speed, altitude
Delayed initiating go-around
Failed to initiate go-around
Continued flight into known area of severe turbulence
Lost/disoriented
Misused flaps
Spontaneous improper action
Failed to maintain directional control
Vortex turbulence

Type of Accident

Hard landing
Collision with ground - controlled
Collision with ground -
uncontrolled
Collision with obstructions
Overshoot
Undershoot
Stall
Stall - spin
Stall - spiral
Stall - mush
Turbulence
Uncontrolled altitude deviation

Operational Phase

Landing - final VFR
Landing - final IFR
Landing - initial
Landing - level off/touchdown
Landing - go-around
Landing - missed approach
Takeoff - initial climb

The next cut from this list was made on the basis of the complexity of modeling the local weather conditions. In particular, noncommercial accidents occurring in areas where there are gross changes in the features of the terrain or occurring within thunderstorms were excluded due to modeling difficulties. This left 53 accidents to be studied in more detail.

The files for 40 of these accidents were reviewed at the Office of Public Inquiries in Washington, and 18 cases were selected for further study. The others were excluded primarily due to complex terrain and crosswind effects as opposed to wind shear and turbulence. In addition, accidents involving pilots with less than 1000 total hours and less than 100 hours in that type of aircraft were excluded in order to reduce the probability that pilot inexperience was a cause. It is anticipated that a few of the remaining accidents will be eliminated on the basis of further review.

For accidents occurring to scheduled flights, the file can run several hundred pages and usually contains all the data necessary for local weather analysis. However, the vast majority of the accidents occur on nonscheduled flights and the files associated with these are usually just a few pages. For further study of these cases, it will be necessary to obtain the appropriate weather data from the National Weather Service. Terrain data in the vicinity of some of the airports will also be required. The particulars for the final set of accidents selected are given in Table V.

TABLE V. ACCIDENTS FOR FURTHER INVESTIGATION

File No.	Location	Date	A/C No.	Commercial or Noncomm. Flight	Accident Type	Operational Phase	Cause/Factor ^x
A-0004	MA., Boston	12/17/73	EC-CBN	C	Hit obstruction	Landing	S.W.
	NY-JFK	6/24/75	N8845E		Hard landing	Landing	D-U
1-0041	Missouri, St.Louis	7/23/73	N4215	C	Hard landing	Landing	TSTM, U.W.
1-0028	Tennessee, Chatanooga	11/27/63	N3323L	C	Undershoot	Landing	U.W.
1-0047	NY-JFK	12/12/72	N788TW	C	Hit obstruction	Landing	S.W.
3-0001	NY-LaG.	1/4/71	N7	C	Hit obstruction	Landing	U.W.
3-0001	Penna., Johnstown	1/6/74	N125AE	C	Stall	Landing	D-U
3-4528	Puerto Rico, Culebra	12/21/71	N589JA	C	Hit ground	Landing	U-D
3-0617	N.Carolina, Morrisville	4/2/70	N401RA	NC	Hit trees	Landing	S.W.
3-3086	Conn., Madison	8/26/74	N5065B	C	Undershoot	Landing	D-U
3-1898	Washington, Mead	5/19/74	N55	NC	Undershoot	Landing	D-U

^x Standard cause/factor terms: S.W. = sudden wind shift; D-U = downdraft-updraft; U.W. = unfavorable wind; TSTM = thunderstorm

File No.	Location	Date	A/C No.	Commercial or Noncomm. Flight	Accident Type	Operational Phase	Cause/ Factor
3-0780	Georgia, St. Marys	3/26/70	N7332T	C	Stall	Takeoff	U.W.
-----	-----	-----	-----	-----	-----	-----	-----
1-0050	Virgin Is., St. Thomas	12/10/70	N3417	C	Hard landing	Landing	U.W.
1-0012	Calif., Los Angeles	1/16/74	N757TW	C	Hard landing	Landing	Fog
1-0005	Kansas, Wichita	3/3/74	N2307	C	Overshoot	Landing	Rain
1-0041	Alaska, Sitkinak	10/2/70	N9117	C	Stall	Takeoff	U.W.
1-0002	Calif., Ontario	3/31/71	N3166	C	Hit ground	Landing	Fog
1-0008	Alaska, N. Juneau	9/4/71	N2969G	C	Hit ground	Landing	Fog

Note: The files of those accidents listed above the dashed line were reviewed in some detail while those below the dashed line were selected on the basis of the accident brief only.

REFERENCES

1. Donaldson, Coleman duP., "Calculation of Turbulent Shear Flows for Atmospheric and Vortex Motions," AIAA Journal 10, 1, 1972, pp. 4-12. DRYDEN RESEARCH LECTURE
2. Donaldson, Coleman duP., "Construction of a Dynamic Model of the Production of Atmospheric Turbulence and the Dispersal of Atmospheric Pollutants," Workshop on Micrometeorology, American Meteorological Society, Boston, 1973, pp. 313-392.
3. Donaldson, Coleman duP., "Atmospheric Turbulence and the Dispersal of Atmospheric Pollutants," Environmental Protection Agency Report EPA-R4-73-016a, 1973.
4. Lewellen, W.S., M.E. Teske, Ross M. Contiliano, Glenn R. Hilst, and Coleman duP. Donaldson, "Invariant Modeling of Turbulent Diffusion in the Planetary Boundary Layer," Environmental Protection Agency Report EPA-650/4-74-035, 1974.
5. Lewellen, W.S. and M.E. Teske, "Turbulence Modeling and Its Application to Atmospheric Diffusion," Environmental Protection Agency Report EPA-600/4-75-016, 1975.
6. Lewellen, W.S., M.E. Teske, and Coleman duP. Donaldson, "Turbulence Model of Diurnal Variations in the Planetary Boundary Layer," Proc. 1974 Heat Transfer and Fluid Mechanics Institute (L.R.Davis and R.E.Wilson, eds.), Stanford University Press, 1974, pp. 301-319.
7. Lewellen, W.S. and M.E. Teske, "Prediction of the Monin-Obukhov Similarity Functions from an Invariant Model of Turbulence," J. Atmos. Sciences 30, 7, 1973, pp. 1340-1345.
8. Lewellen, W.S., M.E. Teske, and Coleman duP. Donaldson, "Examples of Variable Density Flows Computed by a Second-Order Closure Description of Turbulence," AIAA Paper No. 75-871, 1975.
9. Lewellen, W.S., Guy G. Williamson, and M.E. Teske, "Estimates of the Low-Level Wind Shear and Turbulence in the Vicinity of JFK on the Afternoon of 24 June 1975," Aeronautical Research Associates of Princeton, Inc., Report No. 261, 1975.
10. Estogue, M.A., "Numerical Modeling of the Planetary Boundary Layer," Workshop on Micrometeorology, American Meteorological Society, Boston, 1973.
11. Wyngaard, J.C. and O. R.Coté, "The Evolution of a Convective Planetary Boundary Layer: A High-Order-Closure Model Study," Boundary Layer Meteorology 7, 1974, pp. 289-308.
12. Wyngaard, J.C., O.R. Coté, and K. S. Rao, "Modeling the Atmospheric Boundary Layer," Advances in Geophysics 18A, Academic Press, New York, 1974.

13. Rao, K.S., J.C. Wyngaard, and O.R. Coté, "The Structure of Two-Dimensional Internal Boundary Layer Over a Sudden Change of Surface Roughness," *J. Atmos. Sciences* 31, 1974, pp. 738-746.
14. Mellor, G.L. and T. Yamada, "A Hierarchy of Turbulence Closure Models for Planetary Boundary Layers," *J. Atmos. Sciences* 31, 1974, pp. 1791-1806.
15. Yamada, T. and G. L. Mellor, "A Simulation of the Wangara Atmospheric Boundary Layer Data," *J. Atmos. Sciences* 32, 1975, pp. 2309-2329.
16. Shir, C.C., "A Preliminary Numerical Study of Atmospheric Turbulent Flows in the Idealized Planetary Boundary Layer," *J. Atmos. Sciences* 30, 1973, pp. 1327-1339.
17. Zilitinkevich, S.S., "Resistance Laws and Prediction Equations for the Depth of the Planetary Boundary Layer," *J. Atmos. Sciences* 32, 1975, pp. 741-752.
18. Arya, S.P.S. and J.C. Wyngaard, "Effect of Baroclinicity on Wind Profiles and the Geostrophic Drag Law for the Convective Planetary Boundary Layer," *J. Atmos. Sciences* 32, 1975, pp. 767-778.
19. Wyngaard, J.C., "Notes on Surface Layer Turbulence," Work-Shop on Micrometeorology, American Meteorological Society Boston, 1973.
20. Luers, J.K. and J.B. Reeves, "Effect of Shear on Aircraft Landing," NASA CR-2287, July 1973.
21. "Manual of Code Classifications: Aircraft Accidents and Incidents," National Transportation Safety Board, Department of Transportation, 1972.